Time-Reversal of Seismic Waves in SeisSol

Philipp Wendland

Master's Thesis in Robotics, Cognition, Intelligence

Department of Informatics
Technical University of Munich

Department of Informatics
Technical University of Munich

Master's Thesis in Robotics, Cognition, Intelligence

Time-Reversal of Seismic Waves in SeisSol

Zeitumkehrung von seismischen Wellen mit SeisSol

Supervisor Prof. Dr. Michael Bader

Advisor Sebastian Wolf, M.Sc.

Author Philipp Wendland

Date May 15, 2021 in Garching

Disclaimer

I confirm that this Master's Thesis is my own work and I have documented all sources and material used.

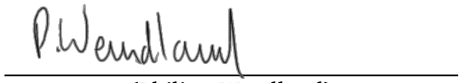

Garching, May 15, 2021 (Philipp Wendland)

Acknowledgements

I would like to thank Prof. Dr. Michael Bader for giving me the opportunity to write my master's thesis at the Chair for Scientifc Computing in Computer Science (SCCS). I am grateful for my advisor, Sebastian Wolf, who proposed the topic and helped refine it. He supported me throughout the making of this thesis and guided me in the research.

Finally, I want to thank my friends and family for their constant support during my studies and their eagerness to help wherever they could.

Abstract

The numerical simulation of 3D earthquake phenomena is increasingly important in modern-day seismology. In this work, a time-reversal method, based on the theory of the Time-Reversal Cavity, was implemented in the simulation software SeisSol. This approach yields a novel method to determine the epicenter of an earthquake. During the simulation, the waves in the forward direction were recorded by a set of receivers located at the surfaces of the examined volume, a $(10 \times 10 \times 10)$ m cube. The recorded time evolution of points inside the volume from both the forward and the time-reversed simulation were then compared using time-frequency misfit analyses. During these analyses, an improved criterion for the spacing of receivers on a grid was found that yields consistently small errors, namely, when receivers are spaced $\psi_P/8$ apart, where ψ_P is the wavelength of the P-wave. In both homogeneous and inhomogeneous media, an accurate time-reversal was achieved. In addition to the quantitative analyses, a qualitative analysis was performed in order to determine the minimum number of receivers required for the accurate observation of a converging wave. With knowledge of the moment tensor of the source, one receiver on each face of the cube provided enough information to determine the origin of the source. Finally, the time-reversal method was successfully applied to the benchmark test WP2_LOH1, visually confirming that a time-reversal can be achieved in realistic media beyond the $(10 \times 10 \times 10)$ m test volume.

Zusammenfassung

Numerische Simulationen von Erdbeben in einem drei-dimensionalem Raum sind von zunehmender Wichtigkeit in moderner Seismologie. Basierend auf der Theorie der *Time Reversal Cavity* wurde in dieser Arbeit eine Methode zur Zeitumkehrung von seismischen Wellen in der Simulationssoftware SeisSol implementiert. Dieser Ansatz bietet eine neue Art und Weise, das Epizentrum von Erdbeben bestimmen zu können. Während einer Simulation werden die Wellen der Vorwärts- und der zeitumgekehrten Richtung von Empfängern auf der Oberfläche des $(10 \times 10 \times 10)$ m Testvolumens aufgenommen. Die aufgenommene Zeitentwicklung von sowohl der vorwärtslaufenden Welle als auch der Welle aus der Zeitumkehrung wurden dann mit Hilfe der Zeit-Frequenz Fehleranalyse begutachtet. Durch die Analyse wurde ein Kriteritum für den Abstand zwischen zwei Empfängern gefunden. Sind Empfänger weniger als $\psi_p/8$ voneinander entfernt, wobei ψ_p die Wellenlänge der P-Welle ist, ist der Fehler zwischen der Vorwärts- und der zeitumgekehrten Richtung sehr klein. Sowohl in homogenen als auch in inhomogenen Medien wurden so erfolgreiche Zeitumkehrungen durchgeführt. Über die quantitativen Analysen hinaus, wurde eine qualitative Analyse zur Bestimmung des maximalen Abstands zweier Empfänger durchgeführt, sodass eine konvergente Welle immer noch sichtbar ist. Mit Wissen über den seismischen Momenttensor kann die Position der Quelle bestimmt werden, selbst wenn nur ein Empfänger pro Würfelseite platziert wurde. Abschließend wurde die Methode zur Zeitumkehrung von seismischen Wellen auf das Testproblem WP2_LOH1 angewandt. Damit wurde visuell bestätigt, dass auch in Medien realistischen Ausmaßes eine Zeitumkehrung möglich ist.

Contents

Glossary

EM Envelope misfit between two signals.

M_{ij} Seismic moment tensor, the unit [Nm] is implicitly assumed.

PM Phase misfit between two signals.

RMS Root-mean-square-error when comparing two signals.

T_{fwd} End time of the forward simulation.

T_{tr} End time of the time-reversed simulation.

Δx Distance between two receivers on the grid on the surface, measured in [m].

λ First Lamé parameter. Unless otherwise indicated its unit is always assumed to be [Pa].

μ Second Lamé parameter. Unless otherwise indicated its unit is always assumed to be [Pa].

ψ_p Wavelength of the P-Wave.

ψ_s Wavelength of the S-Wave.

ρ Density of a medium. Unless otherwise indicated its unit is always assumed to be [kg/m^3].

σ_{ij} Stress tensor.

t_{conv} Point in time where the converging wave in the time-reversal is converged.

t_{max} Point in time where the source function is at its peak.

v_p Wavelength of the P-Wave.

v_s Wavelength of the S-Wave.

ADER Arbitrary high-order DERivatives.

DG Discontinuous Galerkin.

IDW Inverse Distance Weighting interpolation technique.

TRC Time Reversal Cavity.

TRM Time Reversal Mirror.

Chapter 1

Introduction

Earthquakes, as experienced across the entire globe, are inevitable. They cause both economic damage and a large number of human casualties. Studying seismic phenomena helps to understand where earthquakes are most destructive, and can thus provide a perspective where e.g. earthquake resistant measures are most necessary.

The recent advances in super-computing have created large-scale possibilities to model realistic 3D earthquake events, something that 20 years ago was not possible. Modern simulation software relies heavily on numerics. The volume in question is discretized into smaller elements and numerical solvers are applied in each element in order to obtain a solution to the entire problem. Numerical methods to solve seismic wave equations range from e.g. finite difference (FD) schemes ([Mad76]) to spectral element methods (SEM) ([PCS94]).

SeisSol[1] is a scientific software both for the simulation of seismic waves and of earthquake phenomena. Modelling complex 3D geometries is computationally very expensive. Using an unstructured tetrahedral mesh has proven valuable in these scenarios ([DK06]). A range of different scenarios can be studied using SeisSol. The material can be adjusted to exhibit elastic, viscoelastic, or viscoplastic properties. SeisSol uses an approach that combines the Discontinuous Galerkin (DG) method with a time-integration using Arbirary high-order DERivatives (ADER), resulting in the ADER-DG approach ([Dum03]). Dumbser *et al.* extended this approach to solve the elastic wave equations in three dimensions ([DK06]). ADER-DG yields arbitrary high-order accuracy in both time and space. The solution in each element is approximated by polynomials, where the degrees of freedom are expressed through the coefficients of the polynomial. During a simulation, these coefficients are advanced in time, allowing for discontinuities across element boundaries ([KD05]).

In this work, SeisSol is used to create a time-reversal of seismic waves. Time-reversal methods have been studied in acoustic media, mainly to achieve a focusing of the wave below the diffraction limit ([Fin+89]). It can e.g. be used to better locate gallstones in the human body ([Fin97]). The experimental setup used by Fink *et al.* consists of a cavity surrounded by transducers that record the outward propagating acoustic pressure. These waves are distorted by inhomogeneities inside the cavity. In the second step, the same transducers act as transmitters, resulting in the propagation of a converging wave, focused at the original source location.

In the simulation environment, the volume in which the wave propagation is calculated corresponds to the cavity from the experimental setup. Instead of transducers, receiver locations are set on the surface of the volume, recording the time evolution of the incoming wave. In the second step, the boundary conditions of the volume are changed, thus creating sources at the boundary. When successful, the time-reversed wave propagating through the medium converges towards the original source. This provides a novel approach to determine

[1] https://github.com/SeisSol/SeisSol (2021, May 10)

the epicenter of an earthquake. Most commonly, an epicenter is found using a triangulation approach with signals from at least three seismographs. The time-reversal presented here, is in its simplest form not applicable in real world scenarios, as seismographs cannot be placed on all faces of a 3D volume encompassing the source of an earthquake. Nevertheless, showing a successful time-reversal of seismic waves is an instrumental first step.

This thesis is structured as follows. Chapter 2 focuses on the fundamental theory of elastic wave propagation and the presentation of the numerical ADER-DG scheme used in SeisSol. The equation of motion in elastic media is derived and the wave equation presented in the velocity-stress formulation. Chapter 3 is split into two parts. In the first part, the theory of the time-reversal is presented, which allows us to time-reverse the entire wavefield in the 3-dimensional volume. Subsequently, the latter part details the implementation of the time-reversal method into the existing SeisSol simulation. In the following chapters, Chapter 4 and 5, the method and the results are presented, beginning by elaborating on the setting used in the analysis, including the description of the source and the measures used to compare the forward and time-reversed direction (Chapter 4). Here, the time-frequency representation of signals is introduced, to serve as a measure to evaluate the goodness-of-fit between the original and the time-reversed wave. Chapter 5 then displays the results on the background of the knowledge obtained in previous chapters. At first, a homogeneous acoustic medium is analysed to obtain a proof of concept. Thereafter, inhomogeneities are added and the transition to elastic media is performed. In addition, experiments in which the number of receivers is reduced are conducted. Lastly, the time-reversal procedure is applied to a well known 3-dimensional test problem composed of a layer over a halfspace, WP2_LOH1. Finally, the findings are discussed and an outlook to possible future research directions is provided (Chapter 6).

Chapter 2

Seismic Waves

In this chapter, we will lay the theoretical foundations of this thesis. First, we will derive the basic equations for elastic wave propagation and show the equation of motion in velocity-stress formulation. Throughout this thesis, we consider isotropic media only, and make use of this assumption in certain symmetry arguments. The restriction to isotropic media is a commonly made simplification, which is also employed in e.g. [DK06]. In view of the analysis conducted in chapter 5, we will highlight additional simplifications valid in isotropic, homogeneous, acoustic media.

Subsequently, the simulation software used to obtain the results is presented. SeisSol[1] is used to numerically simulate seismic wave phenomena. SeisSol combines the Discontinuous Galerkin (DG) Finite Element (FE) method with a time integration scheme based on the solution of Arbitrary high-order DErivatives Riemann problems (ADER) [Käs+10] [DK06]. Combined, this approach is coined ADER-DG and will be introduced briefly in the following.

2.1 Elastic Wave Equation

An elastic medium is characterized by an undeformed state, in which stresses and strains are zero, to which it will return to in the absence of outer forces. If the stresses and strains the medium experiences are infinitesimal, the theory of linear elasticity applies. We define the displacement vector $\mathbf{U}$ describing the shortest distance between the initial and current position of a point. The particle velocities u, v and w in x-, y- and z-direction, respectively, can then be defined as the temporal derivative of $\mathbf{U}$

$$\begin{aligned} \frac{\partial}{\partial t} U_x &= \dot{U}_x = u \\ \frac{\partial}{\partial t} U_y &= \dot{U}_y = v \\ \frac{\partial}{\partial t} U_z &= \dot{U}_z = w, \end{aligned} \tag{2.1}$$

where the subscript indicates the coordinate direction and a dot over a variable refers to the partial time derivative. In short, we can thus write

$$\frac{\partial}{\partial t} U_i = \partial_t U_i = \dot{U}_i = V_i, \tag{2.2}$$

where we introduced the velocity vector $\mathbf{V}$.

[1] https://github.com/SeisSol/SeisSol

In linear elasticity the following generalization of Hooke's law is valid

$$\sigma_{ij} = c_{ijkl}\epsilon_{kl}, \tag{2.3}$$

with the medium specific constants c_{ijkl}. Note that we are using the Einstein summation convention, i.e. when an index appears twice, we sum over all possible values. Here and in the following σ_{ij} refers to the stress tensor and ϵ_{kl} to the strain tensor. Hooke's law therefore states that components of the stress tensor are a linear combination of components of the strain tensor. Continuing with infinitesimal small perturbations, the components of the strain tensor ϵ_{kl} are defined as

$$\epsilon_{kl} = \frac{1}{2}\left(\partial_k U_l + \partial_l U_k\right), \tag{2.4}$$

where ∂_k is the spatial derivative in k-direction and U_i the displacement in i-direction. As mentioned earlier, our interest lies in the velocity-stress formulation, as opposed to the displacement -stress formulation. Hence, in order to eliminate the displacements U_i, we used the velocities V_i as introduced in eq. 2.2. Thus yielding the time derivative of the strain tensor

$$\dot{\epsilon}_{kl} = \frac{1}{2}(\partial_k V_l + \partial_l V_k), \tag{2.5}$$

dependent on the spatial derivatives of the velocities V_i. Thereupon, it is trivial to express the time derivative of the stress tensor, keeping in mind that c_{ijkl} are constant over time

$$\dot{\sigma}_{ij} = c_{ijkl}\dot{\epsilon}_{kl}. \tag{2.6}$$

Returning to the forth-order tensor c_{ijkl} in equation 2.3, symmetry considerations can reduce the number of independent components from 81 to 21 (cf. [AR02] Chapter 2). In isotropic media only two constants remain to define the entire tensor. Its general form is then

$$c_{ijkl} = \lambda\delta_{ij}\delta_{kl} + \mu(\delta_{ik}\delta_{jl} + \delta_{il}\delta_{jk}), \tag{2.7}$$

where δ_{ij} is the Kronecker-delta and constants λ and μ are known as the Lamé moduli. Depending on the context, other expressions can be used instead of the Lamé parameters, i.e. μ is equal to the shear modulus G. Here, we kept the constants μ and λ as is common in seismology.

Following the derivation laid out in [AR02] we will now derive the equation of motion in a given volume V with surface S. The rate of change of momentum of particles inside the volume is equal to the forces acting on those particles. Thus, the forces acting on a particle consist of the body force and a surface force, which arises due to normal and shear stresses. Combined this leads to

$$\frac{\partial}{\partial t}\int_V \rho\frac{\partial \mathbf{U}}{\partial t}\mathrm{d}V = \int_V \mathbf{f}\,\mathrm{d}V + \int_S \mathbf{T}(\mathbf{n})\,\mathrm{d}S, \tag{2.8}$$

where $\int_v \rho\frac{\partial \mathbf{U}}{\partial t}\mathrm{d}V$, with mass density ρ, is the momentum of the particles in volume V, and $\mathbf{T}$ the traction vector which Cauchy's stress theorem relates to the stress tensor by

$$T_j(n) = \sigma_{ij}n_i, \tag{2.9}$$

with the normal vector n_i. Replacing $\mathbf{T}$ in the rightmost term in the equation above with the newfound expression and applying Gauss's divergence theorem yields

$$\int_S T_j \,\mathrm{d}S = \int_S \sigma_{ij} n_i \,\mathrm{d}S = \int_V \partial_i \sigma_{ij} \,\mathrm{d}V. \tag{2.10}$$

By rearranging and inserting this result into equation 2.8, we obtain

$$\int_V (\rho \ddot{U}_i - f_i - \partial_j \sigma_{ij}) \,\mathrm{d}V = 0, \tag{2.11}$$

where we have exploited the symmetry of the stress tensor[2] and a variant of Fubini's theorem that allows us to swap the time derivative and integration. Finally, since this is true for a general volume V, the integrand must be zero wherever is continuous, otherwise a volume violating eq. 2.11 could be found ([AR02]). Therefore,

$$\rho \ddot{U}_i = f_i + \partial_j \sigma_{ij}, \tag{2.12}$$

where we tacitly made use of the Einstein summation convention, i.e.

$$\rho \frac{\partial}{\partial t} V_i = f_i + \partial_x \sigma_{xi} + \partial_y \sigma_{yi} + \partial_z \sigma_{zi}, \tag{2.13}$$

and again expressed the displacements U_i in terms of the velocities V_i. The body force f_i will later be accounted for in the source term.

Combining the previous results from equations 2.6, 2.7, and 2.13, we arrive at the 3D elastic wave equation for an isotropic medium in velocity-stress formulation

$$\begin{aligned}
\frac{\partial}{\partial t}\sigma_{xx} - (\lambda+2\mu)\frac{\partial}{\partial x}u - \lambda\frac{\partial}{\partial y}v - \lambda\frac{\partial}{\partial z}w &= S_1,\\
\frac{\partial}{\partial t}\sigma_{yy} - \lambda\frac{\partial}{\partial x}u - (\lambda+2\mu)\frac{\partial}{\partial y}v - \lambda\frac{\partial}{\partial z}w &= S_2,\\
\frac{\partial}{\partial t}\sigma_{zz} - \lambda\frac{\partial}{\partial x}u - \lambda\frac{\partial}{\partial y}v - (\lambda+2\mu)\frac{\partial}{\partial z}w &= S_3,\\
\frac{\partial}{\partial t}\sigma_{xy} - \mu\left(\frac{\partial}{\partial x}v + \frac{\partial}{\partial y}u\right) &= S_4,\\
\frac{\partial}{\partial t}\sigma_{yz} - \mu\left(\frac{\partial}{\partial z}v + \frac{\partial}{\partial y}w\right) &= S_5,\\
\frac{\partial}{\partial t}\sigma_{xz} - \mu\left(\frac{\partial}{\partial z}u + \frac{\partial}{\partial x}w\right) &= S_6,\\
\rho\frac{\partial}{\partial t}u - \frac{\partial}{\partial x}\sigma_{xx} - \frac{\partial}{\partial y}\sigma_{xy} - \frac{\partial}{\partial z}\sigma_{xz} &= \rho S_7,\\
\rho\frac{\partial}{\partial t}v - \frac{\partial}{\partial x}\sigma_{xy} - \frac{\partial}{\partial y}\sigma_{yy} - \frac{\partial}{\partial z}\sigma_{yz} &= \rho S_8,\\
\rho\frac{\partial}{\partial t}w - \frac{\partial}{\partial x}\sigma_{xz} - \frac{\partial}{\partial y}\sigma_{yz} - \frac{\partial}{\partial z}\sigma_{zz} &= \rho S_9,
\end{aligned} \tag{2.14}$$

where $S_p(\mathbf{x}, t)$, $p = 1, \ldots, 9$, is a vector containing the space-time dependent source terms. It should be pointed out that the time and space dependencies are skipped throughout this

[2] That $\sigma_{ij} = \sigma_{ji}$ can easily be shown starting with the conservation of angular momentum and again applying Gauss's divergence theorem.

thesis. The stresses and velocities will in general be functions of both time $t \in \mathbb{R}$ and space $\mathbf{x} = (x, y, z)^T \in \mathbb{R}^3$, although the space dependency disappears when fixing the evaluation of stresses and velocities at a specific point. In addition, λ, μ, and ρ are functions of space, but constant in time.

Before drawing further conclusions from this system of equations, one more parameter, the propagation velocity of elastic waves, needs to be taken into account. In elastic media we will later observe two distinct waves, a compression (or longitudinal) and a shear (or transverse) wave, later to be called P- and S-waves, respectively.

Inserting the definition of σ_{ij} (eq. 2.3) and the constants c_{ijkl} from equation 2.7 into the equation of motion (2.12), one simply verifies that

$$\rho \ddot{U}_i = (\lambda + \mu)\partial_i \partial_j u_j + \mu \partial_j \partial_j u_i, \tag{2.15}$$

where the source term was set to zero. To convert this equation to a matrix equation, we make use of the following vector identity

$$\nabla \times (\nabla \times \mathbf{U}) = \nabla(\nabla \cdot \mathbf{U}) - \nabla^2 \mathbf{U}. \tag{2.16}$$

Notice that the last term on the right hand side already contains the derivatives present in the last term in eq. 2.15. Recalling that

$$\nabla(\nabla \cdot \mathbf{U}) = \begin{pmatrix} \partial_{xx} U_1 + \partial_{xy} U_2 + \partial_{xz} U_3 \\ \partial_{yx} U_1 + \partial_{yy} U_2 + \partial_{yz} U_3 \\ \partial_{zx} U_1 + \partial_{zy} U_2 + \partial_{zz} U_3 \end{pmatrix}, \tag{2.17}$$

we can easily identify it with the first part of eq. 2.15. Combining these results yields:

$$\begin{aligned} \rho \ddot{\mathbf{U}} &= (\lambda + \mu)\nabla(\nabla \cdot \mathbf{U}) + \mu \nabla^2 \mathbf{U} \\ &= (\lambda + \mu)\nabla(\nabla \cdot \mathbf{U}) - \mu \nabla \times (\nabla \times \mathbf{U}) + \mu \nabla(\nabla \cdot \mathbf{U}), \end{aligned} \tag{2.18}$$

which then finally can be combined to

$$\rho \ddot{\mathbf{U}} = (\lambda + 2\mu)\nabla(\nabla \cdot \mathbf{U}) - \mu \nabla \times (\nabla \times \mathbf{U}). \tag{2.19}$$

In order to derive the propagation velocities, we will now distinguish between an irrotational (i.e. curl-free) and a solenoidal (i.e. divergence-free) displacement. Firstly, for a displacement that is irrotational we, by definition, have $\nabla \times \mathbf{U}_p = 0$. Thus, the matrix equation above simplifies to

$$\frac{\partial^2 \mathbf{U}_p}{\partial t^2} = \frac{\lambda + 2\mu}{\rho} \nabla(\nabla \cdot \mathbf{U}_p). \tag{2.20}$$

Rearranging the vector identity from eq. 2.16, we obtain the basic wave equation

$$\frac{\partial^2 \mathbf{U}_p}{\partial t^2} = \frac{\lambda + 2\mu}{\rho} \nabla^2 \mathbf{U}_p = v_p^2 \nabla^2 \mathbf{U}_p, \tag{2.21}$$

where we introduced the propagation velocity

$$v_p = \sqrt{\frac{\lambda + 2\mu}{\rho}}. \tag{2.22}$$

Analogously, we proceed with the next distinction, a solenoidal displacement $\mathbf{U}_s$, i.e. $\nabla \cdot \mathbf{U}_s = 0$. Thus, the vector identity from eq. 2.16 reduces to $\nabla \times (\nabla \times \mathbf{U}_s) = -\nabla^2 \mathbf{U}_s$; simplifying equation 2.19 similarly to before yields

$$\frac{\partial^2 \mathbf{U}_s}{\partial t^2} = \frac{\mu}{\rho} \nabla^2 \mathbf{U}_s = v_s^2 \nabla^2 \mathbf{U}_s, \tag{2.23}$$

again introducing a propagation velocity,

$$v_s = \sqrt{\frac{\mu}{\rho}}. \tag{2.24}$$

As already hinted at earlier, these two velocities are the propagation velocities of the longitudinal P-wave (also called the primary wave) and the transverse S-wave (also known as the secondary or shear wave), respectively.

The theory of elastic wave propagation is easily simplified to the acoustic case by setting $\mu = 0$ in all equations. In order to provide a proof of concept, we will later begin by time-reversing acoustic waves (cf. sec. 5.1), before moving on to the elastic case. The important simplifications are therefore stated in the following. One of the main differences between elastic and acoustic media is the phenomenon of shear waves. These S-waves do not occur in acoustic media. This can easily be seen from equation 2.24, where, when $\mu = 0$, also $v_s = 0$. Thus following our intuition that sound waves propagate solely as longitudinal waves in e.g. air and water. We therefore expect a single wave travelling with the velocity

$$v_{p,\text{ acoustic}} = \sqrt{\frac{\lambda}{\rho}}. \tag{2.25}$$

Further simplifications can be made when examining the system 2.14. Immediately, one observes that the time derivative of the off-diagonal elements of σ_{ij} is zero. Looking at the displacement-stress formulation, we can conclude even more, that is

$$\sigma_{ij} = 0, \text{ for } i \neq j. \tag{2.26}$$

Continuing to look at system 2.14 in displacement-stress formulation[3], we find that all three equations describing the diagonal elements can be condensed to one, namely $\sigma_{ii} = \lambda \partial_j u_j$, implying that

$$p := \sigma_{xx} = \sigma_{yy} = \sigma_{zz} = \lambda \partial_i u_i, \tag{2.27}$$

where we again make use of Einstein's summation convention. Finally, the equation of motion can be rewritten to

$$\rho \frac{\partial^2 \mathbf{u}_i}{\partial t^2} - \partial_i p = 0. \tag{2.28}$$

2.2 ADER-DG

In this section, we will elaborate on the basic elements of the ADER-DG method, a fundamental part in SeisSol. The intention is to give the reader an overview over the most important aspects, focusing on what will later be relevant in the implementation of the time-reversal. For a thorough presentation of ADER-DG and its roots in generalised Riemann problems, the interested reader is referred to [TMN01], [TT02], [DM05], [KD05], [DK06], [Käs+10].

[3]The displacement-stress formulation can easily be obtained by following the same process outlined above with $\sigma_{ij} = c_{ijkl}\epsilon_{kl}$ instead of the using $\dot{\sigma}_{ij}$.

2.2.1 Discontinuous Galerkin Method

As we have seen in the previous section, we want to solve the elastic wave question formulated as a linear hyperbolic system. In 1973, Reed and Hill ([RH73]) first used the Discontinuous Galerkin (DG) Finite-Element method to obtain a solution of this kind of problem. In 2001, Toro *et al.* developed the idea of arbitrary high order generalized Riemann solvers in a finite volume framework and coined the approach ADER (Arbitrary high-order schemes using DERivatives). Here, we will present the combination of solving generalized Riemann problems with Discontinuous Galerkin methods, resulting in the ADER-DG approach [DM06]. We allow piecewise polynomial approximations in order to reuse the theory of fluxes across element boundaries from the finite volume methods. The ADER-DG scheme provides, similar to the original ADER idea, an explicit, one-step scheme. That is, to advance the solution by a full time step, only the computation of inter-cell fluxes is required. To achieve arbitrary high-order accuracy in both space and time, the time derivatives are replaced with space derivatives using the Cauchy-Kowalevski or Lax-Wendroff procedure.

In the following, we will present the ADER-DG approach to solve the 3D elastic wave equation on tetrahedral meshes (cf. [DK06]). We begin by transforming the system of equations 2.14 into the more compact form

$$\frac{\partial Q_p}{\partial t} + A_{pq}\frac{\partial Q_q}{\partial x} + B_{pq}\frac{\partial Q_q}{\partial y} + C_{pq}\frac{\partial Q_q}{\partial z} = 0, \tag{2.29}$$

where **Q** is the vector containing the stresses and velocities, i.e.

$$Q_p = (\sigma_{xx}, \sigma_{yy}, \sigma_{zz}, \sigma_{xy}, \sigma_{yz}, \sigma_{xz}, u, v, w)^T \tag{2.30}$$

and A_{pq}, B_{pq}, and C_{pq} are space-dependent Jacobian matrices. It can be easily verified that

$$A_{pq} = \begin{pmatrix} 0 & 0 & 0 & 0 & 0 & 0 & -(\lambda+2\mu) & 0 & 0 \\ 0 & 0 & 0 & 0 & 0 & 0 & -\lambda & 0 & 0 \\ 0 & 0 & 0 & 0 & 0 & 0 & -\lambda & 0 & 0 \\ 0 & 0 & 0 & 0 & 0 & 0 & 0 & -\mu & 0 \\ 0 & 0 & 0 & 0 & 0 & 0 & 0 & 0 & 0 \\ 0 & 0 & 0 & 0 & 0 & 0 & 0 & 0 & -\mu \\ -\frac{1}{\rho} & 0 & 0 & 0 & 0 & 0 & 0 & 0 & 0 \\ 0 & 0 & 0 & -\frac{1}{\rho} & 0 & 0 & 0 & 0 & 0 \\ 0 & 0 & 0 & 0 & 0 & -\frac{1}{\rho} & 0 & 0 & 0 \end{pmatrix}. \tag{2.31}$$

Matrices B_{pq} and C_{pq} are similar, the non-zero entries are just shifted around (all three matrices are explicitly stated in [DK06]).

We begin by dividing the computational domain $\Omega \in \mathbb{R}^3$ into tetrahedral elements $\mathcal{T}^{(m)}$, with unique indices $m \in \mathbb{N}$. The above mentioned matrices A_{pq}, B_{pq}, and C_{pq} are assumed to be piecewise constant inside each $\mathcal{T}^{(m)}$. In addition, we introduce (ξ, η, ζ) as a new coordinate frame of a reference tetrahedron $\mathcal{T}_E$ (cf. fig. 2.1)

Thus, we require a transformation T_{pq} to transform the vector Q_p, here $p = 1, \ldots, 9$ expresses the unknowns of the governing equation, from the global Cartesian system to the vector Q_p^n in the normal, face-aligned frame, such that

$$Q_p = T_{pq} Q_q^n. \tag{2.32}$$

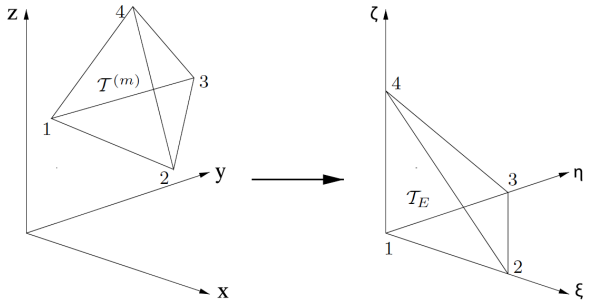

Figure 2.1: Transforming the physical tetrahedron $\mathcal{T}^{(m)}$ to the canonical reference tetrahedron $\mathcal{T}_E$ using the transformation matrix T_{pq}. (Figure taken from Figure 1 in [DK06])

It is given by

$$T_{pq} = \begin{pmatrix} n_x^2 & s_x^2 & t_x^2 & 2n_x s_x & 2s_x t_x & 2n_x t_x & 0 & 0 & 0 \\ n_y^2 & s_y^2 & t_y^2 & 2n_y s_y & 2s_y t_y & 2n_y t_y & 0 & 0 & 0 \\ n_z^2 & s_z^2 & t_z^2 & 2n_z s_z & 2s_z t_z & 2n_z t_z & 0 & 0 & 0 \\ n_y n_x & s_y s_x & t_y t_x & n_y s_x + n_x s_y & s_y t_x + s_x t_y & n_y t_x + n_x t_y & 0 & 0 & 0 \\ n_z n_y & s_z s_y & t_z t_y & n_z s_y + n_y s_z & s_z t_y + s_y t_z & n_z t_y + n_y t_z & 0 & 0 & 0 \\ n_z n_x & s_z s_x & t_z t_x & n_z s_x + n_x s_z & s_z t_x + s_x t_z & n_z t_x + n_x t_z & 0 & 0 & 0 \\ 0 & 0 & 0 & 0 & 0 & 0 & n_x & s_x & t_x \\ 0 & 0 & 0 & 0 & 0 & 0 & n_y & s_y & t_y \\ 0 & 0 & 0 & 0 & 0 & 0 & n_z & s_z & t_z \end{pmatrix}, \quad (2.33)$$

where $\mathbf{n} = (n_x, n_y, n_z)^T$ are the components of the normal vector, and $\mathbf{s} = (s_x, s_y, s_z)^T$ and $\mathbf{t} = (t_x, t_y, t_z)^T$ are two tangential vectors, which lie in the plain determined by the boundary face of the tetrahedron. It is common to define the vector $\mathbf{s}$ such that it points from face node 1 to face node 2 (node numbers can also be seen in fig. 2.1). Of course, $\mathbf{n}$, $\mathbf{s}$, and $\mathbf{t}$ are orthogonal to each other. In addition, the physical coordinates (x, y, z) need to be mapped to the coordinates in the reference element (ξ, η, ζ) with

$$Q_p^{(m)}(x, y, z, t) = \hat{Q}_{pl}^{(m)}(t)\Psi_l(x, y, z), \quad (2.34)$$

where $\Psi_l(x, y, z)$ are pure spatial polynomial basis functions, defined on the physical element. With a suitable coordinate transformation M, equation 2.34 can now be expressed in the frame of the reference element

$$Q_p^{(m)}(x, y, z, t) = \hat{Q}_{pl}^{(m)}(t)\Psi_l(M(\xi, \eta, \zeta)). \quad (2.35)$$

We can now define spatial polynomial basis functions on the reference element $\Phi_l(\xi, \eta, \zeta)$. The coordinate transformation is applied to make the implementation more efficient, as integrals in the reference system can be computed beforehand. In order to express the numerical solution Q_h by a linear combination of pure spatial and pure time-dependent functions, the time-dependent degrees of freedom $\hat{Q}_{pl}^m(t)$ are introduced. As Φ_l is defined with support $\mathcal{T}^m$, we can approximate Q_h in each tetrahedron

$$[Q_h^{(m)}]_p(\xi, \eta, \zeta, t) = \hat{Q}_{pl}^m(t)\Phi_l(\xi, \eta, \zeta), \quad (2.36)$$

where l denotes the lth basis function. Multiplying eq. 2.29 with the test function Ψ_k (as given in [CKS11]) and integrating over a tetrahedral element $\mathcal{T}^{(m)}$ yields

$$\int_{\mathcal{T}^{(m)}} \Psi_k \frac{\partial Q_p}{\partial t} \mathrm{d}V + \int_{\mathcal{T}^{(m)}} \Psi_k \left(A_{pq} \frac{\partial Q_q}{\partial x} + B_{pq} \frac{\partial Q_q}{\partial y} + C_{pq} \frac{\partial Q_q}{\partial z} \right) \mathrm{d}V = 0, \quad (2.37)$$

thus moving over to a weak formulation. Introducing the flux F_p^h, to take discontinuities in Q_h at element boundaries into account and integrating by parts, yields

$$\int_{\mathcal{T}^{(m)}} \Psi_k \frac{\partial Q_p}{\partial t} \mathrm{d}V + \int_{\partial\mathcal{T}^{(m)}} \Psi_k F_p^h \mathrm{d}S - \int_{\mathcal{T}^{(m)}} \left(\frac{\partial \Psi_k}{\partial x} A_{pq} Q_q + \frac{\partial \Psi_k}{\partial y} B_{pq} Q_q + \frac{\partial \Psi_k}{\partial z} C_{pq} Q_q \right) \mathrm{d}V = 0. \quad (2.38)$$

The flux for tetrahedron $\mathcal{T}^{(m)}$ with boundary extrapolated numerical solution $\hat{Q}_{sl}^{(m)} \Psi_l^{(m)}$ across the boundary of one of the neighbouring tetrahedra $\mathcal{T}^{(m_j)}$ with $j = 1, 2, 3, 4$, and $\hat{Q}_{sl}^{(m_j)} \Psi_l^{(m_j)}$, in the global, Cartesian system can then be computed with the Jacobian matrix A_{pq} (eq. 2.31)

$$F_p^h = \frac{1}{2} T_{pq} \left(A_{qr}^{(m)} + \mid A_{qr}^{(m)} \mid \right) (T_{rs})^{-1} \hat{Q}_{sl}^{(m)} \Psi_l^{(m)} + \frac{1}{2} T_{pq} \left(A_{qr}^{(m)} + \mid A_{qr}^{(m)} \mid \right) (T_{rs})^{-1} \hat{Q}_{sl}^{(m_j)} \Psi_l^{(m_j)}. \quad (2.39)$$

It remains to be clarified that

$$\mid A_{qr}^{(m)} \mid = R_{qp}^A \mid \Lambda_{ps} \mid (R_{sr}^A)^{-1}, \quad (2.40)$$

where Λ is a diagonal matrix containing the eigenvalues of A_{pq} and R_{pq} a matrix containing the nine right eigenvectors of A_{pq}. We can now insert the flux calculation from eq. 2.39 and the definition of the numerical solution Q_h from eq. 2.36 into the weak formulation in eq. 2.38. Since the basis functions Φ_l are defined in (ξ, η, ζ)-space we additionally need to transform the resulting equation using

$$\mathrm{d}x\mathrm{d}y\mathrm{d}z = \mid J \mid \mathrm{d}\xi\mathrm{d}\eta\mathrm{d}x\zeta \quad (2.41)$$

and special linear combinations of the Jacobians

$$\begin{aligned} A_{pq}^* &= A_{pq} \frac{\partial \xi}{\partial x} + B_{pq} \frac{\partial \xi}{\partial y} + C_{pq} \frac{\partial \xi}{\partial z}, \\ B_{pq}^* &= A_{pq} \frac{\partial \eta}{\partial x} + B_{pq} \frac{\partial \eta}{\partial y} + C_{pq} \frac{\partial \eta}{\partial z}, \\ C_{pq}^* &= A_{pq} \frac{\partial \zeta}{\partial x} + B_{pq} \frac{\partial \zeta}{\partial y} + C_{pq} \frac{\partial \zeta}{\partial z}. \end{aligned} \quad (2.42)$$

Then, finally yielding the ODE system describing the semi-discrete DG formulation in the reference element $\mathcal{T}_E$

$$\begin{aligned} &\frac{\partial}{\partial t} \hat{Q}_{pl}^{(m)} \mid J \mid \int_{\mathcal{T}_E} \Phi_k \Phi_l \mathrm{d}\xi\mathrm{d}\eta\mathrm{d}\zeta \\ &+ \sum_{j=1}^{4} T_{pq}^j \frac{1}{2} \left(A_{qr}^{(m)} + \mid A_{qr}^{(m)} \mid \right) (T_{rs}^j)^{-1} \hat{Q}_{sl}^{(m)} \mid S_j \mid F_{kl}^{-,j} \\ &+ \sum_{j=1}^{4} T_{pq}^j \frac{1}{2} \left(A_{qr}^{(m)} + \mid A_{qr}^{(m)} \mid \right) (T_{rs}^j)^{-1} \hat{Q}_{sl}^{(m_j)} \mid S_j \mid F_{kl}^{-,j,i,h} \\ &- A_{pq}^* \hat{Q}_{ql}^{(m)} \mid J \mid \int_{\mathcal{T}_E} \frac{\partial \Phi_k}{\partial \xi} \Phi_l \mathrm{d}\xi\mathrm{d}\eta\mathrm{d}\zeta - B_{pq}^* \hat{Q}_{ql}^{(m)} \mid J \mid \int_{\mathcal{T}_E} \frac{\partial \Phi_k}{\partial \eta} \Phi_l \mathrm{d}\xi\mathrm{d}\eta\mathrm{d}\zeta - C_{pq}^* \hat{Q}_{ql}^{(m)} \mid J \mid \int_{\mathcal{T}_E} \frac{\partial \Phi_k}{\partial \zeta} \Phi_l \mathrm{d}\xi\mathrm{d}\eta\mathrm{d}\zeta \\ &= 0, \end{aligned} \quad (2.43)$$

with the area of tetrahedron face j, $\mid S_j \mid$.

2.2.2 ADER-DG Time Discretization

Instead of now applying the Runge-Kutta method to the DG formulation to obtain a Runge-Kutta DG scheme, which essentially is limited to the fourth order, we apply the ADER approach to achieve arbitrary high-order accuracy in both space and time. Runge-Kutta schemes of order higher than 4 become increasingly inefficient as the required number of calculation steps supersedes the order of accuracy. These are the so-called Butcher barriers ([But87]). Applying the ADER scheme to the DG formulation above results in the ADER-DG scheme. The key is to use the Cauchy-Kovalewski procedure to replace the time-derivatives by pure space derivatives. As a result, the Cauchy-Kovalewski procedure gives the kth time-derivative in the face-aligned coordinate system

$$\frac{\partial^k Q_p}{\partial t^k} = (-1)^k \left(A^*_{pq} \frac{\partial}{\partial \xi} + B^*_{pq} \frac{\partial}{\partial \eta} + C^*_{pq} \frac{\partial}{\partial \zeta} \right)^k Q_q. \tag{2.44}$$

Q_p can then be developed in a Taylor series in time, and the time derivatives replaced by space derivatives using the above equation (cf. Section 3.2 in [DK06]). By doing so, we achieve arbitrary high-order accuracy in both space and time. As mentioned earlier, the ADER-DG schemes perform time integration in a single time step, taking into account the current element and its j neighbours only, thus making the method ideal for parallelization. It has also been shown that ADER-DG is faster than e.g. a RK-DG scheme ([DM05].

2.2.3 Boundary Conditions

To conclude this section, some considerations about boundary conditions are made. Boundary conditions will be important again in the next section, where we impose Dirichlet boundary conditions on the surface of our volume to initialize the time-reversal.

Absorbing Boundaries

In the forward direction, the physical volume will be enclosed by absorbing boundaries, i.e. no waves are entering the computational domain and outgoing waves pass the boundary without being reflected. A closer look at eq. 2.39 reveals that the first term on the right-hand-side corresponds to the outflow from the current element, while the second term on the right-hand-side corresponds to the inflow from neighboring elements. Thus, not allowing for incoming waves corresponds to setting the second term to zero. Hence, the flux at all absorbing faces of the respective tetrahedral elements is set to

$$F_p^{\text{AbsorbBC}} = \frac{1}{2} T_{pq} \left(A^{(m)}_{qr} + |A^{(m)}_{qr}| \right) (T_{rs})^{-1} \hat{Q}^{(m)}_{sl} \Psi^{(m)}_l. \tag{2.45}$$

Free-Surface Boundaries

At a free-surface boundary the elastic medium is in contact with surrounding air or void. Since there are no external forces on the outside of the elastic medium, normal and shear stresses have to vanish at the free surface. This is achieved by creating ghost cells, where we mirror the stresses, i.e. the values have the same magnitude, but opposite sign. This is realized by using the flux function (cf. [DK06])

$$\begin{aligned} F_p^{\text{FreeBC}} =& \frac{1}{2} T_{pq} \left(A^{(m)}_{qr} + |A^{(m)}_{qr}| \right) (T_{rs})^{-1} \hat{Q}^{(m)}_{sl} \Psi^{(m)}_l \\ &+ \frac{1}{2} T_{pq} \left(A^{(m)}_{qr} + |A^{(m)}_{qr}| \right) \Gamma_{rs} (T_{rs})^{-1} \hat{Q}^{(m)}_{sl} \Psi^{(m)}_l, \end{aligned} \tag{2.46}$$

where $\Gamma_{rs} = \text{diag}(-1, 1, 1, -1, 1, -1, 1, 1, 1)$ is the matrix implementing the mirroring of normal and shear stresses.

Inflow Boundaries

At inflow boundaries, waves entering the computational domain are handled. Similar to Hermann's approach in [Her10], we define the incoming wave at each quadrature point n as $u_n^{p,\text{inflow},(m)}(\xi, \eta, \zeta, t)$ for each component p. However, contrary to Hermann, we do not integrate over all Gaussian points, but rather define a flux $F_{p,n}^{\text{Inflow}}$ at each point. The flux at an inflow boundary is then given by

$$\begin{aligned} F_{p,n}^{\text{Inflow}} = &\frac{1}{2} T_{pq} \left(A_{qr}^{(m)+} + |A_{qr}^{(m)}| \right) (T_{rs})^{-1} \hat{Q}_{sl}^{(m)} \Psi_l^{(m)} \\ &+ \frac{1}{2} T_{pq} \left(A_{qr}^{(m)+} + |A_{qr}^{(m)}| \right) (T_{rs})^{-1} u_n^{p,\text{Inflow},(m)}. \end{aligned} \tag{2.47}$$

Comparing this equation to the above mentioned flux for absorbing boundary conditions, it is apparent that this flux also acts as an absorbing boundary for outgoing waves.

Chapter 3

Time-Reversal

Time-reversal methods are concerned with mirroring the propagation of waves in time. After a successful time-reversal the resulting wave should converge at the source. There are mainly two different ways in which a time-reversal can be achieved ([FF17]). Time-reversal mirrors (TRMs) rely on the so-called Cauchy Boundary Conditions. If the wavefield and its normal derivative are known at the entire surface $\mathcal{S}$ surrounding the volume for all times t, the wavefield inside the entire volume can be calculated. Thus, the time-reversal is achieved by initially recording the outgoing wave on $\mathcal{S}$, then time-reversing it, and finally emitting the time-reversed field from $\mathcal{S}$.

Instead of examining boundary conditions, one can also achieve a time-reversal that relies on Cauchy Initial Conditions. Here, the wavefield and its normal derivative are known in the entire volume, but only for a specific time. Consider a N particle system, where each particle is described by a position and velocity vector $\{\mathbf{r}_i, \mathbf{v}_i\}$. Using Lohschmidt daemons, the velocity of each particle can be reversed instantaneously, i.e. $\{\mathbf{r}_i, -\mathbf{v}_i\}$, also yielding a time-reversed wave. This approach is called the instantaneous time-reversal mirror (ITM).

In this thesis, the focus lies on the approach of the TRM, as the wavefield can easily be recorded at the surface of a volume. To develop the theory, we will primarily focus on the so-called time-reversal cavity, which is an idealized version of the TRM, where the wave is recorded continuously on $\mathcal{S}$. Almost 30 years ago, Fink *et al.* wrote a series of papers examining the theory and presenting experimental results on the time-reversal of ultrasonic fields ([Fin92], [WTF92], [CF92b]). In the first part of this chapter, we will follow the theoretical foundation laid out in [CF92b], where Cassereau and Fink discuss the theory of the closed time-reversal cavity, pointing out changes when necessary. Note that although the derivation of Casserau and Fink is limited to acoustic waves, the time-reversal method is equally applicable to elastic waves ([FP01]). In the latter part of this chapter (sec. 3.2), we will present the implementation of the time-reversal in the numerical simulation software SeisSol. The description of the implementation remains as general as possible, such that this chapter provides a comprehensive understanding of the method. Details regarding the exact settings analysed in this thesis will be provided in the next chapter (4).

3.1 Theory of Time-Reversals

The concept of the time-reversal is a two step process. First, in the recording step, the wave field originating from a point source propagates through the volume and is recorded at the surface of the volume. The recording step is illustrated in fig. 3.1a. Receivers at the surface $\mathcal{S}$ record the time evolution of all entries of Q_p, as defined in eq. 2.30. Should inhomogeneities or material boundaries be present in the medium, a distorted wave front will be recorded

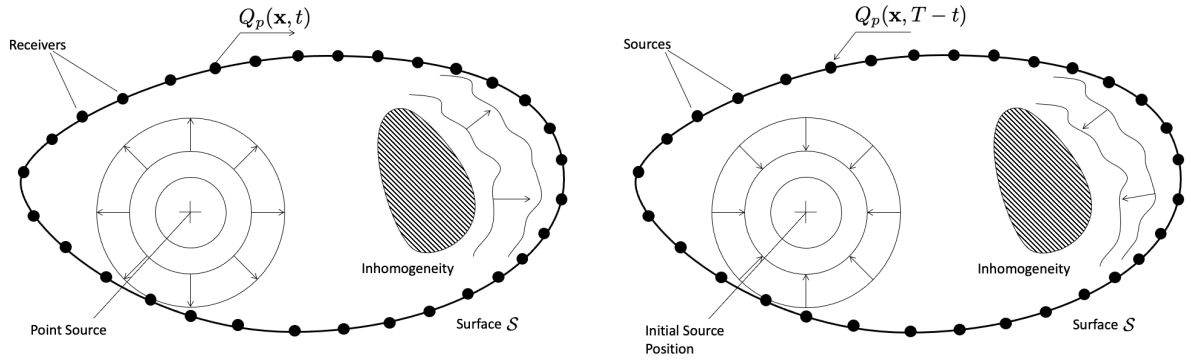

(a) Recording step: The wavefront originating from a point source propagates throughout the medium and is then recorded by receivers at the surface surrounding the volume.

(b) Reconstruction step: The recorded signals are time-reversed and the receivers now act as sources. Now the time-reversed field propagates in the medium and converges to the location of the initial source

Figure 3.1: Visualization of the recording and reconstruction step in the time-reversal process (adapted from fig. 1 in [FF17]).

by the receivers. Second, in the reconstruction step, the passive receivers from the first step become sources and emit the recorded field in a time-reversed manner, ideally creating a wave that converges back to the initial source position, as seen in fig. 3.1b.

The theory of the time-reversal is thus based on two fundamental principles. Firstly, the wave equation needs to be reversible in time. Examining the elastic wave equation from the previous chapter (2.19)

$$\rho\ddot{\mathbf{U}}(\mathbf{x},t) - (\lambda+2\mu)\nabla(\nabla\cdot\mathbf{U}(\mathbf{x},t)) + \mu\nabla\times(\nabla\times\mathbf{U}(\mathbf{x},t)) = \mathbf{S}(\mathbf{x},t), \tag{3.1}$$

with the source function $\mathbf{S}(\mathbf{x},t)$, it is evident that the wave equation only contains second-order time derivatives. Therefore, if $\tilde{\mathbf{U}}(\mathbf{x},t)$ is a solution, we know that $\tilde{\mathbf{U}}(\mathbf{x},-t)$ also has to be a solution to the equation, if $\mathbf{S}$ is symmetric in time. Secondly, a slightly modified version of the Helmholtz-Kirchhoff integral theorem is employed, that allows the recovery of the entire wave field at any time in the given volume, only knowing the outgoing wave field along the 2D surface $\mathcal{S}$ for a sufficient amount of time ([CF92b]).

One differentiates between the closed time-reversal cavity and the TRM. The closed time-reversal cavity is an idealized concept, where the surface $\mathcal{S}$, enclosing the entire volume in question, can continuously record the propagating wave field. That is, both time and space dimensions are recorded continuously. In the TRM, the receivers are spaced on a discrete grid. Fink claims in [FP01] that it suffices to space receivers $\psi_{\min}/2$ apart, where $\psi_{\min}$ is the smallest wavelength of the wave field, and a temporal resolution of $T_{\min}/8$ with $T_{\min}$ being the minimum period. In contrast to Fink *et al.*, who are mainly concerned with experimental setups, we can take advantage of conducting experiments in a simulation environment. That is, a mixture of both methods is employed, in the sense that a discrete number of receivers is placed on $\mathcal{S}$, but the surface can be continuously sampled using interpolation techniques. Nonetheless, it is instructive to inspect the theory in the ideal case.

In order for the time-reversal to make sense, in the recording step, the outgoing wave field needs to be recorded long enough, such that the wave actually passes through $\mathcal{S}$. We define T_{fwd} as the end time of the forward simulation, i.e. the outgoing wave field is recorded during the finite time interval $[0, T_{\text{fwd}}]$. T_{fwd} should be chosen large enough to allow the entire wave field to propagate out of the volume enclosed by $\mathcal{S}$. In mathematical terms we

define the function

$$H(t) = \begin{cases} 1 & \text{if } 0 \leq t \leq T_{\text{fwd}}, \\ 0 & \text{otherwise,} \end{cases} \tag{3.2}$$

such that the recorded wave field is $Q_p(\mathbf{x}, t)H(t)$. Contrary to the velocity-stress formulation depicted in Chapter 2, it should be noted that we use the differential equation describing the displacements to show the analogy to the acoustic wave equation. Note also that the receivers on the surface record Q_p and not the displacements $\mathbf{U}$. That is, after the recording step the recorded data contain the time evolution of the stress tensor σ_{ij} and the velocities v_i in all three coordinate directions.

The second step in the time-reversal process is the reconstruction step. Our goal is to create a wave that propagates from the boundary of the volume to the origin of the source inside the volume. In order to set a consistent wave field at the surface, we either set the six independent entries of σ_{ij} or the three velocities V_i at the surface. The results obtained are identical, up to a multiplication of -1 of the entire wave field, due to the fact that σ_{ij} is dependent on the spatial derivatives of the displacement, while V_i is dependent on the temporal derivative, thus adding a factor of -1 in the time-reversal.

In the following, when mentioning Q_p, we imply a lower dimensional object that guarantees the description of a well defined wave field, in our case

$$Q_p = (\sigma_{xx}, \sigma_{yy}, \sigma_{zz}, \sigma_{xy}, \sigma_{yz}, \sigma_{xz}). \tag{3.3}$$

Naturally, the time-reversed displacement $\mathbf{U}_{\text{TR}}$ also has to obey the elastic wave equation, with two modifications. Trivially, the original source is no longer present in the volume, i.e. $\mathbf{S}(\mathbf{x}, t) = 0$. Thereby yielding

$$\rho \ddot{\mathbf{U}}_{\text{TR}}(\mathbf{x}, t) - (\lambda + 2\mu)\nabla(\nabla \cdot \mathbf{U}_{\text{TR}}(\mathbf{x}, t)) + \mu \nabla \times (\nabla \times \mathbf{U}_{\text{TR}}(\mathbf{x}, t)) = 0. \tag{3.4}$$

Secondly, the boundary conditions (BCs) have changed. In the forward direction absorbing BCs were applied, in order to eliminate the reflection of waves back into the physical volume. In the time-reversed direction we require inflow BCs, thereby enabling the wave to propagate into the volume. The inflow is achieved by creating surface sources $\mathbf{S}_{\mathcal{S}}$ on $\mathcal{S}$ that are characterized by $Q_p(\mathbf{x}_i, T_{\text{fwd}} - t)H(T_{\text{fwd}} - t)$, where receivers are located at points x_i. Conceptually this is equal to playing the recorded receiver file backwards. Performing the time-reversal transformation from t to $T_{\text{fwd}} - t$ on the equation of motion (3.1) yields

$$\rho \ddot{\mathbf{U}}(\mathbf{x}, T_{\text{fwd}} - t) - (\lambda + 2\mu)\nabla(\nabla \cdot \mathbf{U}(\mathbf{x}, T_{\text{fwd}} - t) + \mu \nabla \times (\nabla \times \mathbf{U}(\mathbf{x}, t)) = \mathbf{S}(\mathbf{x}, T_{\text{fwd}} - t); \tag{3.5}$$

not only has the wave field on $\mathcal{S}$ been time-reversed, but also the source $\mathbf{S}$.

Fink *et al.* go on to find an equation for the time-reversed field by assuming an impulsive source

$$\mathbf{S}(\mathbf{x}, t) = \mathbf{S}(\mathbf{x})\delta_D(t), \tag{3.6}$$

where δ_D is the Dirac delta. In this thesis we however employ a source time function $S(t)$ located at a specific point. The source function is thus

$$\mathbf{S}(\mathbf{x}, t) = S(t)\delta_D(\mathbf{x} - \mathbf{x}_0), \tag{3.7}$$

a point source, but not impulsive in time. This is where we deviate from the theory of Fink *et al.* and move in a slightly different direction. The ultimate goal of Fink *et al.* is to achieve a focusing of waves below the diffraction limit. Our goal, however, is to determine the center

of an earthquake, i.e. the origin of the source, based on a recorded wave field. In addition, the theory for an impulsive diverging wave can be derived in a straight-forward fashion using a free-space Green's function. Finding a similar expression for a source as described by eq. 3.7 goes beyond the scope of this thesis. Hence, in the following we present an informal argument to obtain the time-reversed entries of Q_p, Q_p^{TR}, which agrees with the experimental results obtained in chapter 5.

It has been established that the recording time T_{fwd} has to be sufficiently large to allow most of the wave field to propagate out of the volume. In other words, when the simulation time approaches T_{fwd} the source function should be close to zero, otherwise a larger T_{fwd} should have been chosen. We define a new parameter τ that describes exactly this interval where the source function is close to zero. Namely, the time the wave takes to travel from the origin of the point source to the outermost point on $\mathcal{S}$. Evidently, the smallest propagation velocity has to be taken into account. We can thus assume that

$$S(t) = 0 \qquad \forall\, T_{\mathrm{fwd}} - \tau < t < T_{\mathrm{fwd}}, \tag{3.8}$$

or expressed for the time-reversed source

$$S(T_{\mathrm{fwd}} - t) = 0 \qquad \forall\, 0 < t < \tau. \tag{3.9}$$

Hence, eq. 3.4 holds for all $0 < t < \tau$. We have thus found a description of the time-reversed elements of Q_p^{TR} dependent on the original vector Q_p

$$Q_p^{\mathrm{TR}}(\mathbf{x}, t) = Q_p(\mathbf{x}, T_{\mathrm{fwd}} - t) \qquad \text{if } t < \tau. \tag{3.10}$$

Obviously, the backwards propagating wave will not magically disappear. Consider a source that is symmetric in time relative to the peak of the source function $t_{\max}$ (see fig. 3.2a). In the time-reversed direction the peak will arrive at the origin of the point source exactly at time $T_{\mathrm{fwd}} - t_{\max}$. The peak of the wave will then immediately start diverging, independent of the starting time of the original source function. This behavior is illustrated in fig. 3.2b. Now consider a receiver that is placed at some distance to the source. In the forward direction it will record a wave field, peaking at some time $T' > t_{\max}$. Fig. 3.2c shows the propagating wave field. The same receiver will record two signals in the time-reversal step (see fig. 3.2d). The first field is reversed in time compared to the original field. The second one however is merely translated in time. Since the converging wave immediately starts diverging at time $T_{\mathrm{fwd}} - t_{\max}$, a factor of 2 is present in the description of the diverging wave field

$$Q_p^{\mathrm{TR}}(\mathbf{x}, t) = Q_p(\mathbf{x}, t - (T_{\mathrm{fwd}} - 2 \cdot t_{\max})) \qquad \forall\, t > T_{\mathrm{fwd}} - t_{\max}. \tag{3.11}$$

We here express the diverging time-reversed wave in terms of the original wave field. Notice, if $t_{\max} = 0$, the diverging wave would be expressed by $Q_p(t - T_{\mathrm{fwd}})$, a simple translation in time.

In order to obtain a more concise relationship for the time-reversal field Q_p^{TR}, we assume that the source time function is a narrow peak in time compared to T_{fwd}, and we limit the validity of the following equation to points that are far enough away from the source. Here, far enough means that the converging and diverging waves can be resolved separately in time (cf. fig. 3.2d). With these assumptions, we can artificially increase τ, such that we finally obtain

$$Q_p^{\mathrm{TR}}(\mathbf{x}, t) = \begin{cases} Q_p(\mathbf{x}, T_{\mathrm{fwd}} - t) & \text{if } t \le T_{\mathrm{fwd}} - t_{\max}, \\ Q_p(\mathbf{x}, t - (T_{\mathrm{fwd}} - 2 \cdot t_{\max})) & \text{if } t \ge T_{\mathrm{fwd}} - t_{\max}. \end{cases} \tag{3.12}$$

This is an important observation. It implies that the time-reversed field shows two wave-fronts. At first, the time-reversed wave $\mathbf{U}(\mathbf{x}, T_{\mathrm{fwd}} - t)$ converges from the surface towards the

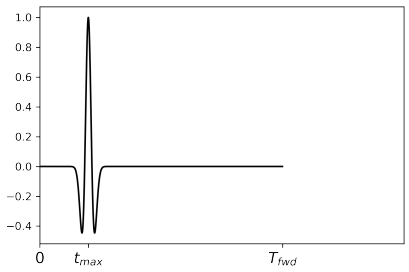

(a) Time evolution at the source point in the forward direction.

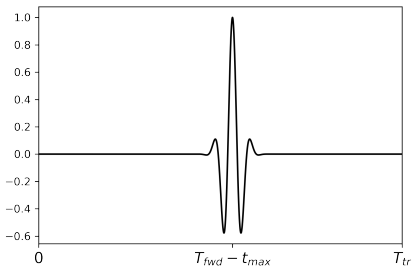

(b) Time evolution at the source point in the time-reversed direction.

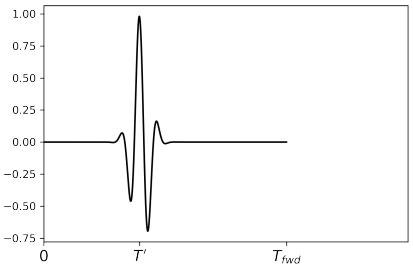

(c) Time evolution in the forward direction at a receiver point located somewhere in the volume.

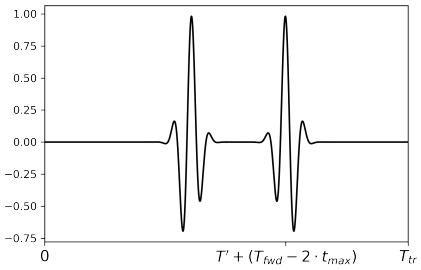

(d) Time evolution in the time-reversed direction at the same receiver location as in fig. 3.2c.

Figure 3.2: Time evolution of Q_p of both forward (*left*) and time-reversed (*right*) direction at two different receiver points. Naturally, in the time-reversed field at the source a distinction between the converging and diverging wave is not possible. However, further away from the source the converging and diverging wave field can be resolved separately.

point source inside the volume. After converging, the wave will then diverge and propagate through the medium again, as described by $\mathbf{U}(\mathbf{x}, t-(T_{\text{fwd}}-2\cdot t_{\max}))$. Since we in principle can record the wave field at any point inside the volume in the forward direction, this equation enables us to compare the results from the time-reversal to the forward simulation.

The entries of Q_p are limited to the independent quantities of the stress tensor (cf. eq. 3.3). The equations above, relating Q_p^{TR} to Q_p are meant to describe the entries of σ_{ij}. Evidently, we can also compare the velocities V_i from both the initial and time-reversed wave. By doing so, the propagation direction of the wave has to be considered, yielding an additional factor of -1 in the description of the convergent wave in eq. 3.12. Thus taking into account that the converging wave is not only time-reversed in comparison to the original propagating wave, but that the propagation direction is also reversed.

To summarize, we have modified the theory presented by Cassereau and Fink ([CF92a]) to accommodate a source of the form $\mathbf{S}(\mathbf{x}, t) = s(t)\delta_D(\mathbf{x}-\mathbf{x}_0)$. We have not presented a rigorous derivation using Green's functions, but instead presented an argument that agrees with the experimental results obtained in Chapter 5. The core part of the theory, however, remains unchanged. The converging part of eq. 3.12 is identical to the one presented in [FF17]; that is, we expect the time-reversed wave to be a mirror of the original forward propagating wave. Analogously to Fink *et al.* we find a diverging wave in our experiments, i.e. the second part of eq. 3.12. It differs from the description obtained by Fink *et al.*, which can be attributed to the use of a different type of source function.

We have thus successfully established the theory of the time-reversal in a way that allows us to compare the forward simulation with the time-reversal. Thereby, we will be able to make assessments on the validity of the time-reversal and on the accuracy of time-reversed waves in SeisSol. The exact setup of the experiments is detailed in Chapter 4. However, prior thereof, the implementation in SeiSol shall be presented.

3.2 Implementation

In this section, the additions made to SeisSol that allow the simulation of time-reversed waves are presented.[1] The implementation is kept as general as possible to allow future experiments to reuse the current code.

As is evident from the description above, SeisSol remains unchanged in the forward direction. The goal of the recording step is to record the outgoing wave on the surface $\mathcal{S}$. In order to achieve this, recording points are specified on $\mathcal{S}$. While simulating, SeisSol writes all entries from Q_p into so-called receiver files. A receiver file contains the time evolution of all values Q_p at a given point. The sample rate in time can be adjusted with the parameters of the simulation. Naturally, the number of recording points can be varied. Nonetheless, $\mathcal{S}$ will only be sampled discretely by the recording points, in both space and time. This is the first step in the time-reversal process.

The interesting part of the implementation is the reconstruction step. During the initialization phase of SeisSol the receiver files obtained from the forward simulation are read. That is, the position of each receiver file and the relevant entries of Q_p are stored. Relevant here means the first six entries of Q_p, i.e. the entries of the stress tensor. As mentioned in the previous section, one can alternatively choose to set the velocities instead of the σ_{ij} at $\mathcal{S}$. Therefore, when referring to Q_p in the following we address the first six components mentioned in eq. 3.3. During the time-reversal simulation, the values at the physical boundary need to be set. That is, we need to properly specify the sources on $\mathcal{S}$. This is a two-step

[1] The code it its entirety can be found here: https://github.com/pwendland/SeisSol/tree/time-reversal-master-thesis

process. At first, an interpolation in space and time is performed to obtain appropriate values for Q_p at any point on $\mathcal{S}$ for any time t with $0 \leq t \leq T$. Subsequently, the actual time-reversal is implemented and the appropriate boundary conditions set.

3.2.1 Interpolation

The receiver files are both discrete in time and space. A high sampling rate in time is easily achievable, which is why a linear interpolation in time is appropriate. That is, for each entry Q_p of $\mathbf{Q}$ we calculate the linear interpolation at time τ

$$Q_p^{\text{LinInterpol}} = Q_p(t_0) + \frac{(\tau - t_0) \cdot (Q_p(t_1) - Q_p(t_0))}{t_1 - t_0}, \tag{3.13}$$

where $t_0 < \tau < t_1$. That is, we find recorded timestamps t_0 and t_1 as close to τ as possible where the values of $\mathbf{Q}$ are known. This interpolation is performed as a first step for all elements Q_p.

In space, the inverse distance weighting (IDW) interpolation technique is used. As mentioned earlier, each receiver captures the incoming wave locally. With IDW the importance of a given data point decreases with its distance to the unknown point. The number of known points N taken into account in the calculations is variable. We choose $N = 4$, as the receivers are placed at regular intervals, which allows for a sufficiently accurate local approximation.

Here, the basic form of Shephard's method is used; given a set of known points r_i, $i \in [1, N]$, in Cartesian coordinates, with the recorded value at each point Q_p^i, we can interpolate the value Q_u at an unknown point x_u by computing:

$$Q_p^u = \begin{cases} \frac{\sum_{i=1}^N w_i(x_u, x_i) Q_p^i}{\sum_{i=1}^N w_i(x_u, x_i)} & \text{if } d(x_u, x_i) \neq 0, \forall i, \\ Q_p^i & \text{if } \exists i : d(x_u, x_i) = 0, \end{cases} \tag{3.14}$$

with

$$w_i(x_u, x_i) = \frac{1}{d(x_u, x_i)^k}, \tag{3.15}$$

where $k \in \mathbb{R}^+$ is the so-called power-parameter. We choose $k = 2$, such that points that are further away contribute quadratically less to the result, a similar dependence as Newtonian gravity ($\propto \frac{1}{r^2}$).

We chose IDW over e.g. nearest neighbor interpolation, since it provides a smoother approximation of the actual wave field.

3.2.2 Setting Sources at the Surface

After the initialization steps, all entries of Q_p are stored in vectors with associated position and timestamp for each value. Since the receiver files were recorded during the entire forward simulation, we obtain the end time T_{fwd} of the initial simulation simply by extracting the last recorded timestamp. In a loop over the quadrature points on the surface $\mathcal{S}$, we set the sources which radiate the time-reversed wave. At first, we obtain the entries of Q_p after the interpolation at a node position in a time-reversed manner. The time-reversal of the receiver files is achieved by simply reversing the time dimension

$$t \to T_{\text{fwd}} - t, \tag{3.16}$$

with the current simulation time t. This approach results in

$$Q_p^{\mathrm{tr}}(\mathbf{x}, t) = Q_p(\mathbf{x}, T_{\mathrm{fwd}} - t)H(T - t). \tag{3.17}$$

Note that once the simulation time t exceeds the recording time T_{fwd} from the forward simulation, the receiver files cannot return a sensible value, hence it is set to zero by multiplying with

$$H(t) = \begin{cases} 1 & \text{if } t \geq 0, \\ 0 & \text{otherwise.} \end{cases} \tag{3.18}$$

Alternatively, this can be achieved implicitly by defining $Q_p(t) = 0 \,\forall\, t < 0$.

Before actually setting the time-reversed field, we need to apply the transformation from the global Cartesian system to the local normal system, as described by the transformation matrix in eq. 2.33. The receiver files record Q_p in the global Cartesian frame, while the boundary conditions are evaluated in the normal frame. Transforming eq. 2.32 yields

$$Q_p^n = T_{pq}^{-1} Q_p, \tag{3.19}$$

where we use the inverse of the transformation matrix T_{pq}. It should be noted that we are only setting the stresses at the surface, thus only require to invert a 6×6 submatrix of T_{pq}. Both T_{pq} and its inverse are precomputed as they are also needed for flux computations. The values Q_p^n are now set on $\mathcal{S}$ and act as sources in the time-reversal.

In this section, we provided a general implementation of the time-reversal in SeisSol independent of the volume and the material parameters used. The result is dependent on different hyperparameters that need to be set before running a simulation.

The end time T_{fwd} can be determined by considering the extent of the volume and the source characteristics. In order to create a satisfactory time-reversal, the receivers on $\mathcal{S}$ ideally need to record the entire outgoing wave. Choosing a smaller T_{fwd} results in a less accurate time-reversal, while larger values require unnecessary computation time.

The far harder choice is to determine the number of receivers needed on $\mathcal{S}$. As proposed by Fink *et al.* in [FP01], the receivers should not be placed at a distance greater than $\psi_{\min}/2$ apart, where $\psi_{\min}$ is the smallest wavelength of the propagating wave field. Depending on the number of receivers, the parameters for the interpolation can also be adjusted. Increasing the power parameter k will ultimately result in the mosaic pattern of the nearest neighbor interpolation. But in our case $k = 2$ remains constant.

Chapter 4

Method

We shall now move from the general considerations in previous chapters to the details of how the analysis in Chapter 5 was conducted. Firstly, we will define the mesh and its material parameters. Thereafter, the source function is examined more closely. Lastly, we will present the misfit criteria Kristekova *et al.* use for the quantitative comparison of seismograms in [Kri+06] and any general pre-processing steps needed before moving on to the analysis.

Note that the content presented in sections 4.1 and 4.2 is not applicable in the last test case presented in sec. 5.3. The important parameters for the WP2-LOH1 test case are introduced at the beginning of said section.

4.1 Mesh and Material

In order to successfully start a simulation in SeisSol, several initial properties have to be specified. The volume in which the simulation is run is determined by the mesh geometry. The volume of interest is a $(10x10x10)$m cube with origin at $(0,0,-5)$, i.e. x- and y-ranges are $[-5,5]$ and the z-range is $[-10,0]$. Using the transfinite algorithm in gmsh[1] we create a structured, regular tetrahedral mesh with approximately $100k$ elements (see fig. 4.1). We intentionally choose a regular grid over a locally refined mesh. Consider the regions of interest in our approach. Obviously, the source region, i.e. the origin of the cube, is a region of interest. Furthermore, the entire surface of the cube is important, since the data for the time-reversal is collected there. Finally, in order to analyse the differences between forward and time-reversed direction, receivers are placed throughout the volume to record both directions. This implies that any point inside the volume where a receiver is located should also be surrounded by a refined mesh. Since the points of interest are spread out over the entire volume and vary in the different test cases, using a regular mesh is the best choice.

This mesh is used for both the forward and the time-reversed direction, different only in the physical boundaries. As discussed above, in the forward direction we employ absorbing boundary conditions, while in the time-reversal inflow boundary conditions are applied.

The experiments are split into two main parts; providing a proof-of-concept in the simplified acoustic case, i.e. $\mu = 0$, and then further analyzing the capabilities of the time-reversal by moving to an elastic medium. As we are conducting the simulations in a mock environment, simple, and thus unrealistic material parameters are chosen. Changing the material parameters to more realistic values does not add a significant weight to the results and is, therefore, not taken into account in further considerations. Nevertheless, a qualitative study of the benchmark scenario WP2-LOH1 (Wave Propagation 2 - Layer Over Halfspace) is con-

[1] https://gmsh.info/

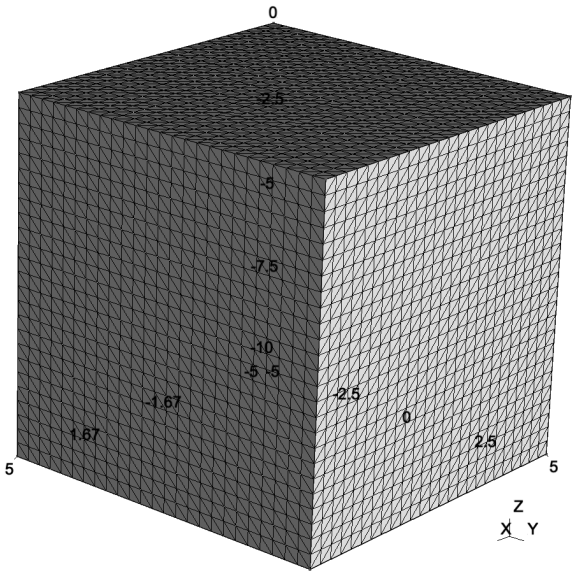

Figure 4.1: Regular structured mesh on the $(10, 10, 10)$ cube with approximately $100k$ elements.

ducted as a final test. Here, realistic parameters inside a volume spanning multiple kilometers are used.

In the elastic case the material parameters are chosen in such a way that both P- and S-waves can be seen separately in the recorded receiver files. In the acoustic case simple considerations on the propagation velocity and the resulting wavelength are sufficient. In order to introduce inhomogeneities into the medium, we will later vary the material parameters slightly.

4.2 Point Source

In the previous chapter assumptions about the source were made, which will be explored further here. The simulations are performed with a point source located at the center of the cube, i.e. $(0, 0, -5)$. Additionally, we require a smooth and differentiable function, that is symmetric in time and with a reasonable width. The Ricker wavelet is often used in seismic analysis ([Wan15]) and is ideal for our purposes. It is obtained by solving the Stokes differential equation and is mathematically equivalent to the second derivative of a Gaussian function. It is thus smooth and differentiable. The amplitude of the Ricker wavelet at time t is given by

$$A(f, t) = (1 - 2\pi^2 f^2 t^2) e^{-\pi^2 f^2 t^2}, \tag{4.1}$$

where f is the peak frequency. This general form is symmetric around $t = 0$. For our purposes this is inadequate, as we require the source to be smooth in the time interval $[0, T_{\text{fwd}}]$. Hence, the entire wavelet is shifted in the direction of positive time by 4 s and the peak frequency is set to $f = 0.75\,\text{Hz}$ (see fig. 4.2). The frequency choice balances the width of the wavelet and the wavelengths of the resulting wave field. The chosen frequency directly influences the wavelengths $\psi_{p/s} = \frac{v_{p/s}}{f}$ for the propagation speeds v_p and v_s, of P- and S-wave respectively, and thus the minimum resolution for the grid of receivers.

The same source function is applied in both the acoustic and the elastic test cases. The Ricker wavelet is sampled with a timestep of $\Delta t = 0.001\,\text{s}$ for a total of 30 s. In our simulated

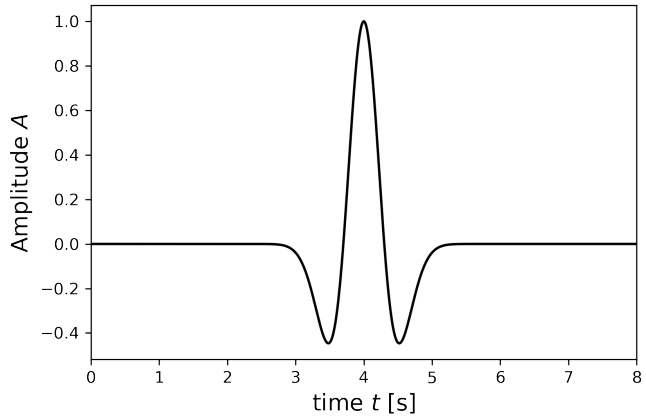

Figure 4.2: The Ricker wavelet as given by $A(f,t) = (1-2\pi^2 f^2 (t-t_{\max})^2 e^{-\pi^2 f^2 (t-t_{\max})^2}$, with $f = 0.75\,\text{Hz}$ and $t_{\max} = 4\,\text{s}$.

environment strike, dip and rake angles are set to 0. The most important difference between the acoustic and the elastic case is the moment tensor of the source. In the acoustic case, an isotropic explosive source is used, thus yielding the moment tensor of the acoustic source

$$M_{ij}^{\text{Acoustic}} = \begin{pmatrix} 1 & 0 & 0 \\ 0 & 1 & 0 \\ 0 & 0 & 1 \end{pmatrix}. \tag{4.2}$$

In the elastic case, we use a moment tensor associated with a vertical strike-slip fault

$$M_{ij}^{\text{Elastic}} = \begin{pmatrix} 0 & 1 & 0 \\ 1 & 0 & 0 \\ 0 & 0 & 0 \end{pmatrix}, \tag{4.3}$$

thereby setting a focus on the xy-plane in the analysis.

4.3 Comparison of Receiver Data

A major part of this thesis is the comparison between the wave fields obtained through the forward and the time-reversed simulation. As elaborated in the previous chapter, the time-reversed direction consists of a converging and a diverging wave, which both depend on the result from the forward direction. In order to assess the quality and correctness of the time-reversal, Q_p and Q_p^{TR} of the two simulations needed to be compared and their difference qualified. Analogously to receivers placed on the surface $\mathcal{S}$, recording points can be defined throughout the volume to record Q_p as a function of time. In Chapter 5, we will elaborate how these points are chosen in a representative fashion. In this section, we shall first discuss the general criteria used to compare two signals, after which we will detail the pre-processing steps needed to actually obtain two matching signals. Hence, for now we define the signal $s(t)$ and the reference signal $s_{\text{ref}}(t)$. Consider the reference signal to hold the time evolution from the forward simulation and $s(t)$ the information from the time-reversal. Note that the space dependency is omitted here, since it is obvious that we consider the signals obtained from one receiver at a specific point in space.

We make use of two different criteria to quantify the difference between the two seismograms. Firstly, the commonly known root-mean-square error is introduced, after which the more specialized time-frequency misfit as discussed by Kristekova *et al.* ([Kri+06]) is presented.

A commonly used misfit criterion is the root mean square (RMS). It is defined as

$$RMS = \sqrt{\frac{\sum_t \mid s(t) - s_{\text{ref}}(t) \mid^2}{\sum_t \mid s_{\text{ref}}(t) \mid^2}}. \tag{4.4}$$

In [Kri+06], Kristekova *et al.* introduce more precise misfit criteria based on the time-frequency representation of the seismograms. Apart from time- and frequency-dependent criteria, single-valued envelope misfit *EM* and phase misfit *PM*, respectively, are introduced. Kristekova *et al.* show that if s only differs from s_{ref} in amplitude, *EM* and *RMS* values are identical. However, if a phase difference is present the *RMS* misfit is significantly larger than *EM*. Hence, in the error analysis we will mostly focus on *EM* and *PM*.

Following the derivation in [Kri+06], we obtain the definitions of *EM* and *PM* respectively. Initially, consider the continuous wavelet transform (CWT) of a signal $s(t)$

$$CWT_{(a,b)}\{s(t)\} = \frac{1}{\sqrt{\mid a \mid}} \int_{-\infty}^{\infty} s(t)\theta^*\left(\frac{t-b}{a}\right) \mathrm{d}t. \tag{4.5}$$

Here, t is the time, a a scaling parameter related to the frequency f by $f = \frac{\omega_0}{2\pi a}$, b a translational time parameter, and θ^* the complex conjugate of the analyzing wavelet. We then define the time-frequency (TF) representation $W(t,f)$ of a signal $s(t)$ as

$$W(t,f) = CWT_{(a,b)}\{s(t)\};\ a = \omega_0/2\pi f\ ,\ b = t. \tag{4.6}$$

Using the TF representation of the reference signal $W_{\text{ref}}(t,f)$, we can now define the local TF envelope difference

$$\Delta E(t,f) = \mid W(t,f) \mid - \mid W_{\text{ref}}(t,f) \mid, \tag{4.7}$$

and the local TF phase difference

$$\Delta P = \text{Arg}\left[\frac{W(t,f)}{W_{\text{ref}}(t,f)}\right]. \tag{4.8}$$

Extending Eqs. 4.7 and 4.8 to a global, single-value misfit yields for the envelope misfit *EM*

$$EM = \sqrt{\frac{\sum_f \sum_t \mid \Delta E(t,f) \mid^2}{\sum_f \sum_t \mid W_{\text{ref}}(t,f) \mid^2}}, \tag{4.9}$$

and analogously for the phase misfit *PM*

$$PM = \sqrt{\frac{\sum_f \sum_t \mid \Delta P(t,f) \mid^2}{\sum_f \sum_t \mid W_{\text{ref}}(t,f) \mid^2}}. \tag{4.10}$$

The global single-valued envelope misfit is a single value that describes how well the amplitudes of the reference and the original signal match. Evidently, if there is no phase difference, *EM* and the *RMS*-error will yield the same result, as both are comparing amplitudes. The important difference arises if the two signals exhibit a phase difference in addition to an amplitude mismatch. Since the *RMS*-error does not take the phases of the signal into account, it

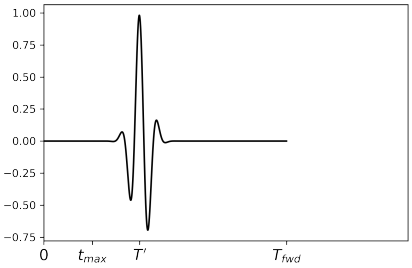

(a) Receiver output from the forward simulation (cf. fig. 3.2c).

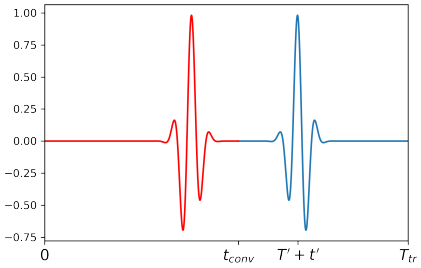

(b) Receiver output from the time-reversal (cf. fig. 4.3d).

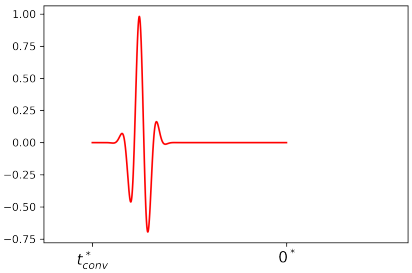

(c) The convergent wave, i.e. the first wave field in fig. 4.3b, is time-reversed in the interval $[0, t_{\text{conv}}]$, which corresponds to times $[t_{\text{max}}, T_{\text{fwd}}]$ in the forward direction.

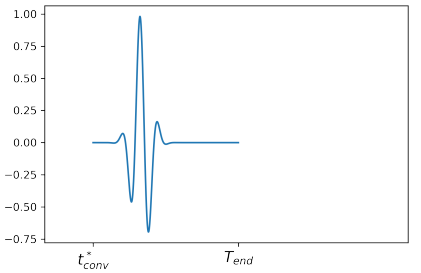

(d) The divergent wave, i.e. the second wave field in fig. 4.3b, is translated in time, such that it coincides with the original forward propagating wave field, i.e. t^*_{conv} is equivalent to t_{max}.

Figure 4.3: The top row shows, similar to fig. 3.2, the forward and the time-reversed receiver output at a fixed position. The bottom row shows the modified converging and diverging wave from the time-reversal.

will significantly over-estimate the error ([Kri+06]). Hence, we introduced the global single-valued phase misfit that together with the envelop misfit will give a more detailed insight when comparing the two signals. Lastly, the pre-processing steps required to actually obtain two signals we expect to be identical in their time evolution need to be detailed.

It is incidental, that the following considerations are made assuming a point source as described in Section 4.2, and only taking points far enough from the origin into account where the converging and diverging wave are reasonably separated. Based on the details given in Section 3.1, we know that the time-reversed signal consists of a converging and a diverging wave. We are thus presented with two different waveforms that can be compared to the forward direction. Again, the process is illustrated with the help of a figure (fig. 4.3). In the upper row the already familiar plots of the forward direction (cf. fig. 4.3a) and the time-reversal (cf. fig. 4.3b) are shown. For the sake of clarity, we introduce t_{conv} as the point in time the wave field converged

$$t_{\text{conv}} = T_{\text{fwd}} - t_{\text{max}}, \tag{4.11}$$

and the translation parameter t'

$$t' = T_{\text{fwd}} - 2 \cdot t_{\text{max}}. \tag{4.12}$$

We now apply the pre-processing steps solely to the time-reversed waveform; the initial wave field stays unmodified. Consider the converging wave first. We know that the converging wave is the time-reversed equivalent of the initial forward propagating wave. By design, the first entry of the time-reversal recording corresponds to the last entry of the forward direction. Thus, we simply identify the first entry of the recording of the time-reversal with the last entry in the initial recording. In fig. 4.3c this point in time is marked by 0^*. Evidently,

this waveform can only be reversed up until t_{conv}, as for all times $t > t_{\text{conv}}$ the receiver in the time-reversal step already records the diverging wave. Again t_{conv} is marked with an asterisk to indicate the equivalent value in the time-reversal, at the new time, such that a comparison with the forward direction is possible. Thus, we compare the original signal $s_{\text{ref}}(t)$ with the mirrored time-reversed signal $s(T_{\text{fwd}} - t)$, but ignore all values for $t < t_{\text{max}}$ after the reversal of the data.

Analogously, we consider the diverging wave. As stated in Section 3.1 the diverging wave is equal to the forward propagating wave, up to a translation in time. The modified wavefield is shown in fig. 4.3d. It is a simple translation in time by t' as defined in eq. 4.12. Again, we only take values at times $t \geq t_{\text{conv}}$ from the time-reversal into account. Additionally, the end time of the comparison t_{end} can be specified as

$$T_{\text{end}} = \min(T_{\text{fwd}} - t_{\text{max}},\ T_{\text{tr}} - t_{\text{conv}}) + t_{\text{max}}, \tag{4.13}$$

which is identical to the interval the convergent wave is compared in, if T_{tr}, the end time of the time-reversed simulation, is chosen sufficiently large. We thus compare $s_{\text{ref}}(t)$ with $s(t + t')$, since the time-reversed field is translated to the left, in the interval $[t_{\text{max}}, T_{\text{end}}]$.

To summarize, we have now established two different misfit criteria: the simple RMS-error and the time-frequency misfit consisting of an envelope and a phase misfit. Subsequently, we defined the modifications to the time-reversed wave field needed in order to enable a comparison. Thereby defining two different ways that the forward and the time-reversed wave field can be compared in qualitatively.

Chapter 5

Analysis of Time-Reversed Waves

This chapter presents and analyses the results obtained from time-reversing seismic waves. The source time function is given by the Ricker wavelet with a frequency of $f = 0.75\,\text{Hz}$ (cf. Chapter 4). The source is a point source located at the origin of the cube, i.e. $(0, 0, -5)$. Unless otherwise stated, the geometry is defined by a $100k$-element mesh extending from $([-5, 5], [-5, 5], [-10, 0])$ in x-, y- and z-direction, respectively. In the recording step, the forward simulation is recorded by receivers on the surface. In the base case, receivers are spaced $\Delta x = 0.5\,\text{m}$ apart, this is justified later on. In the reconstruction step, the time-reversed wave will converge to the location of the source, after which a diverging wave will be observed. Both the time-reversed converging wave, as well as the translated diverging wave should be equal to the original forward propagating wave (cf. sec. 3.1).

This section is split into three parts. As a starting point, the time-reversal is analysed in acoustic media, followed by the analysis in elastic media. Initially, the simplest of cases, a homogeneous medium is examined. Subsequently, more complicated structures are added, by dividing the medium into two parts with distinct material properties, thus creating a material boundary. In addition, a localized inhomogeneity with a high density parameter is introduced, thus creating a predominantly reflecting boundary.

We will conduct both a qualitative and a quantitative analysis. The quantitative analysis focuses on the comparison of receiver files from the forward direction with those obtained in the time-reversal. Thus, we can investigate the entries of Q_p at specific points in the volume to determine if forward and time-reversed signals coincide. In addition to studying the recordings at discrete locations, considering the entire wave field will give insight into the global behavior of the time-reversal. A descriptive analysis of the entire wave field is provided by displaying the 3-dimensional wave propagation graphically.

The homogeneous case is intended to deliver on a sound proof of concept, and showcase the validity of our approach. In the acoustic medium, the contact between two halfspaces is used to examine the grid spacing of receivers on the surface. In addition to the error analysis, a resolution analysis is conducted in the elastic medium, in order to determine the minimum number of receivers needed for a time-reversal. All simulations record Q_p every $\Delta t = 0.002\,\text{s}$.

Finally, the time-reversal method is applied to a benchmark test problem, WP2-LOH1, in order to showcase the time-reversal outside the $(10 \times 10 \times 10)\,\text{m}$ test volume.

5.1 Acoustic Media

The acoustic case is a simplification of propagation in elastic media. The crucial difference is the second Lamé parameter, which in acoustics is zero. From eq. 2.27 it then follows that σ_{ij} only has non-zero diagonal entries. The property that all diagonal elements are identical (cf.

eq. 2.27) is verified in the homogeneous case and later utilized to simplify the analysis.

5.1.1 Homogeneous Volume

We shall start our analysis with the simplest of cases, a homogeneous, isotropic, acoustic medium. The medium is characterized by the following parameters

$$\rho_1 = 1\,,\ \lambda_1 = 2.25\,,\ \mu_1 = 0. \tag{5.1}$$

The propagation velocity $v_{p,1}$ can thus be calculated using eq. 2.25:

$$v_{p,1} = \sqrt{\frac{\lambda_1}{\rho_1}} = 1.5\,\frac{\mathrm{m}}{\mathrm{s}}. \tag{5.2}$$

The wavelength $\psi_{p,1}$ is given in terms of the frequency $f = 0.75\,\mathrm{Hz}$ of the Ricker wavelet (cf. sec. 4.2) and the propagation velocity

$$\psi_{p,1} = \frac{v_{p,1}}{f} = 2.0\,\mathrm{m}. \tag{5.3}$$

A grid of step size $\Delta x = 0.5\,\mathrm{m}$ is defined on the surface of the $(10 \times 10 \times 10)\,\mathrm{m}$ volume. This is amounts to placing 2402 receivers on $\mathcal{S}$. Additionally, a total of 14 receivers are placed inside the volume. We differentiate between receivers set halfway between the source and the surface, in the different coordinate directions, and others located 1 m away from the surface boundary in each of eight quadrants of the cube. The source time function is a Ricker wavelet, translated to peak at time $t = 4\,\mathrm{s}$, i.e. $t_{\max} = 4\,\mathrm{s}$. The end time of the forward simulation is $T_{\mathrm{fwd}} = 20\,\mathrm{s}$.

If a time-reversal is indeed achieved, it can most simply be verified by examining the wave field output (cf. fig 5.1 [1]). With $T_{\mathrm{fwd}} = 20\,\mathrm{s}$, $t_{\max} = 4\,\mathrm{s}$ and eq. 4.11 it follows that

$$t_{\mathrm{conv}} = 16\,\mathrm{s}. \tag{5.4}$$

At $t = 12\,\mathrm{s}$ the time-reversed wave is starting to propagate from the surface of the volume towards the center (cf. fig. 5.1a). With $v_{p,1} = 1.5\,\frac{\mathrm{m}}{\mathrm{s}}$, the peak of the wave is expected to begin propagating inside the volume with a delay of

$$\frac{\frac{1}{2}\psi_{p,1}}{v_{p,1}} = 0.67\,\mathrm{s}. \tag{5.5}$$

This time needs to be added to the time the wavefront takes to travel from the boundary to the origin along the x-direction, $\frac{v_{p,1}}{5\,\mathrm{m}} = 3.33\,\mathrm{s}$, as the convergence calculations are made considering the peak of the wave field. Further advancing in time, the wave field can be seen to start converging to the center (cf. fig. 5.1b), and finally, at $t = 16\,\mathrm{s}$ the wave field is entirely converged at the location of the original source (cf. fig. 5.1c). This agrees with the propagation time calculated previously, since $12 + 3.33 + 0.47 = 16\,\mathrm{s}$. Directly afterwards, an outward propagating (diverging) wave is observed (cf. fig. 5.1d).

To justify the limitation of only considering σ_{xx}, instead of all entries of the stress tensor, and to verify that the time-reversed wave field indeed observes the acoustic properties mentioned at the end of Section 2.1, we examine the entries of σ_{ij}. A general receiver, i.e. a receiver located in a general position, is considered. As expected, all off-diagonal entries are

[1] The 2D wave field output of the entire time-reversal simulation is published as a video: https://youtu.be/w7k3fZkQ5rY.

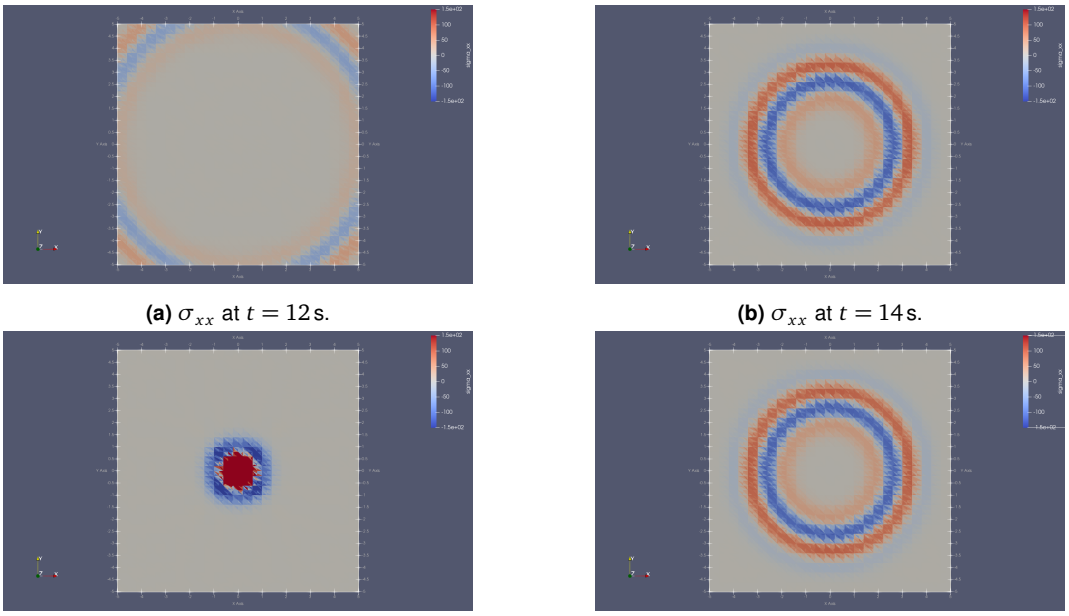

(a) σ_{xx} at $t = 12\,\mathrm{s}$. **(b)** σ_{xx} at $t = 14\,\mathrm{s}$.

(c) σ_{xx} at $t = 16\,\mathrm{s}$. **(d)** σ_{xx} at $t = 18\,\mathrm{s}$.

Figure 5.1: Snapshots of σ_{xx} of the time-reversed wave field in the homogeneous acoustic case at different times, in the interval $[-150, 150]$, where blue and red correspond the most negative and positive values, respectively. The video displaying the entire simulation is available here[1].

close to zero and the diagonal entries are identical (cf. fig. 5.2). To provide a proof beyond the visual, the RMS error (see eq. 4.4) is calculated. Comparing each pair yields an error of less than $4 \cdot 10^{-15}$, thus confirming the acoustic nature of the wave field. This allows us to limit our analysis to the σ_{xx} entry of the stress tensor without loss of generality.

We shall furthermore limit the following analysis to points with interesting differences. For the sake of completeness, comprehensive results are listed in App. A.1. In order to gain an overview over the data, the time evolution of σ_{xx} of both the forward and the time-reversed wave is plotted over T_{fwd} and T_{tr}, respectively (fig. 5.3). As expected, one wavefront is observed in the forward direction. This wavefront arrives later at receivers further away from the source. The time evolution of the time-reversed wave also agrees with the behavior seen in the visualization. Two wavefronts are recorded, that are spaced further apart, the further away the receiver is from the source. Focusing on the time evolution of the receiver located at $(-4.0, -4.0, -9.0)$, the first wavefront can be identified as the time-reversed signal from the intial forward propagating wave, while the second wavefront is equal to the original wave, except for a translation in time (cf. last row in fig. 5.3).

These two wavefronts can be compared to the original wave. To stay concise, the resulting plots while calculating the envelope and phase misfits of only one receiver, at $(2.5, 2.5, -2.5)$ are shown in fig. 5.4. According to the criteria defined by Kristekova *et al.* in [KKM09], an envelope misfit of less than ± 0.16 and a phase misfit of less than ± 0.15 can be classified as an excellent fit. The RMS error, including EM and PM are calculated for each receiver (cf. tab. 5.1, and App. A.1 for the misfits of all 14 receivers). None of the calculated values are above these thresholds. We observe that the phase misfit is consistently smaller than the envelope misfit, which is largest around the peaks of the wave (cf. fig. 5.4). We refrain from analysing the error differences between the receivers here, as this will be discussed in more detail in the following section. This is justified by treating the homogeneous acoustic case as a proof of concept. Thereby, we have established that the time-reversal method indeed reverses the original wave within an acceptable margin of error. This section thus provides a

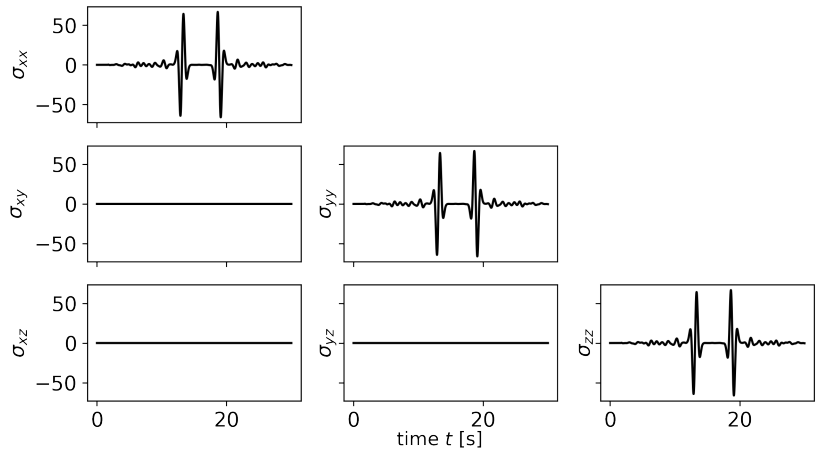

Figure 5.2: The six independent entries of σ_{ij} as recorded by the receiver located at $(2.5, 2.5, -2.5)$, over the entire simulation time of the time-reversal in the homogeneous acoustic case.

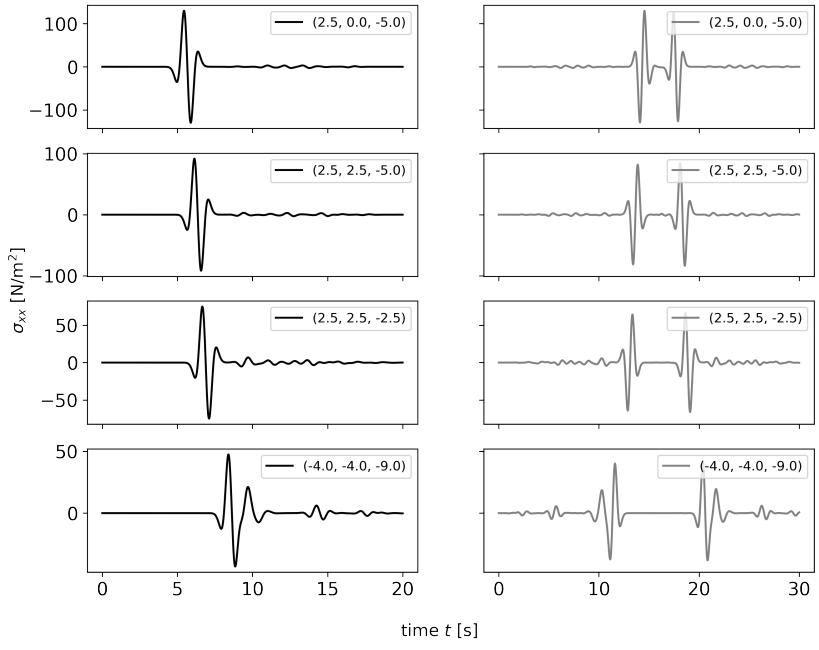

Figure 5.3: σ_{xx} is shown as a function of time for both the forward direction (*left*) and the time-reversed direction (*right*) for four different receiver locations. Note the time axis is scaled differently on the left and the right side.

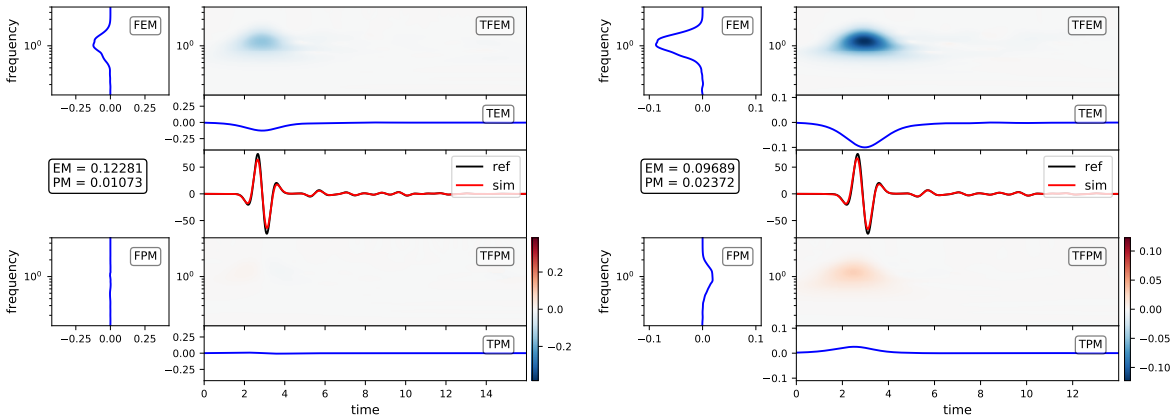

(a) Time-frequency misfit of the converging wave field

(b) Time-frequency misfit of the diverging wave field

Figure 5.4: Time-frequency misfits of both the converging and diverging wave field. In order to obtain comparable wave fields, the time-reversed signal was modified according to the theory described in Section 4.3. The receiver is located at $(2.5, 2.5, -2.5)$, i.e. on the space diagonal.

Table 5.1: Homogeneous medium (acoustic): RMS, EM, and PM values obtained by comparing the σ_{xx} entry from both the convergent and the divergent wave with the forward simulation. For each receiver, both the error calculations for the converging and the diverging wave are presented in the first and second row, respectively.

Receiver Position	RMS	EM	PM
$(-2.5, 0.0, -5.0)$	0.08331	0.02110	0.01785
	0.08855	0.04896	0.01998
$(2.5, 2.5, -5.0)$	0.12207	0.09395	0.00807
	0.10377	0.07081	0.01539
$(2.5, 2.5, -2.5)$	0.15008	0.12281	0.01073
	0.12588	0.09689	0.02372
$(-4.0, -4.0, -9.0)$	0.13796	0.11422	0.01120
	0.10620	0.08887	0.01940

basic understanding of the data and the methodology applied to determine the goodness-of-fit.

5.1.2 Contact of two Halfspaces

The cube is separated into two halfspaces with distinct materials properties. Since the source is located at the origin, we offset the medium boundary slightly. That is, for all $x < 0.25$ the medium has the same properties as in the homogeneous test case, whereas for all $x \geq 0.25$ the following new material parameters are set

$$\rho_2 = 0.25\,,\ \lambda_2 = 2.25\,,\ \mu_2 = 0. \tag{5.6}$$

Changing the material parameters affects both the propagation velocity and the wavelength of the wave. Thus, in the modified medium the wave has a wavelength of

$$\psi_{p,2} = \frac{v_{p,2}}{f} = 4.0\,\mathrm{m}, \tag{5.7}$$

and propagates with the velocity

$$v_{p,2} = \sqrt{\frac{\lambda}{\rho}} = 3.0\,\frac{\mathrm{m}}{\mathrm{s}}. \tag{5.8}$$

Observing the 3D wave field in the xy-plane, the medium boundary is clearly visible (cf. fig. 5.5[2]). At time $t = 13\,\mathrm{s}$, the propagating wave is only visible for negative x (cf. fig.5.6a). We know from before that the wave converges at the origin at $t = 16\,\mathrm{s}$. With a velocity of $v_{p,2}$, the wave needs 2.35 s to travel on the diagonal from $(x, y) = (5, 5)$ to the origin. Thus, at $t = 13\,\mathrm{s}$ no perturbation is seen in the medium for positive x. Analogously, the wavefront requires 1.7 s to travel on a straight line from $x = 5$ to $x = 0$ in 1.7 s. In fig. 5.6b the wave field is seen at time $t = 14.3\,\mathrm{s}$, where the wavefront is almost entirely visible in the volume. 1.7 s later, at $t = 16\,\mathrm{s}$ the converged wave field can be observed (cf. fig. 5.6c). Analogously to the previous case, for times $t > 16\,\mathrm{s}$ the diverging wave is seen (cf. fig. 5.6d).

Throughout the medium, receivers are placed at meaningful locations. This includes points located on the medium boundary at $x = 0.25$, and receivers both closer to the source and further away.[3] As previously explained, in the error calculations both the converging and the diverging wave of the time evolution of σ_{xx} are examined (tab. 5.2). It is apparent that both EM and PM values are below the threshold of ±0.16. A noticeable observation is the fact that receivers located in the second medium, i.e. $x > 0.25$, show considerably better fits than receivers in medium 1. As can be seen in App. A.2 this is not only true for a selected number of receivers, but instead is a consistent result throughout all receivers. Resulting from the distinct material parameters, is a change in wavelength and propagation velocity. Fink *et al.* use an array pitch smaller than $\psi_p/2$ in [FP01]. With receivers spaced $\Delta x = 0.5\,\mathrm{m}$ apart and wavelengths of $\psi_{p,1} = 2.0\,\mathrm{m}$ and $\psi_{p,2} = 4.0\,\mathrm{m}$, this criterion is fulfilled. In order to find an explanation for the difference in the resulting errors, further analyses are conducted.

Before considering the wavelengths in more detail, the mesh is examined to ensure the reason for an increased error is not due to a limited resolution in the mesh. Simulating the homogeneous acoustic case with a $500k$-element mesh, instead of the previously used mesh with $100k$ elements, yields no significant improvement in the misfits (cf. tab. A.2 in App. A.1). Thus, confirming that the characteristics of the wave itself seem to be crucial. As a first investigation step, an additional time-reversal experiment with a modified grid of receivers, spaced $\Delta x = 1.0\,\mathrm{m}$ apart, was conducted. This amounts to 602 receivers spaced over all six faces on a regular grid. It is instructive to examine the 2D visualization of the wave field

[2] The 3D wave field output of the entire time-reversal simulation is published as a video: https://youtu.be/uq6Eetvf4EE.

[3] Error calculations for all receivers can be reviewed in App. A.2

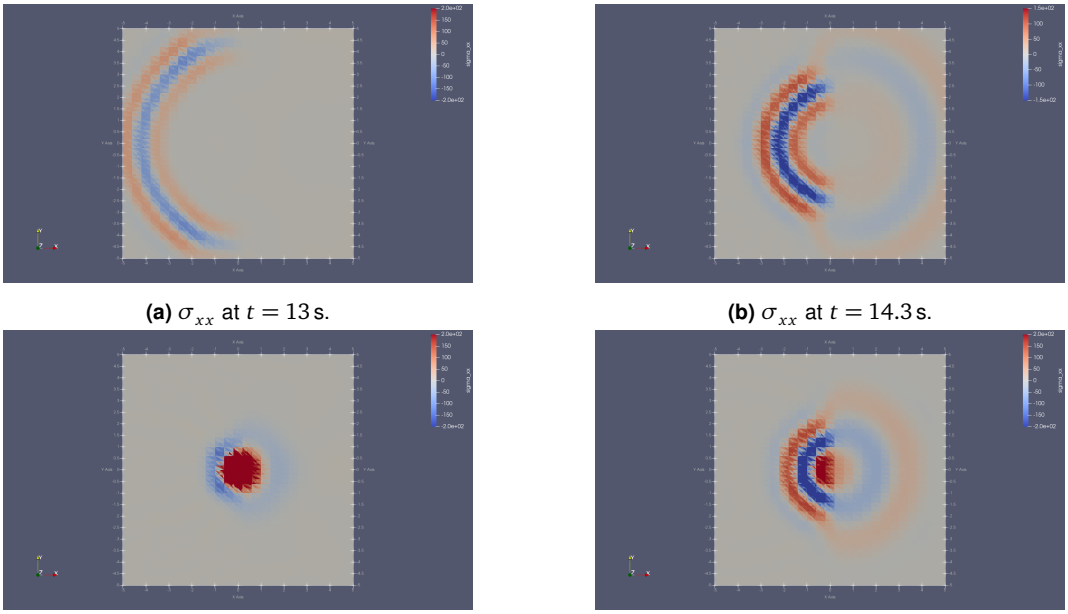

(a) σ_{xx} at $t = 13\,\text{s}$. **(b)** σ_{xx} at $t = 14.3\,\text{s}$.

(c) σ_{xx} at $t = 16\,\text{s}$. **(d)** σ_{xx} at $t = 17\,\text{s}$.

Figure 5.5: Snapshots of σ_{xx} of the time-reversed wave field at different times, in the interval $[-200, 200]$, where blue and red correspond the most negative and positive values, respectively. The video displaying the entire simulation is available here[2].

Table 5.2: Contact between two halfspaces (acoustic): RMS, EM, and PM values obtained by comparing the σ_{xx} entry from both the convergent and the divergent wave with the forward simulation. For each receiver, both the error calculations for the converging and the diverging wave are presented in the first and second row, respectively.

Receiver Position	RMS	EM	PM
$(0.25, -2.5, -7.5)$	0.13443	0.09686	0.01577
	0.10462	0.07874	0.01281
$(-2.5, 0, -5.0)$	0.08924	0.03301	0.01544
	0.12246	0.04274	0.03279
$(2.5, 0, -2.5)$	0.09383	0.03662	0.00827
	0.07620	0.04914	0.01819
$(-2.5, 2.5, -7.5)$	0.16287	0.13699	0.01216
	0.14695	0.11748	0.02346
$(2.5, 2.5, -7.5)$	0.04501	0.02033	0.00718
	0.07015	0.05748	0.00507
$(-4.0, 4.0, -1.0)$	0.14794	0.12472	0.01448
	0.12094	0.10085	0.02002
$(4.0, 4.0, -1.0)$	0.05918	0.04588	0.00600
	0.05091	0.03803	0.00378

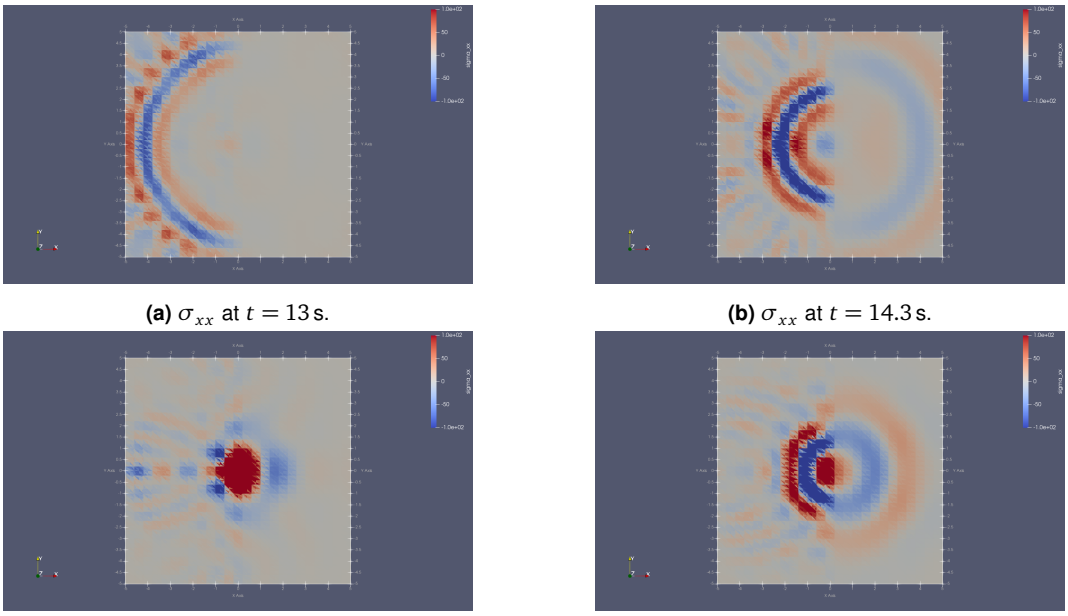

(a) σ_{xx} at $t = 13\,\mathrm{s}$.

(b) σ_{xx} at $t = 14.3\,\mathrm{s}$.

(c) σ_{xx} at $t = 16\,\mathrm{s}$.

(d) σ_{xx} at $t = 17\,\mathrm{s}$.

Figure 5.6: Snapshots of σ_{xx} of the time-reversed wave field at different times, in the interval $[-200, 200]$, where blue and red correspond the most negative and positive values, respectively. Similar to fig. 5.5 with receivers spaced $\Delta x = 1.0\,\mathrm{m}$ apart.

first (fig. 5.6). It is immediately obvious that the wave field propagating in medium 1, with $\psi_{p,1} = 1.0\,\mathrm{m}$ exhibits spurious oscillations. Comparing fig. 5.5 and fig. 5.6, we conclude that receivers spaced $\psi_{p,1}/2 = 1.0\,\mathrm{m}$ apart do not provide a resolution that is accurate enough to assure small misfits. The calculated errors for the same receivers as above are listed in tab. 5.3. The envelope misfit for receivers located in negative x-direction have increased as much as from 0.14, in the simulation with $\Delta x = 0.5$, to 0.48. Thus significantly exceeding the threshold defined previously. Furthermore, even for receivers in positive x-direction large differences can be observed between the errors obtained from the converging and diverging wave. This can be explained by spurious oscillations that are clearly visible in the time evolution of the time-reversed field (cf. fig. A.1 in App. A.2).

Even though the errors have increased significantly, the time-reversal is still clearly visible in the 2D wave field visualization. This poses the question of the minimum number of receivers needed to still create a time-reversed field that converges at the original source. Section 5.2.3 examines this more closely for the elastic case.

Before dismissing the $\psi_P/2$ criterion for the minimal receiver spacing, the manner in which the wavelengths are obtained is investigated. In previous calculations the wavelength was calculated using the peak frequency of the Ricker wavelet (cf. sec. 4.2). The Ricker wavelet, however, unlike basic trigonometric functions, contains multiple frequencies. Its Fourier transform, given by

$$F(f) = \frac{2}{\sqrt{\pi}} \frac{f^2}{f_p^3} e^{-\frac{f^2}{f_p^2}}, \tag{5.9}$$

where f_p is the peak frequency, is plotted in fig. 5.7 for both $f_p = 0.75\,\mathrm{Hz}$ and $f_p = 0.3\,\mathrm{Hz}$ (cf. fig 5.7a and fig. 5.7b, respectively). Using a lower frequency creates a sharper peak, thus resulting in a narrower frequency spectrum.
In order to obtain comparable results, both forward and time-reversal directions are simulated again with the modified frequency of the source function, and different material pa-

Table 5.3: Contact between two halfspaces (acoustic): 602 receivers, creating a grid of $\Delta x = 1.0\,\mathrm{m}$): RMS, EM, and PM values obtained by comparing the σ_{xx} entry from both the convergent and the divergent wave with the forward simulation. For each receiver, both the error calculations for the converging and the diverging wave are presented in the first and second row, respectively.

Receiver Position	RMS	EM	PM
$(0.25, -2.5, -7.5)$	0.4966	0.33540	0.08963
	0.4212	0.28952	0.08138
$(-2.5, 0, -5.0)$	0.6658	0.33944	0.08599
	0.7038	0.17969	0.15756
$(2.5, 0, -5.0)$	0.4195	0.14356	0.04757
	0.3766	0.15901	0.07436
$(-2.5, 2.5, -7.5)$	0.6348	0.47934	0.08517
	0.5566	0.41472	0.09734
$(2.5, 2.5, -7.5)$	0.1515	0.06734	0.02495
	0.2978	0.20814	0.05061
$(-4.0, 4.0, -1.0)$	0.6404	0.36139	0.09512
	0.4357	0.34879	0.07042
$(4.0, 4.0, -1.0)$	0.2284	0.17225	0.02015
	0.2993	0.15161	0.04506

rameters, as to yield identical wavelengths. Assuming a frequency of $f_p = 0.3\,\mathrm{Hz}$, and the wavelengths $\psi_{p,1} = 2.0\,\mathrm{m}$, $\psi_{p,2} = 4.0\,\mathrm{m}$ as given, the medium parameters are easily calculated. The new propagation velocities $v = \psi \cdot f$

$$\begin{aligned} \bar{v}_{p,1} &= \psi_{p,1} \cdot f_p = 0.6 \frac{\mathrm{m}}{\mathrm{s}}, \\ \bar{v}_{p,2} &= \psi_{p,2} \cdot f_p = 1.2 \frac{\mathrm{m}}{\mathrm{s}}, \end{aligned} \tag{5.10}$$

yield

$$\begin{aligned} \bar{\rho}_1 &= 1.0\,,\ \bar{\lambda}_1 = 0.36\,,\ \bar{\mu}_1 = 0, \\ \bar{\rho}_2 &= 1.0\,,\ \bar{\lambda}_2 = 1.44\,,\ \bar{\mu}_2 = 0. \end{aligned} \tag{5.11}$$

The results from the error calculations for the same receivers as above are listed in tab. 5.4. Comparing the simulations with different peak frequencies of the Ricker wavelet, but identical wavelength, only minor differences are visible. The error values in tab. 5.2 and tab. 5.4 do not show a significant difference. This implies that changing the frequency of the Ricker wavelet, which changes the frequency spectrum of the source function, does not improve the accuracy significantly. Thus leading to the re-evaluation of the optimal receiver spacing.

Since a narrower frequency spectrum did not have any significant implications on the resulting errors, we return to the original source function with the frequency $f = 0.75\,\mathrm{Hz}$. Obviously, there are two ways a new bound on the receiver spacing can be found. Either one varies the receiver spacing, or the wavelength of the propagating waves. When receivers are spaced $\Delta x = 0.5\,\mathrm{m}$ apart, 2402 receivers are necessary on the $(10 \times 10 \times 10)\,\mathrm{m}$ cube. Further decreasing this spacing quickly becomes infeasible. Hence, in the following, the wavelengths are varied. Fixing the desired wavelength to $\tilde{\psi}_{p,1} = 6.0\,\mathrm{m}$ and $\tilde{\psi}_{p,2} = 4.0\,\mathrm{m}$ we obtain the propagation velocities $\tilde{v}_{p,1} = 4.5\,\mathrm{ms}^{-1}$, $\tilde{v}_{p,2} = 3.0\,\mathrm{ms}^{-1}$, and the new material parameters for

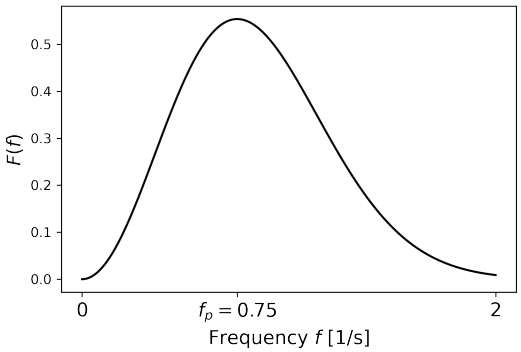

(a) Frequency spectrum of the Ricker wavelet with a peak frequency of $f_p = 0.75\,\text{Hz}$.

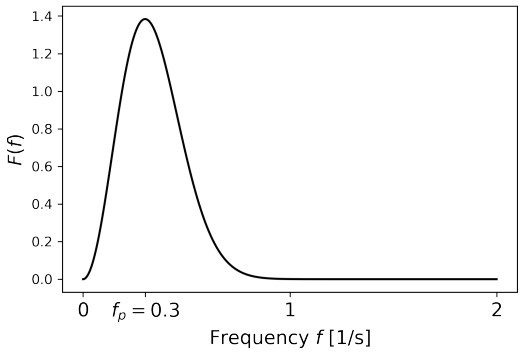

(b) Frequency spectrum of the Ricker wavelet with a peak frequency of $f_p = 0.3\,\text{Hz}$.

Figure 5.7: Fourier transform of the Ricker wavelet for two different peak frequencies.

Table 5.4: Contact between two halfspaces (acoustic): Modified medium parameters, accommodating a Ricker wavelet with $f = 0.3\,\text{Hz}$. RMS, EM, and PM values obtained by comparing the σ_{xx} entry from both the convergent and the divergent wave with the forward simulation. For each receiver, both the error calculations for the converging and the diverging wave are presented in the first and second row, respectively.

Receiver Position	RMS	EM	PM
$(0.25, -2.5, -7.5)$	0.22669	0.08483	0.03639
	0.09158	0.05490	0.00748
$(-2.5, 0, -5.0)$	0.14099	0.03447	0.01563
	0.10845	0.02784	0.01628
$(2.5, 0, -5.0)$	0.08566	0.03927	0.01075
	0.05798	0.04428	0.01643
$(-2.5, 2.5, -7.5)$	0.19767	0.12582	0.01399
	0.13686	0.10291	0.02046
$(2.5, 2.5, -7.5)$	0.07105	0.03397	0.00725
	0.05763	0.04665	0.00371
$(-4.0, 4.0, -1.0)$	0.16680	0.11734	0.01344
	0.11049	0.08847	0.01700
$(4.0, 4.0, -1.0)$	0.06108	0.04711	0.00409
	0.04129	0.03091	0.00280

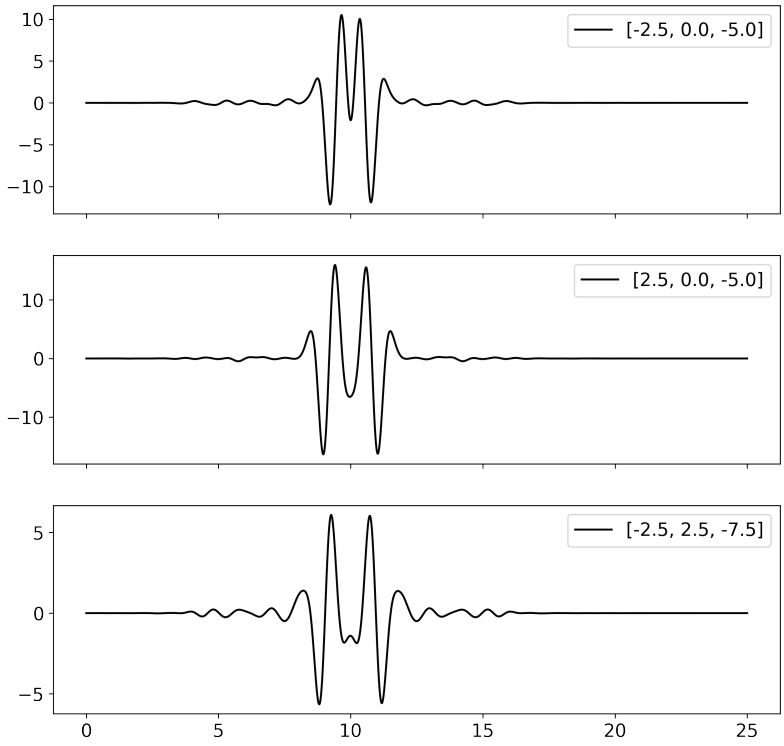

Figure 5.8: Time evolution of the time-reversal of σ_{xx} at three distinct locations. The better the converging and diverging wave can be resolved separately, the lower the calculated errors in tab. 5.5 become. Especially for the receiver located at $(-2.5, 0, -5.0)$ the two waves are hardly distinguishable, thus resulting in a higher envelope misfit.

the two media

$$\begin{aligned} \tilde{\rho}_1 = 1.0\,,\ \tilde{\lambda}_1 = 20.25\,,\ \tilde{\mu}_1 = 0, \\ \tilde{\rho}_2 = 1.0\,,\ \tilde{\lambda}_2 = 9.0\,,\ \tilde{\mu}_2 = 0. \end{aligned} \tag{5.12}$$

The results obtained through this simulation are summarized in tab. 5.5. With the exception of the receiver located at $(-2.5, 0, -5.0)$, all envelope misfits are below 0.06, which is a significant improvement over the initial simulation. In contrast to the homogeneous case, receivers further away from the source do not behave differently than those closer to the source. Examining the time-evolution of the signal for the receiver with the highest error values provides a consistent explanation for this behavior. Fig. 5.8 shows the time-reversed direction for three different receivers. The wave propagates faster in negative x-direction. Hence, receivers have to be located further away from the source, if both the converging and the diverging wave are to be resolved separately. Since that is not the case for the receiver located at $(-2.5, 0, -5.0)$, the errors naturally increase.

In summary, a reasonable accuracy can be achieved when placing receivers on a grid smaller than an eighth of the wavelength, $\psi_p/8$. Increasing the wavelength, or decreasing the receiver spacing beyond that still decreases the error, but introduces new difficulties, such as a faster propagation velocity, and thus a larger region where the converging and the diverging wave cannot be resolved separately.

Table 5.5: Contact of two halfspaces (acoustic): Modified medium parameters, yielding wavelengths of 4.0 m for $x > 0.25$ and 6.0 m for $x < 0.25$. RMS, EM, and PM values obtained from comparing the σ_{xx} entry from both the convergent and the divergent wave with the forward simulation. For each receiver, both the error calculations for the converging and the diverging wave are presented in the first and second row, respectively.

Receiver Position	RMS	EM	PM
$(0.25, -2.5, -7.5)$	0.05662	0.03718	0.01186
	0.05596	0.05490	0.00748
$(-2.5, 0, -5.0)$	0.13197	0.12101	0.06333
	0.14884	0.15018	0.07155
$(2.5, 0, -5.0)$	0.10006	0.05980	0.02796
	0.04863	0.04523	0.01375
$(-2.5, 2.5, -7.5)$	0.03969	0.02347	0.00939
	0.05329	0.02719	0.01246
$(2.5, 2.5, -7.5)$	0.04569	0.03242	0.00784
	0.04260	0.01953	0.01049
$(-4.0, 4.0, -1.0)$	0.04234	0.02540	0.00978
	0.05334	0.03206	0.01238
$(4.0, 4.0, -1.0)$	0.05809	0.04538	0.00959
	0.04914	0.02720	0.01193

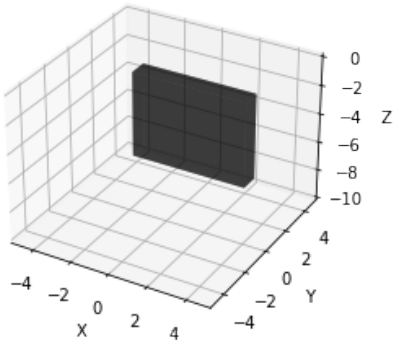

Figure 5.9: An inhomogeneity is introduced in the medium in shape of a box. Its dimensions are $[-3,3],[2,3],[-8,-2]$ in x-, y-, z-direction, respectively. The box has a comparatively high density ($\rho_{\text{box}} = 20$, $\lambda_{\text{box}} = 2.25$), thus creating a predominantly reflective boundary.

5.1.3 Localized Inhomogeneity

Adapted from fig. 3.1, a localized inhomogeneity in shape of a box is introduced. It is located halfway between the source and the boundary in y-direction and stretches from $[-3,3]$ and $[-8,-2]$ in x- and z-direction, respectively (cf. fig. 5.9). Outside the box, the same parameters as previously are used

$$\rho = 0.25\,,\ \lambda = 2.25\,,\ \mu = 0, \tag{5.13}$$

with a resulting wavelength of 4.0 m. The receiver spacing of $\Delta x = 0.5\,\text{m}$ remains unchanged, thus fulfilling the newly found $\psi_p/8$ bound on the distance between receivers. In order to observe the behavior when reflections inside the medium occur, the inside of the box is given a larger density

$$\rho_{\text{box}} = 20.0\,,\ \lambda_{\text{box}} = 2.25\,,\ \mu_{\text{box}} = 0. \tag{5.14}$$

The first indication of a successful time-reversal is again obtained by examining the 3D wave field output of the xy-plane of the σ_{xx} component of the stress tensor (cf. fig. 5.10[4]). At $t = 12\,\text{s}$ the only visible wave field is around the region of the inhomogeneity, providing evidence that waves are propagating out of the inhomogeneity long after the main part of the wave in the forward direction has left the volume. Even with a high density box present in the medium, the converged wave can be observed at time $t = 16\,\text{s}$ (cf. 5.16c). As time advances, the diverging wave can be observed (cf. fig. 5.16d). Contrary to previously studied cases, waves reflected of the boundary of the box are now visible. This distorts the time evolution of some receiver points, making it unreasonable to speak of a time-reversal at those points (cf. fig. 5.11). This is the case for the receiver located at e.g. $(0.0, 2.5, -5.0)$. This observation is confirmed by the envelope misfits, which for both the converging and the diverging wave, with 0.69 and 0.47, are above the threshold of ±0.16 (cf. tab. 5.6). The errors of the converging wave are within acceptable bounds for all other receivers not affected by strong reflections. The errors, when comparing the diverging wave field, are consistently larger (cf. tab. A.4 App. A.3). This can be attributed to the fact that some of the wave gets trapped

[4] The 2D wave field output of the entire time-reversal simulation is published as a video: https://youtu.be/A16TudZXrYs.

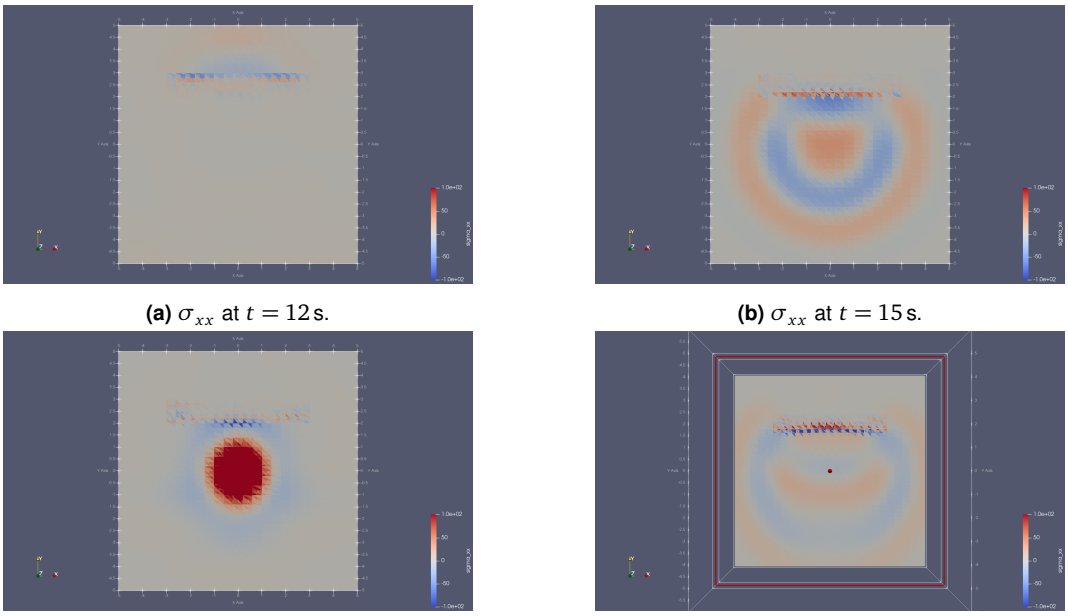

(a) σ_{xx} at $t = 12\,\mathrm{s}$. **(b)** σ_{xx} at $t = 15\,\mathrm{s}$.

(c) σ_{xx} at $t = 16\,\mathrm{s}$. **(d)** σ_{xx} at $t = 17.5\,\mathrm{s}$.

Figure 5.10: Snapshots of σ_{xx} of the time-reversed wavefield at different times, in the interval $[-100, 100]$, where blue and red correspond the most negative and positive values, respectively. The video displaying the entire simulation is available here[4]

inside the box. In the forward direction, the receiver inside the box is still recording an oscillating wave field when T_{fwd} is reached, thus losing information even before the time-reversal is begun. Since the converging wave consistently shows EM and PM values below the thresholds of ± 0.16 and ± 0.15, respectively, we conclude that even with a predominantly reflective boundary a successful time-reversal can be achieved.

Table 5.6: Local inhomogeneity (acoustic): RMS, EM, and PM values obtained from comparing the σ_{xx} entry from both the convergent and the divergent wave with the forward simulation. For each receiver, both the error calculations for the converging and the diverging wave are presented in the first and second row, respectively.

Receiver Position	RMS	EM	PM
$(0.0, 2.5, -5.0)$	0.80980	0.66990	0.39425
	0.72297	0.47226	0.14878
$(0.0, 1.0, -5.0)$	0.72855	0.15473	0.11936
	0.45741	0.26074	0.01702
$(-2.5, 4.0, -3.0)$	0.21537	0.12267	0.04252
	0.11356	0.06428	0.01873
$(-4.0, -4.0, -1.0)$	0.10331	0.05669	0.01517
	0.26060	0.22489	0.05139

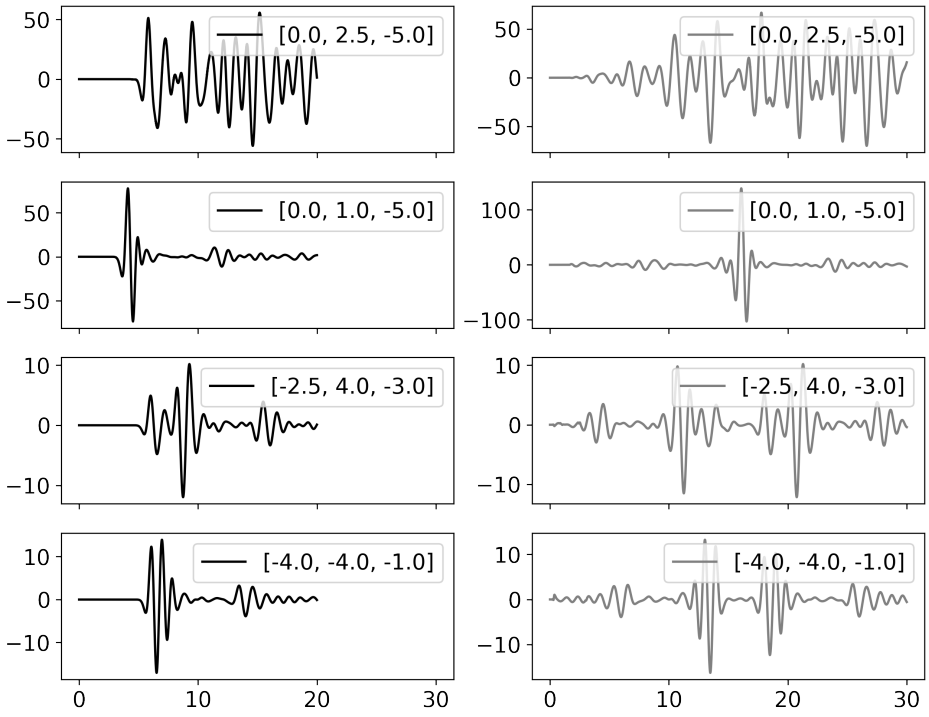

Figure 5.11: From top to bottom the time-evolution of σ_{xx} of receivers located inside the inhomogeneity, between the source and the inhomogeneity, between the inhomogeneity and the boundary, and further away from it, is plotted for both the forward and time-reversed direction.

5.2 Elastic Media

The analysis of acoustic media provided a proof of concept that a time-reversal in SeisSol is achievable with a reasonable accuracy, when spacing receivers less than $\psi_p/8$ apart. In the following, elastic media, i.e. $\mu \neq 0$, will be examined. The main difference between acoustic and elastic media is the presence of both P- (primary) and S- (secondary) waves. In addition to analysing the accuracy of the time-reversal, the minimum number of receivers required in order to achieve a visible time-reversal in the 3D visualization is determined.

5.2.1 Homogeneous Volume

A homogeneous volume serves as the basis for the first analysis. The medium is characterized by

$$\rho = 1.0\,,\ \lambda = 5.0\,,\ \mu = 2.0. \tag{5.15}$$

Following the theory presented in Section 2.1, we obtain the velocities

$$\begin{aligned} v_p &= \sqrt{\frac{\lambda + 2\mu}{\rho}} = 3.0\,\frac{\mathrm{m}}{\mathrm{s}} \\ v_s &= \sqrt{\frac{\mu}{\rho}} = 1.41\,\frac{\mathrm{m}}{\mathrm{s}}. \end{aligned} \tag{5.16}$$

The corresponding wavelengths are calculated with the peak frequency of the source, $f_p = 0.75\,\mathrm{Hz}$

$$\begin{aligned} \psi_p &= 4.0\,\mathrm{m}, \\ \psi_s &= 1.89\,\mathrm{m}. \end{aligned} \tag{5.17}$$

Finally, as discussed in Section 4.2, a double couple source with the moment tensor

$$M_{ij} = \begin{pmatrix} 0 & 1 & 0 \\ 1 & 0 & 0 \\ 0 & 0 & 0 \end{pmatrix}, \tag{5.18}$$

is used. This creates a strike-slip fault, with strike and dip directions along the y- and x-axis, respectively. As in the acoustic case, the P-wave is a longitudinal wave, whereas now, also the S-wave, a shear wave, is observed. Before assessing the error of the time-reversal, the basic properties of the elastic medium are verified. This serves as a confirmation that the following time-reversal is indeed achieved in a medium exhibiting these properties, rather than in a degenerate case.

In order to examine the character of the propagating waves, it is instructive to examine the 3D visualization of the velocity field. Contrary to the acoustic case, a 3-dimensional visualization is necessary to showcase the characteristics of the wave propagation along the principle axes. The velocity in x-direction, u, is examined first (cf. 5.12). The wavefront travelling outwards the fastest clearly moves in x-direction (cf. fig. 5.12a). As given by eq. 5.16 the P-wave moves with a velocity of $3.0\,\frac{\mathrm{m}}{\mathrm{s}}$. The peak of the source is at time $t_{\max} = 4.0\,\mathrm{s}$; at $t = 5.0\,\mathrm{s}$ the wavefront has travelled slightly more than half of the distance between origin and the surface boundary (cf. fig. 5.12a middle). This is in accordance with the $3.0\,\mathrm{m}$ the P-wave is expected to travel in $1\,\mathrm{s}$.

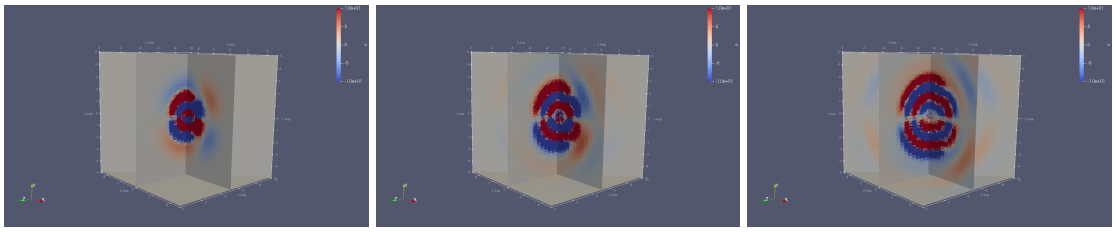

(a) u at $t = 4.5\,\mathrm{s}$, $t = 5.0\,\mathrm{s}$, $t = 5.5\,\mathrm{s}$, in the interval $[-10, 10]$

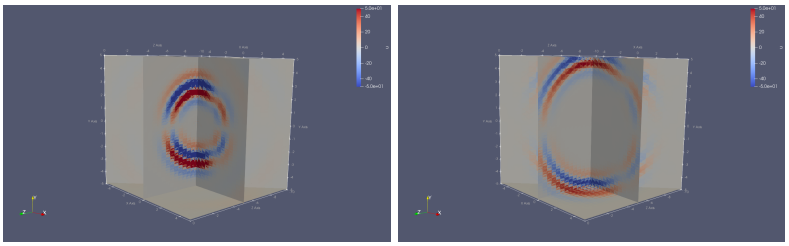

(b) u at $t = 6.0\,\mathrm{s}$, $t = 7.5\,\mathrm{s}$, in the interval $[-50, 50]$

Figure 5.12: The visualization of u: In the upper row both P- and S-wave are observed. The P-wave has a smaller amplitude, therefore, the visualized interval is chosen as $[-10, 10]$. This saturates the display of the S-wave; in the lower row the interval is adjusted to $[-50, 50]$, to better visualize the S-wave

The S-wave can be identified as the second visible wave field. Fig. 5.12a already visualizes a wave travelling in y-direction. Since the amplitude of the S-wave is greater than that of the P-wave, the interval fig. 5.12b is adjusted to visualize the S-wave better. Analogously to before, the propagation velocity is examined. To travel from the origin to the surface boundary along the y-axis a wave with $v_s = 1.41\frac{\mathrm{m}}{\mathrm{s}}$ (see eq. 5.16) requires 3.54 s. At 7.5 s the peak of the second wave is seen to have reached the edge of the volume. Additionally, one observes the y-direction as the direction u is propagating in, thus confirming the presence of a shear wave. That is, both the propagation velocity and the shear wave character of the x-component of the S-wave are confirmed. A similar argument can be made for the velocities v and w. Snapshots of v at identical times can be found in fig. 5.13, where the xz-plane through the origin was added. The primary wave travels in y-direction (cf. fig. 5.13a), whereas the secondary wave travels in x-direction (cf. fig. 5.13b). Again, confirming that the primary wave is a longitudinal wave, while the secondary wave is a shear wave.

Additionally, the strike-slip nature of the source, i.e. the only non-zero entries of the moment tensor are $M_{xy} = M_{yx}$, is confirmed. Both the x and the y component of the shear wave propagate in the xy-plane, and respectively in the yz- and xz-plane.

Figures 5.12 and 5.13 show the symmetries of the wave propagation in an informative manner, which allows us to focus on the error calculations of receivers in one symmetry quadrant. The main part of the error analysis concerns itself with the σ_{xx} and σ_{xy} entries. The choice for σ_{xx} provides a straight-forward connection to the acoustic case, while σ_{xy} is motivated by the design of the moment tensor. The other entries of σ_{ij} are considered when their analysis provides deeper insights.

The time-reversal analysis is begun by examining the time revolution of both σ_{xx} and σ_{xy} for receivers located in one of the symmetry quadrants of the cube (cf. fig. 5.14) [5]. The receivers on the diagonal, e.g. at $(4.0, 4.0, -1.0)$, show both the S- and the P-wave resolved separately in the σ_{xx} component. Considering the diverging wave an exact calculation using the propagation velocities can be made. The receiver is located $\sqrt{4^2 + 4^2 + 4^2} = 6.93\,\mathrm{m}$ away from the surface. As established previously, the peak of the wavefront converges at the origin

[5] The 3D wave field output of σ_{xy} of the entire time-reversal simulation is published as a video: https://youtu.be/G5QZm7ZvAPk.

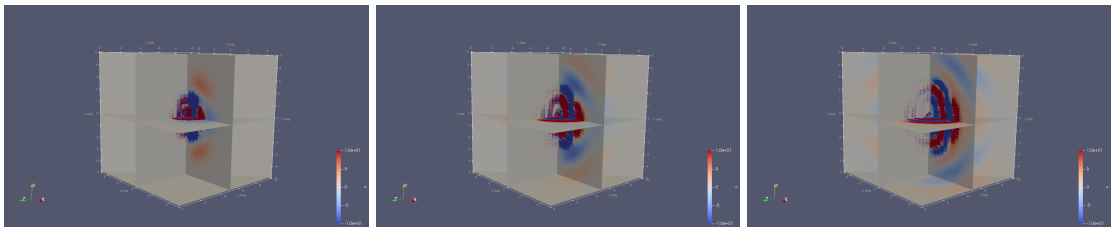

(a) v at $t = 4.5\,\mathrm{s}$, $t = 5.0\,\mathrm{s}$, $t = 5.5\,\mathrm{s}$, in the interval $[-10, 10]$

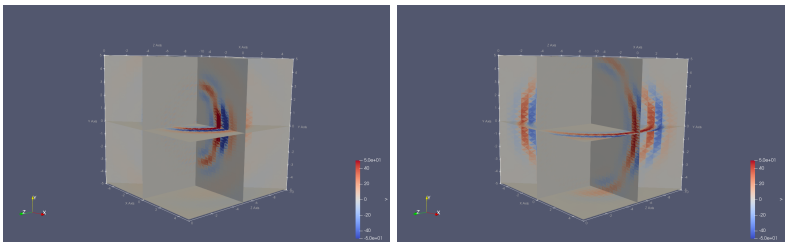

(b) v at $t = 6.0\,\mathrm{s}$, $t = 7.5\,\mathrm{s}$, in the interval $[-50, 50]$

Figure 5.13: The visualization of v: in the upper row in the interval $[-10, 10]$, optimized for showing the P-wave; in the lower row in the interval $[-50, 50]$ for better visualization of the S-wave

at $t = 16.0\,\mathrm{s}$. Using the entries of the recorded receiver file, the sign change between the two peaks of both S- and P-wave can be determined with a precision of $\Delta t = 0.002\,\mathrm{s}$,

$$\begin{aligned} t_p &= 18.319\,\mathrm{s}, \\ t_s &= 20.855\,\mathrm{s}. \end{aligned} \tag{5.19}$$

Adding the time it takes for P- and S-waves to arrive at the receiver location to $t_{\mathrm{conv}} = 16.0\,\mathrm{s}$ yields the expected values

$$\begin{aligned} t_{p,\mathrm{exp}} &= 18.309\,\mathrm{s}, \\ t_{s,\mathrm{exp}} &= 20.810\,\mathrm{s}. \end{aligned} \tag{5.20}$$

Thus indicating that P- and S-wave indeed are resolved separately.

Before the error calculations can be performed, the time evolution of the receiver files has to be modified, such that forward and time-reversed direction are comparable (cf. fig. 5.15). The forward simulation is shown in fig. 5.15a and the corresponding time-reversal in fig. 5.15b. Both the convergent and the divergent wave are clearly visible. Both waves are modified, as detailed in sec. 4.3. The converging wave (*red*) is time-reversed, i.e. essentially played backwards in time, from the moment the wave is converged until the start of the simulation (cf. fig 5.15c). The diverging wave (*blue*) is simply translated in time, such that t_{conv} coincides with t_{max} (cf. fig. 5.15d). This confirms the validity of the theoretical overview given in fig. 4.3.

The quantitative analysis is performed analogously to the acoustic case. The RMS error and both envelope and phase misfits are calculated. The results are presented in tabular form (cf. tab. 5.7). Especially noteworthy is the receiver on the diagonal far away from the source at $(4.0, -4.0, -1.0)$. Both EM and PM for all entries of the stress tensor are below the threshold for an excellent match, as defined by Kristekova *et al.* In fact, most of the envelope misfits are blow 0.1.

To summarize, this section has indicated that the studied medium indeed exhibits both P- and S-waves that can be resolved separately. Furthermore, it was established that the entire wave field is accurately time-reversed.

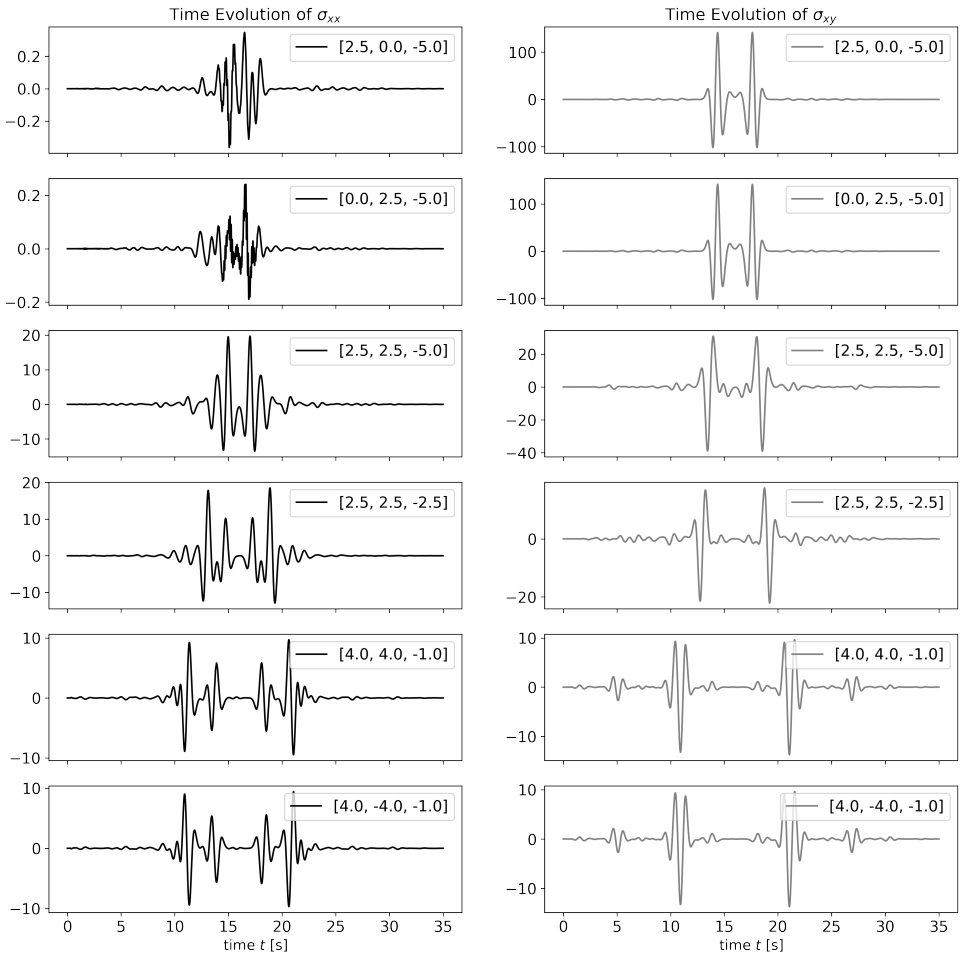

Figure 5.14: Time evolution of σ_{xx} (*left*) and σ_{xy} (*right*) of receivers located in one of the symmetry quadrants of the cube.

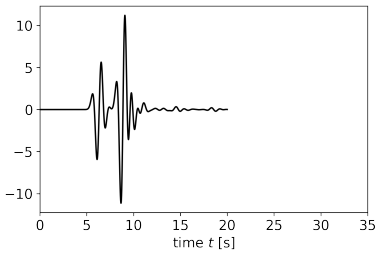

(a) σ_{xx} as recorded by the receiver located at $(4.0, -4.0, -1.0)$ in the forward direction.

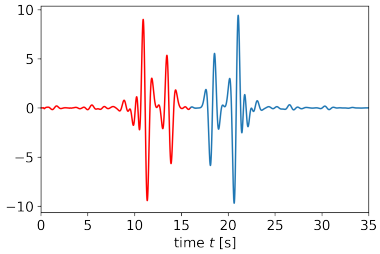

(b) σ_{xx} as recorded by the receiver located at $(4.0, -4.0, -1.0)$ in the time-reversed direction. The red part marks the converging and the blue part the diverging wave.

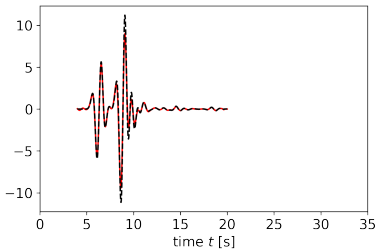

(c) The convergent wave, i.e. the first wavefield in fig. 5.15b, is time-reversed in the interval $[0, t_{\text{conv}}] = [0, 16]$, which corresponds to the interval $[4, 20]$ in the forward direction.

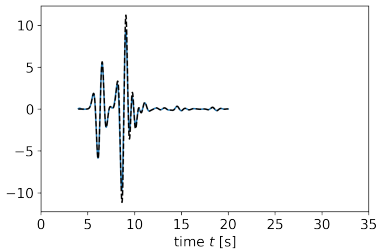

(d) The divergent wave, i.e. the second wavefield in fig. 5.15b, is translated in time, such that it coincides with the original forward propagating wavefield, i.e. $t = 16$ from fig. 5.15b is translated to $t = 4$.

Figure 5.15: The theoretically presented overview (cf. fig. 4.3), is now shown for values obtained through the simulation. The time evolution of σ_{xx} as recorded by the receiver located at $(4.0, -4.0, -1.0)$ is plotted. In the second row, the forward (in black) and time-reversed direction (in grey) are drawn in the same plot.

Table 5.7: Homogeneous medium (elastic): RMS, EM, and PM values obtained from comparing both the convergent and the divergent wave with the forward simulation. Dark grey cells correspond to the best value obtained in each column, while light grey cells mark the worst.

Homogeneous Elastic Medium					
Receiver Position	Wavefront	Q_p	RMS	EM	PM
$(2.5, 0.0, -5.0)$	convergent	σ_{xy}	0.05526	0.02553	0.01208
	divergent		0.05147	0.03068	0.01071
$(0, 2.5, -5.0)$	convergent	σ_{xy}	0.05557	0.02571	0.01212
	divergent		0.05072	0.03170	0.01002
$(2.5, 2.5, -5.0)$	convergent	σ_{xx}	0.08375	0.02173	0.00618
	divergent		0.05584	0.01853	0.00425
	convergent	σ_{xy}	0.06259	0.03851	0.00560
	divergent		0.06451	0.03874	0.01075
$(2.5, 2.5, -2.5)$	convergent	σ_{xx}	0.12810	0.07167	0.00708
	divergent		0.10959	0.05761	0.01056
	convergent	σ_{xy}	0.14405	0.07580	0.00837
	divergent		0.12905	0.06046	0.01649
$(4.0, 4.0, -1.0)$	convergent	σ_{xx}	0.16096	0.07026	0.00694
	divergent		0.13626	0.05243	0.01251
	convergent	σ_{xy}	0.17210	0.09648	0.00738
	divergent		0.14721	0.07713	0.01532
$(4.0, -4.0, -1.0)$	convergent	σ_{xx}	0.16276	0.06891	0.00699
	divergent		0.13910	0.05643	0.01278
	convergent	σ_{yy}	0.15899	0.06526	0.00602
	divergent		0.12241	0.04887	0.00928
	convergent	σ_{zz}	0.17735	0.15095	0.01882
	divergent		0.12931	0.11192	0.01442
	convergent	σ_{xy}	0.17065	0.09650	0.00740
	divergent		0.14539	0.08088	0.01321
	convergent	σ_{yz}	0.16897	0.04334	0.00823
	divergent		0.13828	0.03741	0.00570
	convergent	σ_{xz}	0.15846	0.03916	0.00568
	divergent		0.11337	0.02943	0.00497

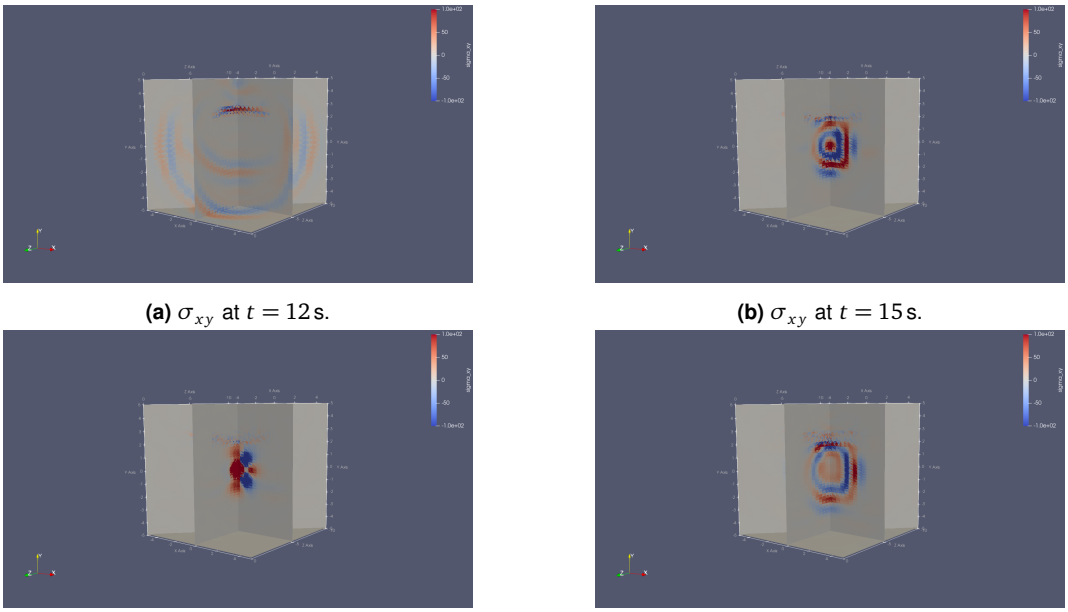

(a) σ_{xy} at $t = 12\,\mathrm{s}$. **(b)** σ_{xy} at $t = 15\,\mathrm{s}$.

(c) σ_{xy} at $t = 16\,\mathrm{s}$. **(d)** σ_{xy} at $t = 17.5\,\mathrm{s}$.

Figure 5.16: Snapshots of σ_{xy} of the time-reversed wavefield at different times in an inhomogeneous medium, in the interval $[-100, 100]$, where blue and red correspond the most negative and positive values, respectively.[6]

5.2.2 Localized Inhomogeneity

Similar to the acoustic case, the time-reversal in a medium with a localized inhomogeneity of high density is studied. For a summary of the error analysis of the contact between two halfspaces in the elastic case, the interested reader is referred to App. B.1.

Identical to the acoustic case, the inhomogeneity is stretches from $[-3, 3]$, $[2, 3]$, $[-8, -2]$ in x-, y-, z-direction, respectively. Its properties are given by

$$\rho_{\mathrm{box}} = 20.0\,,\ \lambda_{\mathrm{box}} = 5.0\,,\ \mu_{\mathrm{box}} = 2.0. \tag{5.21}$$

The 3D visualization of the time-reversal (σ_{xy}) is shown in fig. 5.16[6]. As expected, the wavefront travels towards the origin for $t < 16\,\mathrm{s}$, and diverges for $t > 16\,\mathrm{s}$. At $t = 16\,\mathrm{s}$ the wave is focused around the origin. Since the effects of a reflective boundary on the wave propagation were already discussed in detail in Section 5.1.3, the first two receivers in tab. 5.8 are not considered in more detail here. To aid the analysis of receivers $(4, 4, -1)$ and $(4, -4, -1)$, the time-frequency misfit plots for σ_{xx} of both the converging and diverging wave are shown in fig. 5.17. The amplitude difference between the two receivers is immediately obvious. The inhomogeneity is located between the source and the receiver at $(4, 4, -1)$. As the box is predominantly reflective, only a damped wave reaches the receiver. This explains the large discrepancies in the error calculations of the two receivers. Furthermore, for the receiver at $(4, -4, -1)$ the convergent wave produces consistently smaller errors than the divergent wave. In fact, all misfit calculations comparing the convergent wave with the forward direction are below the ± 0.16 threshold. Fig. 5.17c and fig. 5.17d show the TF misfit plots of both the converging and the diverging wave. The peak of the diverging wave has a visibly lower amplitude than that of the forward direction. This is explained in the same way, as in the acoustic case. As time passes, energy of the wave gets trapped inside the inhomogeneity.

[6] The 3D wave field output of σ_{xy} of the entire time-reversal simulation is published as a video: https://youtu.be/c-5geHHmugo.

Table 5.8: Localized inhomogeneity (elastic): RMS, EM, and PM values obtained from comparing both the convergent and the divergent wave with the forward simulation. Dark grey cells correspond to the best value obtained in each column, while light grey cells mark the highest error.

Localized Inhomogeneity (Elastic Medium)					
Receiver Position	Wavefront	Q_p	RMS	EM	PM
$(0.0, 2.5, -5.0)$	convergent	σ_{xy}	0.59593	0.39150	0.13263
	divergent		0.47215	0.24503	0.10000
$(0.0, 4.0, -5.0)$	convergent	σ_{xy}	0.60846	0.35145	0.10305
	divergent		0.58290	0.32777	0.10829
$(2.5, 1.0, -3.0)$	convergent	σ_{xx}	0.36904	0.07824	0.02485
	divergent		0.29216	0.05211	0.01979
	convergent	σ_{xy}	0.25944	0.13769	0.02000
	divergent		0.19892	0.08604	0.01730
$(2.5, 0.0, -5.0)$	convergent	σ_{xx}	0.39796	0.05066	0.02486
	divergent		0.29728	0.04030	0.01292
	convergent	σ_{xy}	0.11545	0.05359	0.01666
	divergent		0.11700	0.06514	0.02068
$(4.0, 4.0, -1.0)$	convergent	σ_{xx}	0.25780	0.17670	0.04179
	divergent		0.32477	0.18606	0.05845
	convergent	σ_{yy}	0.28918	0.10860	0.04215
	divergent		0.27175	0.11011	0.03683
	convergent	σ_{zz}	0.32599	0.22193	0.06617
	divergent		0.30423	0.19442	0.05933
	convergent	σ_{xy}	0.22043	0.10206	0.02241
	divergent		0.24804	0.11894	0.02867
	convergent	σ_{yz}	0.21428	0.08848	0.02123
	divergent		0.20402	0.07592	0.02659
	convergent	σ_{xz}	0.34058	0.12328	0.02786
	divergent		0.25567	0.08422	0.01978
$(4.0, -4.0, -1.0)$	convergent	σ_{xx}	0.18075	0.08948	0.01525
	divergent		0.28508	0.16384	0.02296
	convergent	σ_{yy}	0.17945	0.07704	0.02071
	divergent		0.29775	0.09461	0.04242
	convergent	σ_{zz}	0.18282	0.12640	0.02610
	divergent		0.27298	0.24562	0.03284
	convergent	σ_{xy}	0.19379	0.11117	0.01240
	divergent		0.29580	0.17132	0.03949
	convergent	σ_{yz}	0.19122	0.05064	0.01127
	divergent		0.26140	0.07728	0.02115
	convergent	σ_{xz}	0.18247	0.03303	0.00632
	divergent		0.39546	0.07837	0.03230

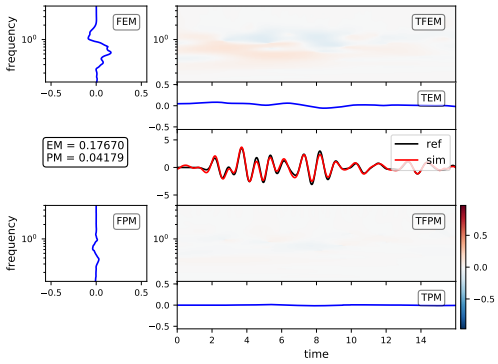

(a) TF misfit of σ_{xx} recorded at position $(4, 4, -1)$. Forward direction compared with the converging wave from the time-reversal.

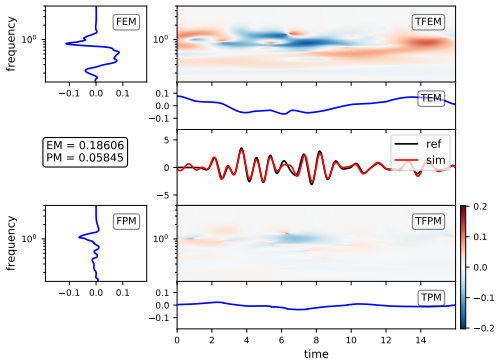

(b) TF misfit of σ_{xx} recorded at position $(4, 4, -1)$. Forward direction compared with the diverging wave from the time-reversal.

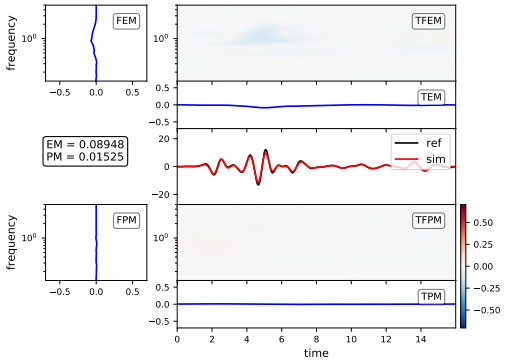

(c) TF misfit of σ_{xx} recorded at position $(4, -4, -1)$. Forward direction compared with the converging wave from the time-reversal.

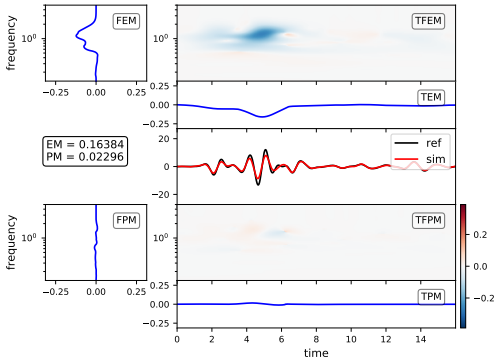

(d) TF misfit of σ_{xx} recorded at position $(4, -4, -1)$. Forward direction compared with the diverging wave from the time-reversal.

Figure 5.17: Time-frequency plots of σ_{xx} recorded at positions $(4, 4, -1)$ and $(4, -4, -1)$, respectively. For each case both the converging and the diverging waves from the time-reversal are compared to the initial simulation.

Thus, comparing the convergent wave with the forward propagation and limiting the statements to receivers that are not blocked by the inhomogeneity, a time-reversal is achieved within acceptable error margins. We have thus shown the validity of the implemented time-reversal method in elastic media, even when inhomogeneities are present in the medium.

5.2.3 Varying Receiver Count

The final analysis conducted using the $(10 \times 10 \times 10)\,\mathrm{m}$ cube returns to the homogeneous elastic medium. The goal of this experiment is to determine how decreasing the number of receivers used in the simulation affects the time-reversed field. When pinpointing the location of the source, the misfit between time-reversed and original wave becomes secondary. Especially, since the error calculations are specific to a point in the volume. The 3D visualization was previously used to gain an overview over the behavior of the time-reversal. It can now be employed to determine, if a limited number of receivers still creates a satisfactory time-reversal. Since the position of the source is of interest, it is instructional to consider sources at different positions. Therefore, the following simulations are both run on the original source at the origin of the cube, and the same source time function translated in x-direction by $x = 2$. In this way, the differences between two possible source locations can be examined.

With knowledge of the source time function and the end time of the forward simulation T_{fwd}, the convergence time can be determined. Since the same source time function as previously is applied, the convergence time is $t_{\mathrm{conv}} = 16\,\mathrm{s}$. Thus, the 3D wave field is examined at time $t = 16\,\mathrm{s}$ (cf. fig. 5.18). Fig. 5.18a serves as the reference case, as it shows the converged wave using 2402 receivers in total, i.e. a receiver spacing of $\Delta x = 0.5\,\mathrm{m}$, which is the same resolution employed throughout the entire analysis above. From fig. 5.18b to fig. 5.18e the receiver count decreases. When spacing the receivers 2.5 m apart, a converged wave can still be observed. Below 98 receivers it is hardly justifiable to speak of a converged wave, as the amplitude almost stretches across the entire principle coordinate directions. Even though the wave field itself is not concentrated at a point, the location of the source can be inferred. To showcase this better, fig. 5.19 shows σ_{xy} on both the xy- and xz-plane. With the knowledge of the moment tensor of the source, in this case $M_{xy} = M_{yx}$ are the only non-zero components, the principle plane can be determined. Using the plots on the left in fig. 5.19, the source location is visible on a 2D plane. To fix the source position in the 3-dimensional volume, the wave field has to be observed in different directions. It is given that in an experimental setup, where the planes through the source location are not known, more effort is required to produce the visualization shown in fig. 5.19. Since this section serves to showcase the capabilities of the time-reversal method using only a limited number of receivers, it is instructional to show the result on the planes intersecting with the source location. Iteratively inspecting different locations of the same plane leads to the same result. Thus, it is possible to determine the location of the source using the time-reversal method with only one receiver at the middle of each face of the cube. How accurately the source position can be determined remains to be studied in future work.

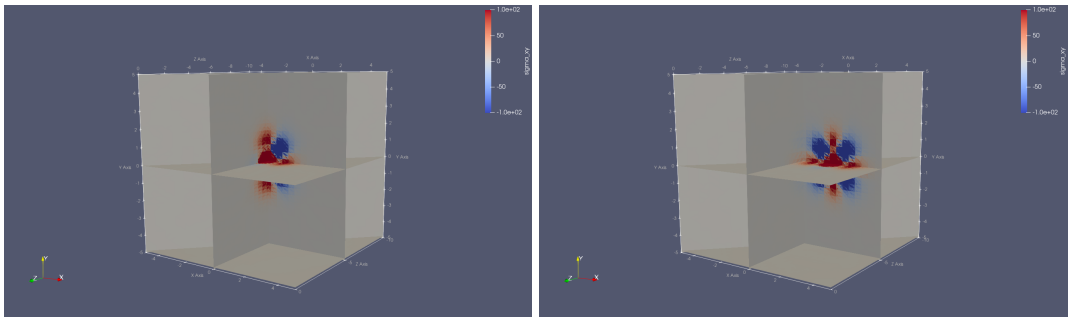

(a) Receivers spaced $\Delta x = 0.5\,\text{m}$ apart (2402 receivers)

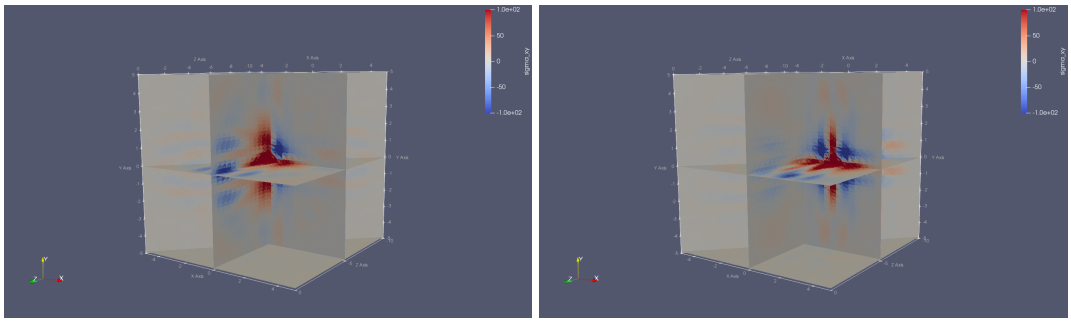

(b) Receivers spaced $\Delta x = 2.0\,\text{m}$ apart (152 receivers)

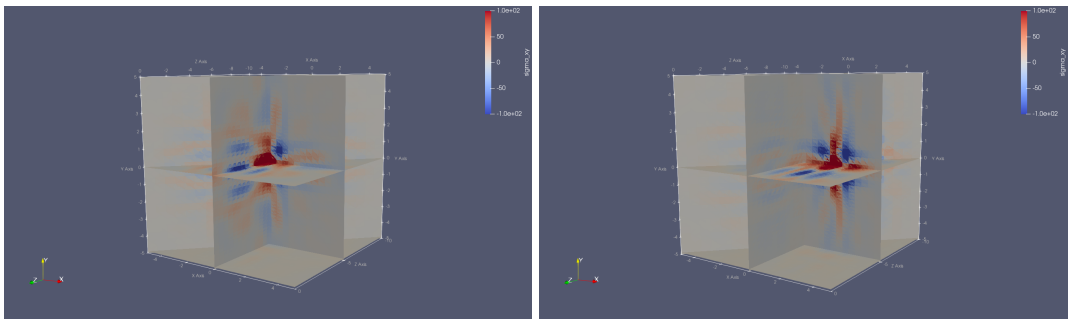

(c) Receivers spaced $\Delta x = 2.5\,\text{m}$ apart (98 receivers)

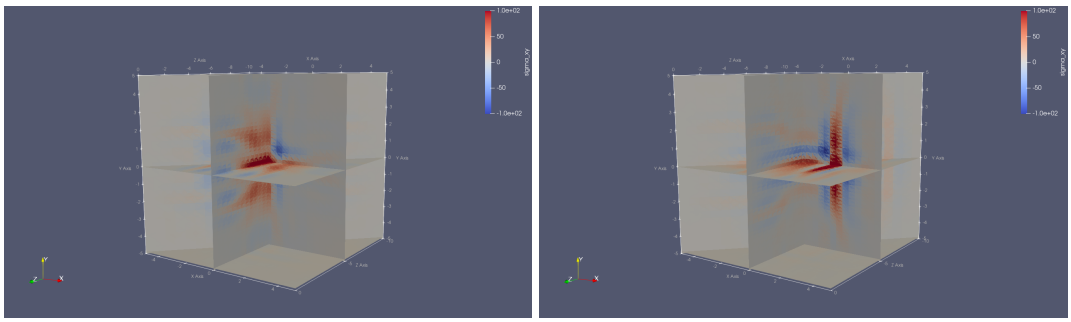

(d) Receivers spaced $\Delta x = 5.0\,\text{m}$ apart (26 receivers)

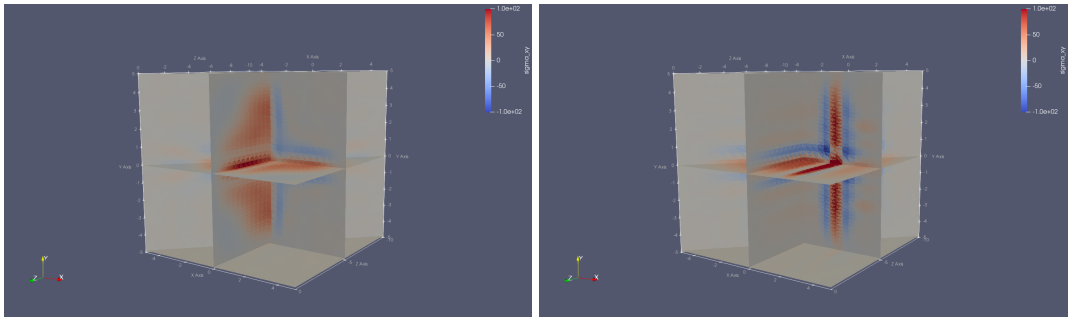

(e) Receivers located in each of the 8 corners and in the middle of each face (14 receivers)

Figure 5.18: The 3D visualization of σ_{xy} at the convergence time ($t = 16\,\text{s}$) with decreasing receiver count. *Left*: Source located at the origin. *Right*: Source located at $(2, 0, -5)$.

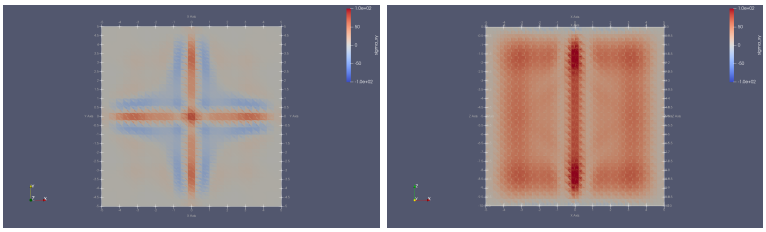

(a) σ_{xy} visualized in the xy-plane (*left*) and the xz-plane (*right*) at $t = 16\,\mathrm{s}$, using data from 6 receivers. The source is located at the origin.

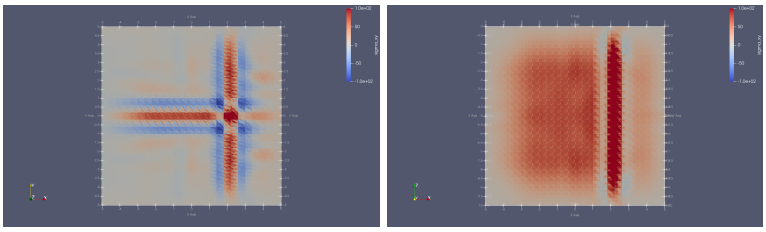

(b) σ_{xy} visualized in the xy-plane (*left*) and the xz-plane (*right*) at $t = 16\,\mathrm{s}$, using data from 6 receivers. The source is located at $(2, 0, -5)$.

Figure 5.19: Both xy- and xz-plane visualized at t_{conv} for sources located at different positions.

5.3 Test Case: WP2-LOH1

The preceding analysis was conducted in a mock environment inside a $(10 \times 10 \times 10)$ m cube. This test case serves to showcase the capabilities of the time-reversal implemented in this thesis outside the simple test environment. For that purpose, the 3D test problem WP2-LOH1 (Wave Propagation 2 - Layer Over Halfspace) is studied, since LOH1 also served as an application example in [DK06]. As the name states, a layer (medium 1) of 1 km thickness is situated above the halfspace (medium 2). The entire volume extends from $[-26000, 32000]$ m in x- and in y-direction, and from $[0, 34000]$ m in z-direction (cf. fig. 5.20). Note, that the z-axis in all figures in this section points upwards, instead of following convention and pointing downwards. This choice is solely motivated by visualization purposes. The material parameters of both media are summarized in tab. 5.9.

	v_p (ms^{-1})	v_s (ms^{-1})	ρ (kg m^{-3})	λ (GPa)	μ (GPa)
Medium 1	4000	2000	2600	20.8	10.4
Medium 2	6000	3464	2700	32.4	32.4

Table 5.9: Material parameters for the LOH1 test case

The source is a point dislocation with only two non-zero entries of the seismic moment tensor $M_{xy} = M_{yx} = M_0 = 10^{18}$ Nm, located at $(x_s, y_s, z_s) = (0, 0, 2000)$ m. The source time function is given by

$$S^T(t) = M_0 \frac{t}{T^2} \exp\left(-\frac{t}{T}\right), \tag{5.22}$$

where T is a smoothness parameter, here chosen as $T = 0.1$. Since the source does not have a dominant frequency, we instead define the maximum frequency $5Hz$, as given in [Her10].

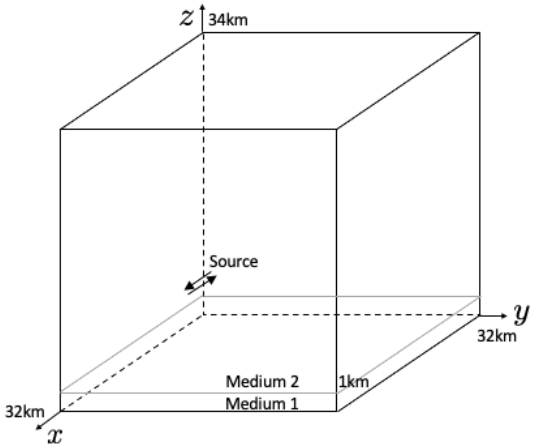

Figure 5.20: Sketch of one quadrant of the LOH1 geometry: A layer of 1 km (medium 1) is above the halfspace (medium 2), and the source is located at $(x_s, y_s, z_s) = (0, 0, 2000)$ m. Note that the z-axis points upwards, in order to keep the same orientation as in fig. 5.21.

The wave field is recorded in the forward direction up to a simulation time of 27 s with a grid of receivers spaced roughly 4.5 km apart on each of the faces of the cuboid, resulting in a total of 552 receivers, which record the outgoing wave field. Subsequently, the time-reversal

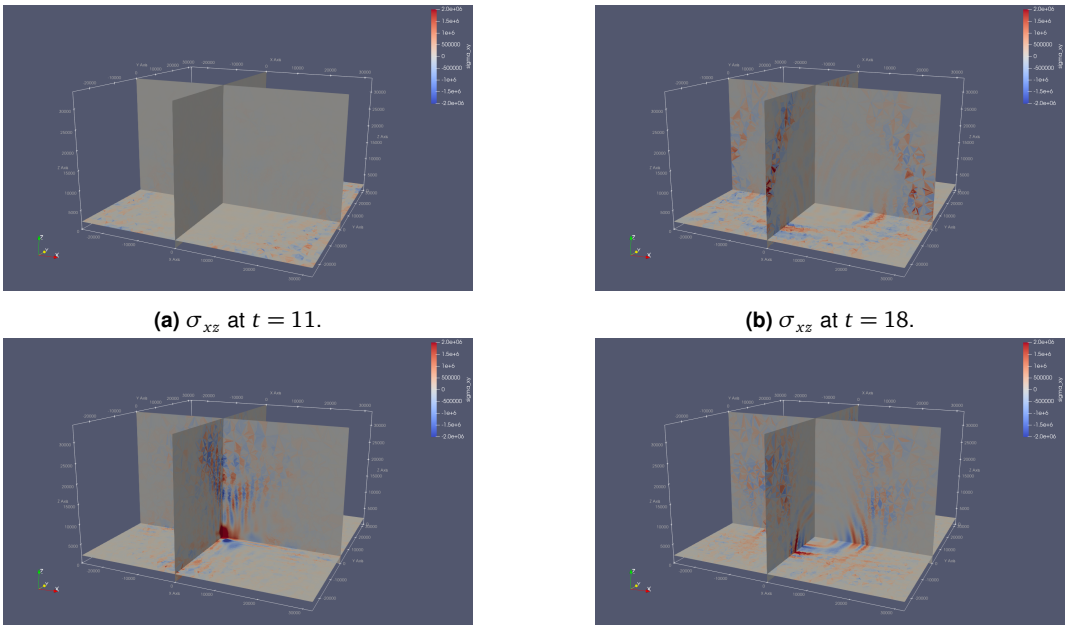

(a) σ_{xz} at $t = 11$.

(b) σ_{xz} at $t = 18$.

(c) σ_{xz} at $t = 27$.

(d) σ_{xz} at $t = 31$.

Figure 5.21: Snapshots of the time-reversed wavefield at different times, we display the quantity σ_{xy} in the interval $[-2.0 \cdot 10^6, 2.0 \cdot 10^6]$, where blue and red correspond the most negative and positive values, respectively. The coordinate system is identical to the one presented in fig. 5.20, with the z-axis pointing upwards. We observe the wavefield first converging to the source position, followed by a diverging wave.

simulation is run and the wave field recorded (cf. fig. 5.21)[7]. Note that the resolution of receivers at the surface is far below the minimum discussed previously. The wavelength of the P-Wave can be obtained using v_p (cf. tab. 5.9)

$$\psi_{p,\min} = \frac{c_{p,1}}{f} = \frac{4000\text{ms}^{-1}}{5\,\text{Hz}} = 800\text{m}. \tag{5.23}$$

Even if receivers would only be spaced $\psi_{p,\min}/4 = 200\,\text{m}$ apart, it would require approximately 300.000 receivers at the surface. Albeit using significantly fewer receivers, the results obtained display the expected behavior. In fact, even though the receiver spacing is larger than the wavelength, $\Delta x \approx 5.6 \cdot \psi_{p,\min}$, the source position inside the volume can still be determined (cf. fig. 5.21c).

The goal of this test case was to present the results from the time-reversal implementation in a more realistic setting. Although our analysis is merely qualitatively, we were able to pinpoint the region of the source through the time-reversed wave field. Developing methods that allow an accurate time-reversal with a limited number of receivers, e.g. on only the surface at $z = 0$, remains a question for future work.

[7]The 3D wave field output of the entire time-reversal simulation is published as a video: https://youtu.be/J1bgmMLQQdY.

Chapter 6

Conclusions & Outlook

In this thesis, we implemented and analysed the time-reversal of seismic waves in SeisSol. The implementation is independent of the medium and the source. Therefore, in addition to performing experiments in a $(10 \times 10 \times 10)$ m volume, the 3D benchmark test scenario, WP2-LOH1 was studied. A quantitative analysis, examining the 3D visualization of the time-reversed wave confirms that the wave field indeed converges to the source position. Thereby delivering proof of a successful time-reversal in realistic scenarios.

The misfit analysis of the time-reversal was initially conducted in an acoustic medium. Visualizing the wavefront provides evidence that the time-reversal behaves as expected. Initially, a backward propagating wave is observed, which converges to the location of the original source. Once converged, the wave immediately diverges and propagates towards the surface of the volume. Using receivers, the wave field was recorded at interesting points inside the volume. The recorded data was then utilized to perform a misfit analysis between the forward simulation and the time-reversal. Analysing the homogeneous acoustic case with receivers spaced $\psi_p/4$ apart, where ψ_p is the wavelength of the P-wave, yields envelope and phase misfits that are all classified as excellent (ranges adopted from Kristekova *et al.* [KKM09]). Subsequently, the contact between two halfspaces was studied. Two distinct materials yield different propagation velocities and, more importantly, different wavelengths. The misfits for waves with a greater wavelength were consistently better than those of smaller wavelengths. After analysing multiple different scenarios, we came to the conclusion that a consistently low envelope and phase misfit can be achieved when spacing receivers $\psi_p/8$ apart. This was also confirmed in homogeneous elastic media, where the calculated misfits mostly were below 0.1.

Furthermore, the behavior of the time-reversal was studied in a medium containing a predominantly reflective inhomogeneity in form of a box. In this case, all receiver locations cannot be regarded as equally important, since the propagation of the wave is obstructed by the inhomogeneity. The overall visualization provides also in this case the indication for a successful time-reversal. Considering only receiver locations, where both the converging and the diverging wave can be resolved separately, the misfit calculations stay smaller than the above mentioned bound of ± 0.16, thus confirming the observation from the visualization. Hence, further establishing the success of the time-reversal of seismic waves in more complicated scenarios.

Finally, the question of how many receivers are actually necessary to produce a visible time-reversed wave was pursued. Decreasingly fewer receivers were placed on the faces of the cube and the 3D visualization of the wave-propagation was observed. Even with a total of 98 receivers, i.e. less than $1/20$ of the receivers used in the misfit analysis, is a converging wave observable. This corresponds to a receiver placed every $\psi_P/1.6$. In the case of a lower receiver count, it would not be adequate to speak of a converging wave. Nonetheless, with the knowledge of the seismic moment tensor of the source and placing only one receiver on

each face of the cube, the location of the original source can still be inferred. Thus promising good prospects for future work, to create more accurate time-reversals using fewer receivers at the surface.

To summarize, in this thesis we have achieved the successful time-reversal of seismic waves in SeisSol, and confirmed the validity of the time-reversal approach of Fink *et al.* ([FP01]) beyond acoustics. Furthermore, a criterion for the receiver spacing yielding consistently small misfits was found, i.e. $\Delta x \leq \psi_P/8$. In addition to the error analysis, reducing the receivers taken into account in the simulation provided the possibility to determine the location of the source with significantly fewer receivers. Finally, the 3D test problem WP2-LOH1 was examined in order to establish the validity of the implemented time-reversal approach beyond the $(10 \times 10 \times 10)$ m test volume.

Future research is needed to prepare the time-reversal method for real world testing, as seismographs on land are commonly placed on the surface of the Earth. Studying the behavior of the time-reversal when receivers are only located on one face is an instrumental step in this direction. Moreover, the misfit analysis studied in a test volume, can be extended to include more realistic scenarios as well.

List of Figures

List of Tables

Appendix A

Error Tables (Acoustic Media)

The appendices contain additional information on the data and on the error calculations in particular. The data presented here is understood to be an extension of Chapter 5.

A.1 Homogeneous

Section 5.1.1 presents the most relevant results of the simulation in the homogeneous acoustic medium. The errors obtained from all 14 receivers are listed in tab. A.1, using a receiver spacing of $\Delta x = 1.0\,\mathrm{m}$ with a $100k$-element mesh. Additionally, a simulation with the same parameters, but with a mesh consisting of $500k$ elements was performed. Its result, tab. A.2 in particular, is referred to in the analysis of the contact between two halfspaces (sec. 5.1.2). Comparing these two tables, we conclude that there is no significant improvement when refining the mesh.

Table A.1: Homogeneous medium (acoustic): RMS, EM, and PM values for 13 receivers placed throughout the volume are calculated. Both the convergent and the divergent wave is comapred with the forward simulation. Dark grey cells correspond to the best value obtained in each column, while light grey cells mark the worst.

Homogeneous Acoustic Medium					
Receiver Position	Wavefront	Q_p	RMS	EM	PM
$(-2.5, 0.0, -5.0)$	convergent	σ_{xx}	0.08331	0.02110	0.01785
	divergent		0.08855	0.04896	0.01998
$(2.5, 0.0, -5.0)$	convergent	σ_{xx}	0.08335	0.02109	0.01788
	divergent		0.08888	0.04909	0.02005
$(0, 2.5, -5.0)$	convergent	σ_{xx}	0.08334	0.02104	0.01788
	divergent		0.08608	0.04624	0.01973
$(2.5, 2.5, -5.0)$	convergent	σ_{xx}	0.12207	0.09395	0.00807
	divergent		0.10377	0.07081	0.01539
$(2.5, 2.5, -2.5)$	convergent	σ_{xx}	0.15008	0.12281	0.01073
	divergent		0.12588	0.09689	0.02372
$(4.0, 4.0, -1.0)$	convergent	σ_{xx}	0.13767	0.11405	0.01117
	divergent		0.10356	0.08580	0.01925
$(4.0, 4.0, -9.0)$	convergent	σ_{xx}	0.13781	0.11433	0.01091
	divergent		0.10451	0.08595	0.01954
$(-4.0, 4.0, -1.0)$	convergent	σ_{xx}	0.13783	0.11433	0.01092
	divergent		0.10452	0.08598	0.01954
$(-4.0, 4.0, -9.0)$	convergent	σ_{xx}	0.13722	0.11368	0.01084
	divergent		0.10160	0.08490	0.01836
$(4.0, -4.0, -1.0)$	convergent	σ_{xx}	0.13766	0.11416	0.01088
	divergent		0.10628	0.08980	0.01869
$(4.0, -4.0, -9.0)$	convergent	σ_{xx}	0.13803	0.11449	0.01093
	divergent		0.10685	0.08877	0.01964
$(-4.0, -4.0, -1.0)$	convergent	σ_{xx}	0.13805	0.11449	0.01094
	divergent		0.10685	0.08879	0.01964
$(-4.0, -4.0, -9.0)$	convergent	σ_{xx}	0.13796	0.11422	0.01120
	divergent		0.10620	0.08887	0.01940

Table A.2: Homogeneous medium (acoustic, 500k-elements mesh): RMS, EM, and PM values obtained by comparing both the convergent and the divergent wave with the forward simulation. Dark grey cells correspond to the best value obtained in each column, while light grey cells mark the worst. An identical setup as in tab. A.1 is used, except for a refined mesh.

Homogeneous Acoustic Medium (500k-elements mesh)					
Receiver Position	Wavefront	Q_p	RMS	EM	PM
$(-2.5, 0.0, -5.0)$	convergent	σ_{xx}	0.08363	0.02170	0.01787
	divergent		0.08424	0.06646	0.01039
$(2.5, 0.0, -5.0)$	convergent	σ_{xx}	0.08328	0.02201	0.01766
	divergent		0.06315	0.03448	0.01056
$(0.0, 2.5, -5.0)$	convergent	σ_{xx}	0.08367	0.02200	0.01766
	divergent		0.06310	0.03487	0.01043
$(2.5, 2.5, -5.0)$	convergent	σ_{xx}	0.12094	0.09176	0.00799
	divergent		0.13919	0.04362	0.03692
$(2.5, 2.5, -2.5)$	convergent	σ_{xx}	0.15198	0.11975	0.01058
	divergent		0.15904	0.06229	0.04467
$(4.0, 4.0, -1.0)$	convergent	σ_{xx}	0.14536	0.11120	0.01080
	divergent		0.14004	0.05695	0.03839
$(4.0, 4.0, -9.0)$	convergent	σ_{xx}	0.13708	0.11385	0.01110
	divergent		0.14977	0.07791	0.04063
$(-4.0, 4.0, -1.0)$	convergent	σ_{xx}	0.13708	0.11385	0.01110
	divergent		0.14978	0.07791	0.04063
$(-4.0, 4.0, -9.0)$	convergent	σ_{xx}	0.13843	0.11501	0.01121
	divergent		0.16003	0.09845	0.04130
$(4.0, -4.0, -1.0)$	convergent	σ_{xx}	0.13697	0.11373	0.01108
	divergent		0.14950	0.07695	0.04055
$(4.0, -4.0, -9.0)$	convergent	σ_{xx}	0.13846	0.11502	0.01121
	divergent		0.15987	0.09760	0.04133
$(-4.0, -4.0, -1.0)$	convergent	σ_{xx}	0.13847	0.11502	0.01121
	divergent		0.15987	0.09760	0.04133
$(-4.0, -4.0, -9.0)$	convergent	σ_{xx}	0.13780	0.11453	0.01114
	divergent		0.16749	0.11612	0.04034

Table A.3: Contact of two Halfspaces (acoustic): RMS, EM, and PM values obtained by comparing both the convergent and the divergent wave with the forward simulation. Dark grey cells correspond to the best value obtained in each column, while light grey cells mark the highest error.

Contact of two Halfspaces (Acoustic Medium)					
Receiver Position	Wavefront	Q_p	RMS	EM	PM
$(0.25, 2.5, -2.5)$	convergent	σ_{xx}	0.13387	0.09620	0.01580
	divergent		0.10186	0.07639	0.01253
$(0.25, 2.5, -5.0)$	convergent	σ_{xx}	0.15020	0.07236	0.00879
	divergent		0.09865	0.03274	0.01297
$(0.25, -2.5, -7.5)$	convergent	σ_{xx}	0.13443	0.09686	0.01577
	divergent		0.10462	0.07874	0.01281
$(-2.5, 0.0, -5.0)$	convergent	σ_{xx}	0.08924	0.03301	0.01544
	divergent		0.12246	0.04274	0.03279
$(2.5, 0.0, -5.0)$	convergent	σ_{xx}	0.09383	0.03662	0.00827
	divergent		0.07620	0.04914	0.01819
$(-2.5, 2.5, -7.5)$	convergent	σ_{xx}	0.16287	0.13699	0.01216
	divergent		0.14695	0.11748	0.02346
$(2.5, 2.5, -7.5)$	convergent	σ_{xx}	0.04501	0.02033	0.00718
	divergent		0.07015	0.05748	0.00507
$(4.0, 4.0, -1.0)$	convergent	σ_{xx}	0.05918	0.04588	0.00600
	divergent		0.05091	0.03803	0.00378
$(-4.0, 4.0, -1.0)$	convergent	σ_{xx}	0.14794	0.12472	0.01448
	divergent		0.12094	0.10085	0.02002
$(4.0, -4.0, -1.0)$	convergent	σ_{xx}	0.05923	0.04588	0.00600
	divergent		0.05324	0.04055	0.00394
$(-4.0, -4.0, -1.0)$	convergent	σ_{xx}	0.14772	0.12459	0.01444
	divergent		0.12227	0.10355	0.01956

A.2 Contact of two Halfspaces

In each halfspace, waves propagate with different wavelengths. In the first simulation, waves with wavelengths $\psi_{p,1} = 2.0\,\mathrm{m}$ in negative x-direction and $\psi_{p,2} = 4.0\,\mathrm{m}$ in positive x-direction are observed. Receivers placed in medium 2 consistently show smaller misfits than those positioned in medium 1 (tab. A.3), obtained with $\Delta x = 0.5\,\mathrm{m}$).

When running the simulation with identical medium parameters, but a receiver spacing of $\Delta x = 1.0\,\mathrm{m}$, spurious oscillations are observed (cf. fig. A.1, which explains the discrepancies seen in the error calculations of the forward and time-reversed wave.

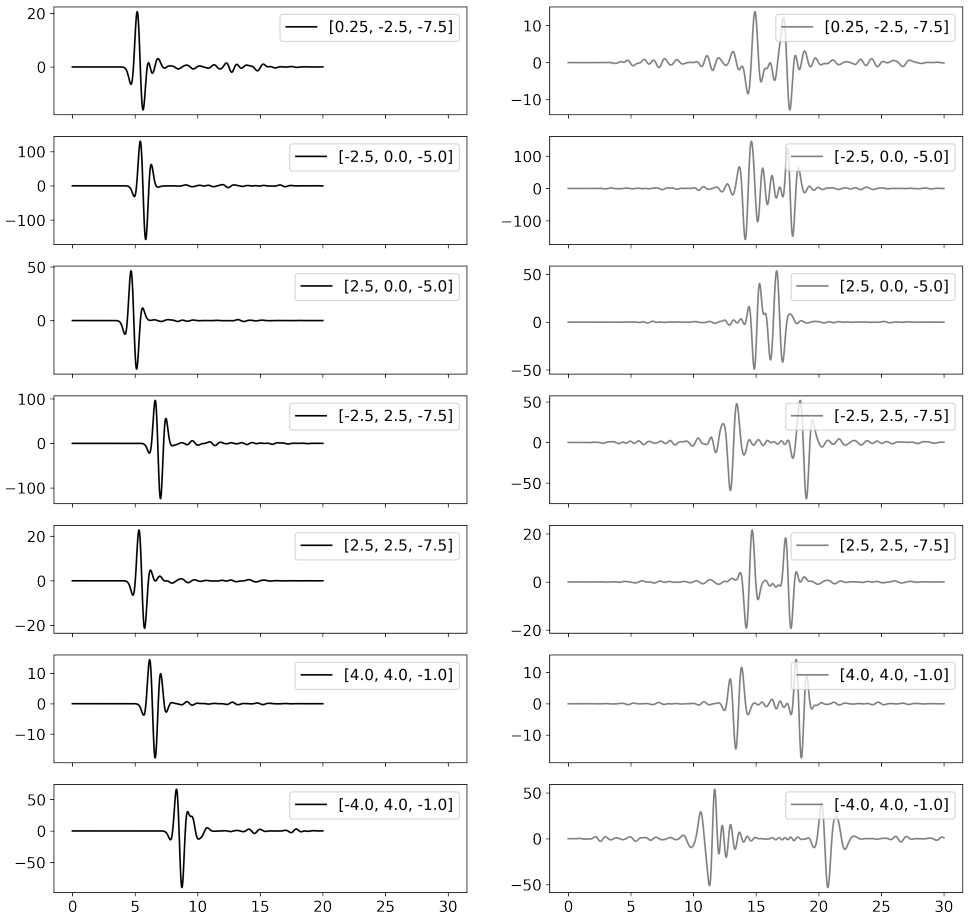

Figure A.1: Contact of two halfspaces (acoustic, $\Delta x = 1.0\,\mathrm{m}$): Time evolution of σ_{xx} in the forward direction (*left*) and in the time-reversal (*right*) at seven distinct locations.

A.3 Localized Inhomogeneity

RMS and TF misfit calculations for 14 receivers are presented in tab. A.4.

Table A.4: Localized inhomogeneity (acoustic): RMS, EM, and PM values obtained by comparing both the convergent and the divergent wave with the forward simulation. Dark grey cells correspond to the best value obtained in each column, while light grey cells mark the highest error.

Localized Inhomogeneity					
Receiver Position	Wavefront	Q_p	RMS	EM	PM
$(0.0, 2.5, -5.0)$	convergent	σ_{xx}	0.80980	0.66990	0.39425
	divergent		0.72297	0.47226	0.14878
$(0.0, 1.0, -5.0)$	convergent	σ_{xx}	0.72855	0.15473	0.11936
	divergent		0.45741	0.26074	0.01702
$(0.0, 4.0, -5.0)$	convergent	σ_{xx}	0.98026	0.52111	0.22047
	divergent		0.50400	0.32086	0.06820
$(-2.5, 4.0, -3.0)$	convergent	σ_{xx}	0.21537	0.12267	0.04252
	divergent		0.11356	0.04274	0.03279
$(-2.5, 1.0, -7.0)$	convergent	σ_{xx}	0.26085	0.11657	0.05392
	divergent		0.21945	0.06428	0.01873
$(-2.5, 0.0, -5.0)$	convergent	σ_{xx}	0.28285	0.09600	0.04889
	divergent		0.28308	0.15233	0.01919
$(2.5, 2.5, -5.0)$	convergent	σ_{xx}	0.92488	0.77945	0.36534
	divergent		0.50485	0.28696	0.11166
$(2.5, 2.5, -2.5)$	convergent	σ_{xx}	1.02943	0.72669	0.40378
	divergent		0.90802	0.65578	0.19013
$(4.0, 4.0, -1.0)$	convergent	σ_{xx}	0.21453	0.11120	0.01080
	divergent		0.16100	0.07822	0.03051
$(4.0, 4.0, -9.0)$	convergent	σ_{xx}	0.15171	0.13029	0.03034
	divergent		0.12011	0.05600	0.02608
$(-4.0, 4.0, -9.0)$	convergent	σ_{xx}	0.19931	0.13801	0.02790
	divergent		0.17658	0.08934	0.03337
$(4.0, -4.0, -1.0)$	convergent	σ_{xx}	0.11097	0.06448	0.01324
	divergent		0.28746	0.20236	0.05989
$(-4.0, -4.0, -1.0)$	convergent	σ_{xx}	0.10331	0.05669	0.01517
	divergent		0.26060	0.22489	0.05139
$(-4.0, -4.0, -9.0)$	convergent	σ_{xx}	0.13239	0.07982	0.01388
	divergent		0.34788	0.22567	0.06436

Appendix B

Error tables (Elastic Media)

B.1 Contact between two Halfspaces

The $(10 \times 10 \times 10)\,\mathrm{m}$ cube is divided into two halfspaces with distinct properties. For $x < 0.25$, the medium is characterized by

$$\rho_1 = 1.0\,,\ \lambda_1 = 5.0\,,\ \mu_1 = 2.0. \tag{B.1}$$

The medium parameters for medium 2, i.e. $x > 0.25$ are given by

$$\rho_2 = 0.5\,,\ \lambda_2 = 5.0\,,\ \mu_2 = 2.0. \tag{B.2}$$

Thus yielding wavelengths

$$\begin{aligned} \psi_{p,1} &= 4.00\,\mathrm{m} \\ \psi_{s,1} &= 1.89\,\mathrm{m}, \end{aligned} \tag{B.3}$$

in medium 1 and

$$\begin{aligned} \psi_{p,2} &= 5.66\,\mathrm{m} \\ \psi_{s,2} &= 2.67\,\mathrm{m}, \end{aligned} \tag{B.4}$$

in medium 2. Since the wavelengths in medium 2 are larger, receivers placed in medium 2 show consistently smaller misfits. The error calculations for the same 11 receivers as in the acoustic case are presented in tab. B.1. Furthermore, tab. B.2 shows the error calculations for all six entries of σ_{ij} for one receiver in each medium.

Table B.1: Contact of two Halfspaces (elastic): Errors calculated for 11 receivers placed throughout the volume. RMS, EM, and PM values obtained by comparing both the convergent and the divergent wave with the forward simulation. Dark grey cells correspond to the best value obtained in each column, while light grey cells mark the highest error.

Contact of two Halfspaces (Elastic Medium)					
Receiver Position	Wavefront	Q_p	RMS	EM	PM
$(0.25, 2.5, -2.5)$	convergent	σ_{xx}	0.12880	0.10048	0.01079
	divergent		0.10679	0.09055	0.00976
	convergent	σ_{xy}	0.13114	0.09053	0.00772
	divergent		0.10260	0.07293	0.00854
$(0.25, 2.5, -5.0)$	convergent	σ_{xx}	0.09261	0.04845	0.01978
	divergent		0.09678	0.07353	0.01551
	convergent	σ_{xy}	0.09421	0.04763	0.01916
	divergent		0.09595	0.06549	0.01584
$(0.25, -2.5, -7.5)$	convergent	σ_{xx}	0.12520	0.09727	0.01066
	divergent		0.10643	0.09053	0.00974
	convergent	σ_{xy}	0.13058	0.09040	0.00770
	divergent		0.10608	0.07658	0.00857
$(-2.5, 0.0, -5.0)$	convergent	σ_{xy}	0.05739	0.02578	0.01053
	divergent		0.04256	0.03388	0.00380
$(2.5, 0.0, -5.0)$	convergent	σ_{xy}	0.06187	0.02658	0.01223
	divergent		0.03965	0.01865	0.00820
$(-2.5, 2.5, -7.5)$	convergent	σ_{xx}	0.14979	0.14280	0.01239
	divergent		0.13223	0.11533	0.02239
	convergent	σ_{xy}	0.15761	0.08519	0.00926
	divergent		0.13910	0.06999	0.01576
$(2.5, 2.5, -7.5)$	convergent	σ_{xx}	0.07408	0.02097	0.00330
	divergent		0.06399	0.01784	0.00462
	convergent	σ_{xy}	0.08033	0.02816	0.00227
	divergent		0.10158	0.03614	0.00713
$(4.0, 4.0, -1.0)$	convergent	σ_{xx}	0.08313	0.02855	0.00594
	divergent		0.07596	0.02474	0.00821
	convergent	σ_{xy}	0.10049	0.03497	0.00272
	divergent		0.11679	0.03813	0.00575
$(-4.0, 4.0, -1.0)$	convergent	σ_{xx}	0.23077	0.15362	0.01466
	divergent		0.19112	0.11490	0.02345
	convergent	σ_{xy}	0.15446	0.10529	0.01021
	divergent		0.13774	0.08360	0.01770
$(4.0, -4.0, -1.0)$	convergent	σ_{xx}	0.09603	0.03374	0.00781
	divergent		0.07360	0.02218	0.00824
	convergent	σ_{xy}	0.08624	0.02450	0.00445
	divergent		0.12006	0.04093	0.00528
$(-4.0, -4.0, -1.0)$	convergent	σ_{xx}	0.24043	0.15461	0.01610
	divergent		0.19261	0.11206	0.02381
	convergent	σ_{xy}	0.15587	0.10428	0.00842
	divergent		0.13518	0.07817	0.01782

Table B.2: Contact of two Halfspaces (elastic): Errors calculated for all six entries of the stress tensor recorded on the space diagonal in medium 1 and 2 respectively. RMS, EM, and PM values obtained by comparing both the convergent and the divergent wave from the time-reversal with the forward simulation. Dark grey cells correspond to the best value obtained in each column, while light grey cells mark the highest error.

Contact of two Halfspaces (Elastic Medium)					
$(4.0, -4.0, -1.0)$	convergent	σ_{xx}	0.09603	0.03374	0.00781
	divergent		0.07360	0.02218	0.00824
	convergent	σ_{yy}	0.06986	0.05844	0.00759
	divergent		0.09727	0.09011	0.01719
	convergent	σ_{zz}	0.07420	0.05838	0.00906
	divergent		0.09507	0.08094	0.01269
	convergent	σ_{xy}	0.08624	0.02450	0.00445
	divergent		0.12006	0.04093	0.00528
	convergent	σ_{yz}	0.09879	0.01517	0.00236
	divergent		0.09795	0.01523	0.00220
	convergent	σ_{xz}	0.10728	0.03494	0.00442
	divergent		0.14500	0.04415	0.00854
$(-4.0, -4.0, -1.0)$	convergent	σ_{xx}	0.24043	0.15461	0.01610
	divergent		0.19261	0.11206	0.02381
	convergent	σ_{yy}	0.19291	0.06654	0.00807
	divergent		0.14507	0.05060	0.00552
	convergent	σ_{zz}	0.18124	0.13536	0.02017
	divergent		0.14545	0.11398	0.01809
	convergent	σ_{xy}	0.15587	0.10428	0.00842
	divergent		0.13518	0.07817	0.01782
	convergent	σ_{yz}	0.19092	0.10581	0.00902
	divergent		0.16011	0.08800	0.01277
	convergent	σ_{xz}	0.14029	0.02504	0.00374
	divergent		0.12861	0.02471	0.00487

Bibliography

[AR02] Aki, K. and Richards, P. G. *Quantitative Seismology*. 2nd ed. University Science Books, 2002. ISBN: 0935702962.

[But87] Butcher, J. C. *The Numerical Analysis of Ordinary Differential Equations: Runge-Kutta and General Linear Methods*. USA: Wiley-Interscience, 1987. ISBN: 0471910465.

[CF92a] Cassereau, D. and Fink, M. "Time-reversal of ultrasonic fields. III. Theory of the closed time-reversal cavity". In: *IEEE Transactions on Ultrasonics, Ferroelectrics, and Frequency Control* 39.5 (1992), pp. 579–592. DOI: 10.1109/58.156176.

[CF92b] Cassereau, D. and Fink, M. "Time-reversal of ultrasonic fields. III. Theory of the closed time-reversal cavity". In: *IEEE Transactions on Ultrasonics, Ferroelectrics, and Frequency Control* 39.5 (1992), pp. 579–592. DOI: 10.1109/58.156176.

[Cla18] Clauser, C. *Grundlagen der angewandten Geophysik - Seismik, Gravimetrie*. Berlin, Heidelberg: Springer Spektrum, 2018. ISBN: 978-3-662-55309-1. DOI: 10.1007/978-3-662-55310-7. URL: https://publications.rwth-aachen.de/record/718008.

[CKS11] Cockburn, B., Karniadakis, G. E., and Shu, C.-W. *Discontinuous Galerkin Methods: Theory, Computation and Applications*. 1st. Springer Publishing Company, Incorporated, 2011. ISBN: 3642640982.

[Dum03] Dumbser, M. "On the Improvement of Efficiency and Storage Requirements of the Discontinuous Galerkin Method for Aeroacoustics". In: *PAMM* 3 (Dec. 2003), pp. 426–427. DOI: 10.1002/pamm.200310484.

[DK06] Dumbser, M. and Käser, M. "An arbitrary high-order discontinuous Galerkin method for elastic waves on unstructured meshes — II. The three-dimensional isotropic case". In: *Geophysical Journal International* 167.1 (Oct. 2006), pp. 319–336. ISSN: 0956-540X. DOI: 10.1111/j.1365-246X.2006.03120.x.

[DM05] Dumbser, M. and Munz, C.-D. "ADER Discontinuous Galerkin Schemes for Aeroacoustics". In: *Comptes Rendus Mécanique* 333 (Sept. 2005), pp. 683–. DOI: 10.1016/j.crme.2005.07.008.

[DM06] Dumbser, M. and Munz, C.-D. "Building Blocks for Arbitrary High Order Discontinuous Galerkin Schemes". In: *J. Sci. Comput.* 27.1-3 (2006), pp. 215–230. DOI: 10.1007/s10915-005-9025-0.

[Fin92] Fink, M. "Time reversal of ultrasonic fields. I. Basic principles". In: *IEEE Transactions on Ultrasonics, Ferroelectrics, and Frequency Control* 39.5 (1992), pp. 555–566. DOI: 10.1109/58.156174.

[Fin97] Fink, M. "Time Reversed Acoustics". In: *Physics Today* 50.3 (1997), pp. 34–40. DOI: https://doi.org/10.1063/1.881692.

[Fin+89] Fink, M., Prada, C., Wu, F., and Cassereau, D. "Self focusing in inhomogeneous media with time reversal acoustic mirrors". In: vol. 2. 1989, pp. 681–686. DOI: 10.1109/ULTSYM.1989.67072.

[FF17] Fink, M. and Fort, E. “From the time-reversal mirror to the instantaneous time mirror”. In: *European Physical Journal: Special Topics* 226 (May 2017), pp. 1477–1486. DOI: 10.1140/epjst/e2016-60258-8.

[FP01] Fink, M. and Prada, C. “Acoustic time-reversal mirrors”. In: *Inverse Problems* 17.1 (Jan. 2001), R1–R38. DOI: 10.1088/0266-5611/17/1/201.

[Her10] Hermann, V. *ADER-DG - Analysis, further Development and Application*. LMU Munich: Institut für Geowissenschaften, PhD Thesis, 2010.

[Käs+10] Käser, M., Castro, C., Hermann, V., and Pelties, C. “SeisSol – A Software for Seismic Wave Propagation Simulations”. In: (2010). Ed. by Wagner, S., Steinmetz, M., Bode, A., and Müller, M. M., pp. 281–292. DOI: 10.1007/978-3-642-13872-0_24.

[KD05] Käser, M. and Dumbser, M. “An arbitrary high-order discontinuous Galerkin method for elastic waves on unstructured meshes - I. The two-dimensional isotropic case with external source terms”. In: *Geophysical Journal International* 166 (Jan. 2005). DOI: 10.1111/j.1365-246X.2006.03051.x.

[Kri+06] Kristekova, M., Kristek, J., Moczo, P., and Day, S. “Misfit Criteria for Quantitative Comparison of Seismograms”. In: *Bulletin of the Seismological Society of America* 96 (Oct. 2006), pp. 1836–1850. DOI: 10.1785/0120060012.

[KKM09] Kristeková, M., Kristek, J., and Moczo, P. “Time-frequency misfit and goodness-of-fit criteria for quantitative comparison of time signals”. In: *Geophysical Journal International* 178.2 (Aug. 2009), pp. 813–825. ISSN: 0956-540X. DOI: 10.1111/j.1365-246X.2009.04177.x.

[Mad76] Madariaga, R. “Dynamics of an Expanding Circular Fault”. In: *Bulletin of the Seismological Society of America* 66 (June 1976), pp. 639–666.

[PCS94] Priolo, E., Carcione, J., and Seriani, G. “Numerical simulation of interface waves by high-order spectral modeling techniques”. In: *THE JOURNAL OF THE ACOUSTICAL SOCIETY OF AMERICA* 95 (Jan. 1994), pp. 681–693. DOI: 10.1121/1.404528.

[RH73] Reed, W. H. and Hill, T. R. “Triangular mesh methods for the neutron transport equation.” In: (1973).

[TMN01] Toro, E., Millington, R., and Nejad, L. “Towards Very High Order Godunov Schemes”. In: *Godunov Methods; Theory and Applications* (Jan. 2001). DOI: 10.1007/978-1-4615-0663-8_87.

[TT02] Toro, E. and Titarev, V. “Solution of the generalized Riemann problem for advection-reaction equations”. In: *Proceedings of the Royal Society A: Mathematical, Physical and Engineering Sciences* 458 (Feb. 2002), pp. 271–. DOI: 10.1098/rspa.2001.0926.

[Wan15] Wang, Y. “Frequencies of the Ricker wavelet”. In: *GEOPHYSICS* 80 (2015), A31–A37. DOI: 10.1190/GEO2014-0441.1.

[WTF92] Wu, F., Thomas, J.-L., and Fink, M. “Time reversal of ultrasonic fields. II. Experimental results”. In: *IEEE Transactions on Ultrasonics, Ferroelectrics, and Frequency Control* 39.5 (1992), pp. 567–578. DOI: 10.1109/58.156175.